

University of Windsor

## Scholarship at UWindor

---

Electronic Theses and Dissertations

Theses, Dissertations, and Major Papers

---

2007

### Effect of pseudoelasticity of nanocrystalline titanium-nickel on wear

Sanjib K. Dey  
*University of Windsor*

Follow this and additional works at: <https://scholar.uwindsor.ca/etd>

---

#### Recommended Citation

Dey, Sanjib K., "Effect of pseudoelasticity of nanocrystalline titanium-nickel on wear" (2007). *Electronic Theses and Dissertations*. 1830.

<https://scholar.uwindsor.ca/etd/1830>

This online database contains the full-text of PhD dissertations and Masters' theses of University of Windsor students from 1954 forward. These documents are made available for personal study and research purposes only, in accordance with the Canadian Copyright Act and the Creative Commons license—CC BY-NC-ND (Attribution, Non-Commercial, No Derivative Works). Under this license, works must always be attributed to the copyright holder (original author), cannot be used for any commercial purposes, and may not be altered. Any other use would require the permission of the copyright holder. Students may inquire about withdrawing their dissertation and/or thesis from this database. For additional inquiries, please contact the repository administrator via email ([scholarship@uwindsor.ca](mailto:scholarship@uwindsor.ca)) or by telephone at 519-253-3000ext. 3208.

**EFFECT OF PSEUDOELASTICITY OF NANOCRYSTALLINE TiNi ON  
WEAR**

**By**

**SANJIB K. DEY**

**A Thesis**

**Submitted to the Faculty of Graduate Studies  
through Engineering Materials  
in Partial Fulfillment of the Requirements for  
the Degree of Master of Applied Science at the  
University of Windsor**

**Windsor, Ontario, Canada**

**2007**

**© 2007 Sanjib K. Dey**



Library and  
Archives Canada

Bibliothèque et  
Archives Canada

Published Heritage  
Branch

Direction du  
Patrimoine de l'édition

395 Wellington Street  
Ottawa ON K1A 0N4  
Canada

395, rue Wellington  
Ottawa ON K1A 0N4  
Canada

*Your file* *Votre référence*  
*ISBN: 978-0-494-34945-8*  
*Our file* *Notre référence*  
*ISBN: 978-0-494-34945-8*

**NOTICE:**

The author has granted a non-exclusive license allowing Library and Archives Canada to reproduce, publish, archive, preserve, conserve, communicate to the public by telecommunication or on the Internet, loan, distribute and sell theses worldwide, for commercial or non-commercial purposes, in microform, paper, electronic and/or any other formats.

The author retains copyright ownership and moral rights in this thesis. Neither the thesis nor substantial extracts from it may be printed or otherwise reproduced without the author's permission.

**AVIS:**

L'auteur a accordé une licence non exclusive permettant à la Bibliothèque et Archives Canada de reproduire, publier, archiver, sauvegarder, conserver, transmettre au public par télécommunication ou par l'Internet, prêter, distribuer et vendre des thèses partout dans le monde, à des fins commerciales ou autres, sur support microforme, papier, électronique et/ou autres formats.

L'auteur conserve la propriété du droit d'auteur et des droits moraux qui protègent cette thèse. Ni la thèse ni des extraits substantiels de celle-ci ne doivent être imprimés ou autrement reproduits sans son autorisation.

---

In compliance with the Canadian Privacy Act some supporting forms may have been removed from this thesis.

Conformément à la loi canadienne sur la protection de la vie privée, quelques formulaires secondaires ont été enlevés de cette thèse.

While these forms may be included in the document page count, their removal does not represent any loss of content from the thesis.

Bien que ces formulaires aient inclus dans la pagination, il n'y aura aucun contenu manquant.

  
**Canada**

## ABSTRACT

The purpose of this research was to investigate the effect of nanocrystalline structure on shape memory (SM) property and pseudoelasticity (PE) of TiNi alloys with a special focus on the application in tribology. A binary TiNi alloy with 50.8at.% Ni was deformed using cold rolling and equal channel angular pressing (ECAP) method at 450 °C to obtain the nanocrystalline structure. The martensitic transformation behaviour after deformation was studied by differential scanning calorimetry and the phase identification was done using X-ray diffraction. SM and pseudoelastic behaviour of the alloy was characterised by indentation and scratch testing. It was shown that after cold rolling and ECAP, the alloy showed higher pseudoelastic recovery. Even though the recovery was not complete, the depth recovery increased with the increasing amount of deformation strain. In addition, the alloy showed 6% SM strain recovery after ECAP processing. The effect of reduced grain size on the PE and SM was analysed and how these properties could be used to achieve a “self-healing surface” was discussed.

## **DEDICATION**

I dedicate this thesis to my dear parents and my dear wife, Sarmistha Das, to whom I owe all my achievements in my life for their unconditional support and effort.

## **ACKNOWLEDGEMENTS**

I would like to thank my advisor Dr. Alpas for accepting me as a graduate student. Thank you very much for your support and supervision throughout my studies at the University of Windsor. I would also like to thank my thesis committee members for their valuable suggestions.

I would like to acknowledge the support and assistance of all the faculty and staff of the University of Windsor. I thank Mr. John Robinson for his assistance during X-ray analysis of the various samples. I would like to thank Mr. Patrick Seguin, Mr. Andy Jenner and all the staff at the Technical Support Centre for their assistance while conducting the pressing experiments. I also thank Ms. Barbara Denomey for her administrative assistance.

I would also like to acknowledge the support extended by GM R&D centre. I sincerely thank Dr. Cheng Y T, Dr. Lukitsch M, and Mr. Bhavesh Shah of GM R&D centre for their discussions and help at various stages of experiments. I thank all my fellow graduate students of GMIRC research group, especially Ahmed Abougharam for driving me down to GM R&D centre to carry out various experiments. Thank you Ahmed once again for your help and friendship. Finally, I thank my wife and my family members who always supported my studies in every possible way.

## TABLE OF CONTENTS

ABSTRACT.....	iii
DEDICATION.....	iv
ACKNOWLEDGEMENTS.....	v
NOMENCLATURE .....	x
LIST OF SYMBOLS .....	xi
LIST OF FIGURES .....	xii
LIST OF TABLES.....	xvi
CHAPTER 1 .....	1
1. Introduction.....	1
1.1. Scope and Objective of the Study.....	3
1.2. Organisation of Thesis.....	4
CHAPTER 2 .....	5
2. Literature Survey .....	5
2.1. Introduction to Pseudoelasticity, Shape memory effect and related phenomenon .....	5
2.1.1. Pseudoelasticity (PE) and Shape Memory Effect (SME) .....	5
2.1.2. Two Way Shape Memory Effect (TWSME) .....	8
2.1.3. Rubber-Like-Behaviour (RLB).....	8
2.2. Martensitic Transformations.....	9
2.2.1. Mechanisms of Martensitic Transformations .....	10
2.2.2. Phase Diagram of TiNi Alloy and Diffusional Transformation .....	11
2.2.3. Factors Affecting the Martensitic Transformations.....	12
2.2.3.1. Effect of Compositional Change.....	12
2.2.3.2. Effect of Cold Working .....	13
2.2.3.3. Effect of Post Deformation Annealing or Ageing .....	16
2.3. Severe Plastic Deformation (SPD).....	17
2.3.1. Equal Channel Angular Pressing (ECAP) .....	19
2.3.2. Processing Routes and Microstructure Development during ECAP .....	20
2.3.3. Strain Calculation during ECAP .....	21

2.3.4. Severe Plastic Deformation on TiNi alloys .....	23
2.3.5. Why Severe Plastic Deformation of TiNi alloys .....	26
2.4. Instrumented Indentation and Shape Memory Effect .....	27
2.4.1. Oliver-Pharr Method.....	28
2.4.2. Quantitative Characterisation of Shape Memory and Pseudoelastic Recovery....	30
2.5. Wear Behaviour of TiNi Alloys.....	31
2.6. Executive Summary of Literature Survey.....	33
CHAPTER 3 .....	51
3. Experimental Methods .....	51
3.1. Composition and As-Received condition of TiNi alloy .....	51
3.1.1. Metallographic Specimen Preparation for Optical Microscopy .....	52
3.2. Preparation of Bulk Nanocrystalline Structure .....	52
3.2.1. Cold Rolling of Ti 50.8at.% Ni.....	52
3.2.2. Equal Channel Angular Pressing (ECAP) of Ti 50.8at.% Ni .....	53
3.3. Differential Scanning Calorimetric (DSC) Measurements .....	55
3.4. X-Ray Diffraction Measurement of Cold Rolled and ECAP Samples.....	55
3.5. Indentation Experiments .....	56
3.5.1. Conical Indentation of Cold Rolled Samples.....	56
3.5.2. Berkovich Indentation of Cold Rolled Samples .....	56
3.5.3. Indentation of ECAP Samples .....	57
3.6. Scratch Experiments .....	59
3.6.1. Scratch Testing of Cold Rolled Samples .....	59
3.6.2. Scratch Testing of ECAP Samples .....	60
3.7. Spherical Indentation of Cold Rolled Samples.....	60
CHAPTER 4 .....	67
4. Results.....	67
4.1. Optical Microscopy of Cold Rolled Samples .....	67
4.2. Differential Scanning Calorimeter.....	67
4.2.1. DSC of Cold Rolled Samples .....	68



4.2.2. Differential Scanning Calorimetry of ECAP Samples.....	68
4.2.3. Summary of DSC Results .....	69
4.3. X-Ray Diffraction Study.....	72
4.3.1. X-Ray Diffraction of Cold Rolled Samples.....	72
4.3.2. X-Ray Diffraction of ECAP Samples .....	72
4.4. Indentation Experiments .....	73
4.4.1. Hardness and Young's Modulus of Cold Rolled Samples.....	73
4.4.2. Spherical PMC Indentation on Cold Rolled Samples.....	74
4.4.3. Hardness and Young's Modulus of ECAP Processed Samples.....	74
4.4.4. Pseudoelasticity of Cold Rolled Samples .....	75
4.4.5. Pseudoelasticity of ECAP Processed Samples .....	75
4.4.6. Shape Memory Behaviour of ECAP Processed Samples .....	76
4.5. Scratch Experiments .....	77
4.5.1. Scratch Testing of Cold Rolled Samples .....	77
4.5.2. Scratch Testing of ECAP samples .....	78
CHAPTER 5 .....	103
5. Discussion.....	103
5.1. Microstructures As Determined By Optical Micrography.....	103
5.2. Experimental Determination of Phase Transformation Temperatures .....	104
5.2.1. Thermodynamics of Martensitic Phase Transformation.....	105
5.2.2. Phase Transformation of Cold Rolled Samples As Determined by DSC.....	106
5.2.3. Phase Transformation of ECAP Processed Samples As Determined by DSC ...	107
5.3. X-Ray Diffraction study of Cold Rolled and ECAP Samples .....	110
5.4. Pseudoelasticity of Cold Rolled Samples .....	113
5.4.1. Mechanical Properties of Cold Rolled Samples .....	117
5.4.2. On the Stress-Strain Diagram of Cold Rolled Samples .....	119
5.5. Shape Memory and Pseudoelasticity of ECAP Samples .....	120
CHAPTER 6 .....	132
6.1. Summary and Conclusions .....	132

6.2. Suggestions for Future Work .....	136
List of References .....	138
VITA AUCTORIS .....	146

## NOMENCLATURE

$A_f$	Austenitic finish temperature
$A_s$	Austenitic start temperature
B19'	Monoclinic structured martensite phase in TiNi alloys
B2	Cubic austenite phase in TiNi alloys
DMA	Dynamic Mechanical Analyzer
DSC	Differential Scanning Calorimeter
EBS	Electron Back Scattered Diffraction
ECAP	Equal Channel Angular Pressing
HPT	High Pressure Torsion
IIT	Instrumented indentation Technique
$M_f$	Martensitic finish temperature
$M_s$	Martensitic start temperature
MST	Micro-Scratch testing
ND	Neutron Diffraction
PE	Pseudoelasticity
PMC	Progressive Multi-Cycle indentation
R	Trigonal structured martensite phase in TiNi alloys
$R_f$	R-phase finish temperature
RLB	Rubber-Like-Behaviour
$R_s$	R-phase start temperature
SIM	Stress Induced Martensite
SME	Shape Memory Effect
SPD	Severe Plastic Deformation
TEM	Transmission Electron microscope
TWSME	Two Way Shape Memory Effect
UFG	Ultra-fine grain
VSI	Vertical Scanning Interferometry
XRD	X-Ray Diffraction

## LIST OF SYMBOLS

$a$	Contact radius
$A_c$	Contact area
$E$	Young's modulus
$E^*$	Reduced composite Young's modulus
$H$	Hardness
$h_c$	Contact depth
$h_f$	Final indentation depth or, Residual indentation depth
$h_m$	Maximum indentation depth
$h_s$	Sink-in depth or displacement of surface at the contact perimeter
$R$	Indenter radius
$S$	Initial unloading stiffness of load-displacement curve
$\epsilon_N$	Equivalent strain after N no of ECAP pass
$\epsilon_r$	Representative strain under indenter
$\nu$	Poisson's ratio
$\Phi$	Die angle of ECAP die
$\Psi$	Corner angle of ECAP die
$\eta_{PE}^h$	Pseudoelastic depth recovery ratio
$\eta_{PE}^w$	Pseudoelastic energy recovery ratio
$\eta_{SME}^h$	Shape memory depth recovery ratio

## LIST OF FIGURES

Figure No	Figure Caption	Page
Figure 2.1.	Appearance of shape memory effect and pseudoelasticity. Demonstration using a schematic diagram showing two dimensional crystal structures of austenite and martensite. (a) Austenite above $A_f$ ; (b) SIM above $A_f$ ; (c) twinned martensite below $M_f$ ; (d) detwinned martensite below $M_f$ . The nomenclature and the structure for various martensites are shown below. ....	35
Figure 2.2.	Two way shape memory of a Ti 51 at.% Ni alloy; (a) 0.3 mm thick sheet; (b) sheet shape during constrain heat treatment; (c) shape of parent phase at 373 K; (d) intermediate shape during cooling to 300 K with R phase; (e) shape of B19' phase at 213 K; (f) intermediate shape with R phase during heating (g) shape of parent phase at 373 K; (h) shape of B19' phase after cooling down to 213 K. Note that shape of both parent and martensite phase is remembered [33]. ....	36
Figure 2.3.	Three transformation paths for TiNi based alloys [32]. ....	37
Figure 2.4.	Schematic diagram of existence of habit plane in austenite and martensite matrix [37]. ....	37
Figure 2.5.	The lattice change from B2 parent phase, (a) to B19' martensite phase, (b) $i, j, k$ refers to parent lattice and $i', j', k'$ refers to the martensite lattice. A shear on $(011)_p$ plane converts the parent structure into B19' martensite structure [37]. ....	38
Figure 2.6.	The phase diagram of TiNi binary alloys by Otsuka et al. The dotted line represents the order-disorder transition for TiNi alloys at $1090^{\circ}\text{C}$ [54]. ....	39
Figure 2.7.	DSC curves for cold rolled $\text{Ti}_{50}\text{Ni}_{50}$ alloy annealed at $500^{\circ}\text{C}$ for 3 h. (a) original specimen with 1.2 mm thickness, (b) the ground specimen to 0.4 mm thickness [64]. ....	40
Figure 2.8.	TEM images of (a) homogenised, (b) 70% rolled; rolled and annealed at (c) 573 K, (d) 673 K, (e) 773 K and (f) 873 K for 1 h. Insets are corresponding SAD [67]. ....	41
Figure 2.9.	$M_s$ temperature as a function of Ni content for binary TiNi alloys. Different data symbol represents data from different authors and the solid line is given by thermodynamic calculations [37]. ....	42
Figure 2.10.	The different possibilities of die design. (a) $\Psi = 0$ , (b) $\Psi = \pi - \Phi$ represents two limiting condition and (c) represents an intermediate situation where the strain can be varied for any given channel angle, $\Phi$ , [84]. ....	43
Figure 2.11.	Different processing routes for any given die design; (a) No rotation of sample, (b) rotation of sample either by $\pm 90^{\circ}$ alternatively or $+ 90^{\circ}$ alternatively, and (c) rotation by $180^{\circ}$ [86]. ....	44

Figure 2.12. Effective strain variation of with corner angle, $\Psi$ for four different channel angle, $\Phi$ .....	45
Figure 2.13. Schematic diagram representing region of shape memory effect and transformation pseudoelasticity in temperature-stress coordinates [99].....	46
Figure 2.14. Stress-strain curves obtained from uniaxial testing showing the effect of grain size on pseudoelasticity of Ti 50.5at.% Ni alloy [100].....	47
Figure 2.15. Schematic cross-section of (a) sharp indentation (b) spherical indentation under load.....	48
Figure 2.16. Typical load displacement curve in instrumented indentation experiments and definition of various parameters measured. ....	49
Figure 2.17. (a) Hardness; (b) H/E* ratio; and (c) wear loss of various specimens. The Y-axis in (c) is in logarithmic scale [114].....	50
Figure 3.1. DSC profile showing the transformation behaviour of as-received Ti 50.8at.% Ni alloy with a heating and cooling rate of 5 °C/min .....	62
Figure 3.2. A schematic of the ECAP die assembly showing various parts. ....	63
Figure 3.3. An actual photograph of the die and heating arrangement for ECAP. The die is at room temperature in the photograph .....	64
Figure 3.4. A typical progressive multi-cycle (PMC) loading-unloading cycle during instrumented indentation.....	65
Figure 3.5. Actual photograph of the heating arrangements during (a) indentation and (b) profilometer measurement.....	66
Figure 4.1. Optical microstructure of (a) as received; (b) solutionised; (c) 10CW; (d) 20CW; (e) 50CW and (f) 80CW sample. Intermediate annealing was done for 50CW and 80CW sample at 600 °C for 15 min. ....	80
Figure 4.2. Differential scanning calorimeter profile of (a) as-received alloy and (b) as-received alloy after solution treatment and quenching (ARS).....	81
Figure 4.3. DSC profiles for various cold rolled samples. Intermediate annealing was done for 50CW and 80CW sample at 600 °C for 15 min. The legend inside each profile corresponds to the sample name. ....	82
Figure 4.4. DSC profile for ARS and ECAP samples. The equivalent strain in solutionised, 1st ECAP, 2nd ECAP, 3rd ECAP and 4th ECAP sample are 0, 0.64, 1.27 1.91 and 2.54, respectively. The legend inside each profile corresponds to the sample name. ....	83
Figure 4.5. Transformation temperatures of Ti 50.8at.% Ni after various passes of ECAP. The X-axis shows the total equivalent strain applied during ECAP. Equivalent strain of 0 indicates ARS sample.....	84

Figure 4.6.	X-Ray diffraction analysis of Ti 50.8at.% Ni ARS sample and after cold rolling to 10, 20, 50 and 80% thickness reduction.....	85
Figure 4.7.	Typical full width half maximum of (110) <sub>B2</sub> peak in ARS and cold rolled samples. (0% reduction indicate ARS sample).....	86
Figure 4.8.	X-ray diffraction analysis of Ti 50.8at.% Ni alloy after various passes of ECAP. Data for ARS sample is also shown. ....	87
Figure 4.9.	Typical full width half maximum of (111) B19' peak in various ECAP samples.....	88
Figure 4.10.	(a) Hardness and (b)Young's modulus of ARS and cold rolled Ti 50.8at.% Ni samples measured during progressive multi-cycle indentation using a Berkovich indenter at 500 mN and 2500 mN indentation loads.....	89
Figure 4.11.	Depth recovery ratio of ARS and cold rolled samples during progressive multi-cycle indentation using a Berkovich indenter. ....	90
Figure 4.12.	Plot showing hardness vs. representative strain for ARS, 10CW and 80CW sample. The data is from two different PMC indentation experiments. ....	91
Figure 4.13.	Hardness and Young's modulus of ARS and ECAP processed Ti 50.8at.% Ni samples measured during nanoindentation using a Berkovich indenter at 100 mN.....	92
Figure 4.14.	Depth recovery ratio of ARS and cold rolled samples during progressive multi-cycle indentation using a conical indenter with 107 μm tip radius.....	93
Figure 4.15.	(a) Depth recovery ratio of ARS measured at room temperature and ECAP samples measured at three different loads at 75 °C; (b) Residual impression of one such set of indents for ARS and ECAP samples taken from WYKO optical profilometer.....	94
Figure 4.16.	WYKO 2D images of indent recovery of Ti 50.8at.% Ni samples after ECAP showing SME at various loads; BH: before heating, AH: after heating.....	95
Figure 4.17.	Cross section of the indents made on (a) 1st ECAP, (b) 2nd ECAP, (c) 3rd ECAP and (d) 4th ECAP sample before heating (BH) and after heating (AH) at 20N load.....	96
Figure 4.18.	(a) WYKO optical surface profile image of a typical scratch showing the position from where the depth is measures (only 0.825 mm of the scratch distance is shown); (b) Maximum scratch depth (during loading, measured by scratch tester) and the residual scratch depth (after unloading, measured by WYKO) profile along the length of the scratch showing the pseudoelastic recovery of ARS and cold rolled Ti 50.8at.% Ni sample. ....	97
Figure 4.19.	WYKO 3D optical surface profilometer images of the scratches made on ARS and cold rolled Ti 50.8at.% Ni samples showing PE effect. Only half of the scratch length (~1 mm) is shown.....	98
Figure 4.20.	(a) Optical surface profile image showing how the depth along the cross section profile was taken; (b) The cross section profile of the recovered	

	scratches at the maximum depth corresponding to 10N load, measured from WYKO images. The depth indicates recovered depth after unloading. ....	99
Figure 4.21.	Average scratch depth (during loading) and average recovered scratch depth (after unloading) at maximum scratch load of 10 N for ARS and cold rolled Ti 50.8at.% Ni sample. The error bar indicates six individual measurements on each sample.....	100
Figure 4.22.	Average scratch depth and residual scratch depth measured at a point corresponding to the maximum load (10N) applied during the scratch for ARS, 1st ECAP, 2nd ECAP, 3rd ECAP and 4th ECAP sample. The scratch tester measures the scratch depth and the optical profilometer measures the residual depth. (Zero equivalent strain during ECAP represents ARS sample).....	101
Figure 4.23.	3D optical surface profiles of the residual scratch depths on ARS, 1st ECAP, 2nd ECAP, 3rd ECAP and 4th ECAP sample. ....	102
Figure 5.1.	Schematic free energy diagram showing the effect of increasing non-chemical free energy contribution to transformation temperatures. $G_c^P$ , is the chemical free energy for parent phase; $G_c^M$ , is the chemical free energy in martensite phase. In all other terms subscript 'nc' represents nonchemical free energy of corresponding phase; $\Delta G_{nc}^{P \rightarrow M}$ , is the change in nonchemical free energy associated with parent to martensite transformation.....	126
Figure 5.2.	Schematic of the mechanism for deformation twin formation in B2 austenite during cold rolling of Ti 50.8at.% Ni above $A_f$ temperature via the $B2 \rightarrow B19' \rightarrow B2$ transformation sequence.....	127
Figure 5.3.	The depth recovery ration and the representative strain for ARS and 80CW sample during a simple indentation using a conical indenter having 107 $\mu\text{m}$ tip radius at three different indentation loads. The numbers in the boxes are the representative strain applied during the indentation. ....	128
Figure 5.4.	Calculated depth recovery ratio for ARS, 10CW and 80CW sample from the result shown in Figure 4.12. Only the first set of indentations were used for the calculation. ....	129
Figure 5.5.	Pseudoelastic depth recovery ratio and representative strain of ARS sample measured at room temperature and ECAP samples measured at three different loads at 75 $^{\circ}\text{C}$ using a spherical indenter with 200 $\mu\text{m}$ tip radius; (a) at Indentation load 5N (b) at 10 N and (c) at 20 N. ....	131



## LIST OF TABLES

<b>Table No</b>	<b>Table Caption</b>	<b>Page</b>
Table 2.1.	Mechanical properties of TiNi alloys compared to stainless steel [14].....	6
Table 2.2.	Effect of ECAP pass and subsequent annealing on the room temperature mechanical properties of Ti 50.2at.% Ni alloy [96 ].....	25
Table 4.1.	Transformation temperatures of as-received TiNi alloy and after solutionisation followed by quenching (ARS).....	68
Table 4.2.	Martensitic transformation behaviour of ARS and Cold rolled samples.....	71
Table 4.3.	Martensitic transformation behaviour of ECAP processed samples.....	71
Table 5.1.	Estimated contact radius and representative strain under the conical indenter with 107 $\mu\text{m}$ tip radius for ARS and various cold rolled samples during PMC up to 2500 mN. Data shown is only for the 5th indentation cycle with peak load of 2500 mN.....	114
Table 5.2.	Calculated contact radius, equivalent strain and measured PE recovery and SME recovery of Ti 50.8at.% Ni alloy after different ECAP passes.....	122

# CHAPTER 1

## 1. Introduction

In twentieth century, one of the greatest milestones in materials science is discovery of shape memory effect in 1932 by Ölander in his study of rubber like effect in Au-Cd alloy system [1,2]. However, material scientists did not pay much attention to this phenomenon until serendipitous discovery of NiTi alloys by Buhler and colleagues at the US Naval Ordnance Laboratory [3,4] in 1959. Later the alloy was patented under the trade name of Nitinol (abbreviation of Ni-Ti Naval Ordnance Laboratory) and is being widely used since its discovery. Researchers have developed many other alloy systems and polymeric materials later, which show the shape memory effect (SME) but TiNi alloys remained the most important practical shape memory alloy due to their unique properties, which will be discussed in the later sections. These “smart materials” as their name suggests are able to memorise their predetermined shape and after being bent, stressed or otherwise mechanically deformed they are able to return to the original shape upon heating. To observe SME, the materials have to be deformed at a lower temperature state and then heated to a higher temperature, thereby remembering the shape of high temperature state. The alloys systems that exhibit shape memory effect other than TiNi binary and ternary (TiNiX; X = few wt% of Fe, Cu, and many others) alloys include AgCd, AuCd, CuZn, CuSn, CuAlNi, InTi, FeMnSi, CuZnX (X = few wt% of Si, Sn, Al). There are various other polymer based shape memory materials and the list of examples of such shape memory Polymers (SMP) is endless [5] and are not discussed here.

In addition to traditional heat-induced effects, shape-memory alloys can also exhibit stress-induced shape memory behaviour - resulting in a property known as 'superelasticity' or 'pseudoelasticity' or 'transformation pseudoelasticity' [6]; through out this thesis the term pseudoelasticity will be used. When a shape-memory material in its high temperature state with the austenite phase is bent, the resulting stresses can cause it to transform to a softer and more malleable low temperature phase, which is martensite. This allows the alloy to accommodate quite severe deformations in its shape without the detrimental initiation of microstructural defects. When the stress is released, transformation back to the austenitic phase allows it once again to recover its original shape. Unsurprisingly, the pseudoelasticity of shape-memory alloys has many practical uses, some of the more successful of which have included the manufacture of super-resilient, 'life-proof' mobile phone antennas and eye glass frames [10].

So far, it is discussed that shape memory effect is achieved either by heating and cooling the material or by the application and removal of stress from the material. There is another way by which the shape memory effect can be achieved; by applying and removing a magnetic field (magnetic shape memory material) [7]. Two classic examples of magnetic shape memory alloy are Fe<sub>31.9</sub>-Ni<sub>9.8</sub>-Co<sub>4.1</sub>-Ti and Ni-Mn-Ga [8, 9].

Since its inception, shape memory alloys are used extensively in many industries. Many literature reviews [10-12] are available which deal with applications of shape memory alloys. The interested readers are suggested to go through these references and the references cited therein. However, for completeness, the applications that use pseudoelasticity of TiNi alloys will be discussed here in brief. The first and important application was orthodontic arch wires for the correction of teeth [13]. Eyeglass frames are also available in the

consumers market, which absorb large amount of deformation. For comfort and improved fit pseudoelastic TiNi wires are used in the heel of a shoe [10]. Using the same property, headphones are developed which can be folded in to a compact egg shape for carrying easily. Portable phone antennas are also made from pseudoelastic TiNi that resists permanent kinking [14]. Interestingly all these applications use TiNi wire. Bulk or structural use of TiNi alloys utilising their shape memory ability and pseudoelasticity are very limited.

### **1.1. Scope and Objective of the Study**

Unlike biological surfaces, which have self-healing capabilities, conventional metallic surfaces do not exhibit the self-healing property. However, in most industrial applications surface damage is introduced while they come into the contact of other similar or dissimilar surfaces. Therefore, achieving self-healing property in bulk metallic surfaces and coatings is opening a new direction in the field of Tribology. Researchers have explored the shape memory property to improve the contact surface damage during cavitation-erosion [15,16] and dry sliding wear [17,18]. Self-healing effect in bulk TiNi shape memory alloy has been studied by Ni et al. [19] using microindentation. It is reported in the literature that nanocrystalline materials show improved mechanical properties and shape memory materials are no exception to this – shape memory effect and pseudoelasticity are seen in microscopic scale [20]. Investigators have also used shape memory alloys as self-healing surfaces based on their shape memory effect and as super-elastic interlayer between hard coating and soft surfaces to reduce the coefficient of friction and wear loss [21,22]. However, no study has been conducted where pseudoelastic property is used to achieve self-healing surface. This is important from practical applications point of view, since it is not possible to heat and cool every contact systems or surfaces and take the benefit of shape memory based self-healing.

Thereby, the present study focuses into achieving a bulk-nanocrystalline TiNi pseudoelastic alloy (Ti 50.8at.% Ni) using conventional cold rolling method and severe plastic deformation (SPD) technique, namely equal channel angular pressing (ECAP). The martensitic transformation behaviour will be studied using DSC and XRD analysis. After that pseudoelastic and shape memory property of this particular alloy is measured and the possibility of achieving a self-healing surface utilising the pseudoelastic property of this alloy is explored.

## **1.2. Organisation of Thesis**

The thesis has five different chapters. Chapter 1 is the introduction to this thesis. Chapter 2 deals with literature survey related to this thesis. Chapter 3 explains the experimental methods and characterisation techniques. The experimental results are introduced in Chapter 4 and in the last chapter, results are discussed exhaustively. The literature survey in Chapter 2 is divided into five sections. The first section is the introduction to shape memory alloys and the related phenomenon. In the second part, introduction to martensitic transformation, its mechanism in binary TiNi alloys and various factors which affect the martensitic transformations are reviewed. In the third part, severe plastic deformation techniques are reviewed with emphasis on equal channel angular pressing (ECAP). Different processing routes of ECAP and microstructural development during ECAP and previous work related to ECAP of binary TiNi alloys are given. The next part deals with instrumented indentation techniques. A brief introduction to Oliver-Pharr method [23,24] is given and how the researchers have used the indentation technique to characterise the shape memory and pseudoelastic recovery of TiNi alloys are explained. The last part reviews the previous studies on macroscopic and microscopic wear behaviour of TiNi alloys.

## **CHAPTER 2**

### **2. Literature Survey**

#### **2.1. Introduction to Pseudoelasticity, Shape memory effect and related phenomenon**

Since its serendipitous discovery by Buhler at Naval Ordnance Laboratory [4], the TiNi shape memory materials have become quite popular among all other shape memory materials. The reasons being TiNi based alloys exhibit varied degree (up to 8% of recoverable strain) of shape memory effect. In addition, they show pseudoelasticity. Overall, they possess excellent mechanical properties [25-26], good corrosion and abrasion resistance [28-30]. They also show high amount of ductility when plastically deformed. Typical mechanical properties of TiNi alloys compared to stainless steel are given in Table 2.1 [14]. The binary TiNi alloys show both diffusional and diffusionless transformation. The diffusionless transformations are responsible for the martensitic transformation, whereas, the diffusional transformation cause precipitates to form, which again affects the martensitic transformation. These transformation mechanisms will be discussed in later part of this Chapter. In the next section, the definition of pseudoelasticity and shape memory effect and related phenomena will be introduced.

##### **2.1.1. Pseudoelasticity (PE) and Shape Memory Effect (SME)**

The mechanism of pseudoelasticity and shape memory effect are same in all shape memory alloys. However, they will be discussed here taking the reference of TiNi binary alloys. The TiNi binary alloys have two different phases depending on the temperature. The high temperature phase is the austenite and the low temperature phase is the martensite. The temperature at which these two different phases appear depends on the composition, thermal

and mechanical history of the alloy. It is worth mentioning here that the high temperature phase (also termed as the parent phase), austenite, is cubic and similar to B2 structure of CsCl [31]. The low temperature phase, martensite, has a complex monoclinic (B19' martensite), orthorhombic (B19 martensite) or trigonal (R phase) structure depending on the alloys system and transformation path [32] and will be discussed in more details in later sections. TiNi alloys undergo solid-state phase transformations between these two phases upon heating and/or by deformation.

**Table 2. 1. Mechanical properties of TiNi alloys compared to stainless steel [14]**

	TiNi	Stainless steel
Max reversible elastic deformation	8%	0.8%
Mass density, kg.m <sup>-3</sup>	6450	8750
Young's modulus(E), GPa	M: 28-41 A: 83	190-210
Shear modulus (G), GPa	M: 10-15.5 A: 31	75-80
Poisson's ratio (ν)	0.33	0.27-0.30
Yield stress, MPa	M: 70-140 A: 195-690	400-1600
Ultimate stress, MPa	895-1900	700-1900
Coefficient of Thermal Expansion (CTE), / °C	M: 6.6×10 <sup>-6</sup> A: 11×10 <sup>-6</sup>	8-10 ×10 <sup>-6</sup>

When the forward transformation from austenite to martensite takes place by application of stress and upon removing the stress the reverse transformation from martensite to austenite takes place at a single temperature slightly above a critical temperature, the

phenomenon is called pseudoelasticity. The strain recovery is pseudoelastic because the strain is recovered but it occurs via a hysteresis loop. When the same forward and reverse transformation is seen by heating and cooling the alloy and the deformation induced at a lower temperature is recovered upon heating the alloy at a higher temperature, the phenomenon is termed as shape memory effect. However, in both cases the original shape is regained and it is only the deformation temperature, which determines the difference between them. In case of PE, the deformation is done at higher temperature in the parent phase and in case of SME, the deformation is done at lower temperature in the martensite phase. Another interesting consideration is that both PE and SME is seen in the same alloy. The occurrence of both is best explained with the help of a schematic diagram as shown in **Figure 2.1**. The transformations are characterised by four different temperatures namely,  $M_S$ ,  $M_f$ ,  $A_S$ ,  $A_f$ .  $M_S$  and  $M_f$  represent the start and finish temperatures of martensite formation during cooling and  $A_S$  and  $A_f$  represent the start and finish temperature of austenite formation during heating. When there is an intermediate transformation to R phase, using similar terminology the transformation is characterised by  $R_S$  and  $R_f$ . Above  $A_f$  temperature when austenite (a) is deformed, stress induced martensite (SIM) is formed (b) and upon unloading SIM transforms back to austenite (a). The shape recovery associated with this  $\left( (a) \xleftarrow[\text{unloading}]{\text{loading}} (b) \right)$  is called pseudoelasticity. On the other hand when (a) is taken below  $M_f$  temperature twinned martensite is formed (c). Upon loading twinned martensite becomes detwinned (d) and unlike in pseudoelasticity detwinned martensite does not transform back to twinned martensite upon unloading. However, after heating this detwinned martensite goes back to austenite (a) showing shape recovery. The cycle  $\left( (a) \xleftarrow[\text{cooling}]{\text{heating}} (c) \xrightarrow{\text{stress}} (d) \xrightarrow{\text{heating}} (a) \right)$  is called shape memory effect (SME).



### 2.1.2. Two Way Shape Memory Effect (TWSME)

The shape memory effect means one-way shape memory effect in general, unless otherwise mentioned, which means only the shape of parent phase or high temperature phase is remembered. The same alloys after particular processing can remember both hot shape and cold shape related to the shape of high and low temperature phase, respectively. This effect is called two way shape memory effect (TWSME) or reversible shape memory effect and is shown in **Figure 2.2** [33], where a 0.3 mm thick Ti 51at.% Ni alloy sheet (a) is heat treated under constraint (b). After the treatment, the alloy is cooled to 373 K to take the shape (c) in austenite phase. Further cooling to 300 K the parent phase transforms to an intermediate R phase taking the shape (d). Further cooling below  $M_f$  the alloy takes the shape (e). After that when the alloy is heated above  $A_f$  (g), it regains the original shape through an intermediate R phase transformation (f). During further thermal cycling, the alloy remembers both high and low temperature shape. There are various training methods such as introduction of plastic deformation [34], thermal cycling [35], using which TWSME can be introduced. Recently, Zhang et al. [36] have shown that TWSME also exists under complex loading conditions produced by indentations. A good review on TWSME is available in [10,37]. Interested readers may go through those papers.

### 2.1.3. Rubber-Like-Behaviour (RLB)

A number of ordered alloys show an unusual deformation behaviour, which was first found by Ölander in 1932 in Au-Cd alloy [1,2]. This alloy in martensitic phase after being aged for some time, can exhibit rubber like recovery or pseudoelastic recovery upon deformation. The Stress-Strain curve of this alloy in martensitic stage after ageing is very similar to pseudoelastic Stress-Strain curve, but the phenomenon is completely different from

pseudoelasticity as the deformation and the recovery takes place in martensitic stage. Later, the list of alloy system which show this kind of behaviour has grown and it is reported [38-40] that Au-Cu-Zn, Cu-Zn-Al, Cu-Al-Ni, In-Tl show rubber like behaviour (RLB). The origin of this behaviour [41] is quite complex and it is believed that RLB occurs because of the reversible movement of twin boundaries. However, what makes the twin boundary reversible is not understood very clearly.

## 2.2. Martensitic Transformations

In the **Figure 2.3** [32], different types of martensitic transformation paths are depicted. There are three types of transformations. All alloys have a tendency to transform from B2 (austenite) to B19' martensite in Ti-Ni-based alloys. Particularly for the solution-treated binary Ti-Ni alloys, where the alloys are taken above 900 °C and then quenched to room temperature to retain the austenite phase at room temperature, the transformation occurs from B2 to B19' directly, while for the upper and lower cases two successive transformations occur upon continuous cooling.  $B2 \leftrightarrow R \leftrightarrow B19'$  transformation is normally seen in Ti-Ni-Fe ternary systems [42]. They can also be seen in TiNi binary alloys, if they are cold worked followed by annealing at proper temperatures, so that high density of re arranged dislocations are left in the specimen.  $B2 \leftrightarrow B19 \leftrightarrow B19'$  transformation is seen in Ti-Ni-Cu ternary systems [43] and the transformations have composition dependence. When  $7.5 \leq x \text{ (at.\%Cu)} \leq 16$ ,  $B2 \leftrightarrow B19 \leftrightarrow B19'$  transformations occur and when  $5 \leq x \text{ (at.\%Cu)} \leq 7.5$ , the two stage transformation actually occurs but the second transformation occurs quickly after the first one and it is difficult to observe the first transformation. However, depending upon the composition and heat-treatment, only the first transformation may occur

and the second one may be lost, because the possible transformation temperatures for the second one to B19' become too low (i.e. below 0 K) in that case.

B19' martensite is obtained when binary Ti-Ni alloys are quenched from high temperature after solution treatment. The crystal structure of B19' phase is monoclinic and so far in the literature various crystallographic data related to this structure is reported [44-47]. The crystal structure of B19 martensite is orthorhombic [48]. The structure of the R phase martensite is rhombohedral and the lattice can be described by stretching the cubic parent lattice along  $\langle 111 \rangle$  diagonal direction [49,50].

### **2.2.1. Mechanisms of Martensitic Transformations**

To understand and work with TiNi alloys it is imperative to understand the martensite transformation mechanism. In this section, some terminologies related to a specific type of martensitic transformation ( $B2 \leftrightarrow B19'$ ) in TiNi binary alloys systems will be introduced. The martensitic transformation in general can be explained by well-established theory called “phenomenological crystallographic theory of martensitic transformation” developed by Wechsler, Lieberman and Read (WLR theory) [51,52]. In this theory, the transformation is seen as a deformation of the parent phase and deformation is expressed with the help of matrix. The total deformation matrix in the transformation is a product of lattice rotation matrix, lattice invariant shear matrix and a lattice deformation matrix from parent to martensite.

When a martensitic transformation happens in the parent phase, large amount of strain is generated around the martensite. This strain is accommodated either by introduction of slip or by introduction of twins. Both processes generate an inhomogeneous shear without

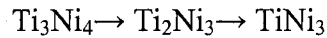
changing the structure of the martensite and that is why it is termed as lattice invariant shear. Whether slip or twin is introduced depends on the alloy system, prior thermal and loading history. In general, twin is generated first while transformation takes place. When twin forms, there is a plane between parent and martensite phase, which is undistorted and unrotated. This invariant plane is called habit plane. The situation is shown schematically in **Figure 2.4** [37]. Twins are normally three types – type I, type II and compound twins.

**Figure 2.5** [37] shows the lattice structure change in a cubic (B2) to monoclinic (B19') martensitic transformation prevalent in solution treated binary TiNi alloy systems. The whole process can be divided into two simple steps, even though in reality everything happens as a single step. If a tetragonal structure is imagined in the parent phase within the four unit cells shown, upon transformation  $[\bar{1}00]_p$ ,  $[01\bar{1}]_p$  and  $[0\bar{1}\bar{1}]_p$  shrinks to form the three lattice parameters a, b, c of the transformed structure. Finally, a shear on  $(011)_p$  plane in  $[100]_p$  direction makes the  $\beta$  angle from  $90^\circ$  to  $96.8^\circ$  and the monoclinic structure is formed.

### 2.2.2. Phase Diagram of TiNi Alloy and Diffusional Transformation

The phase diagram of TiNi alloy system is important to understand the heat treatment of this alloy and the dependence of shape memory and pseudoelastic property on the heat treatment. The TiNi phase diagram had been controversial for many years. Massalaski et al. [53] have established the phase diagram fairly. After that, Otsuka et al. [54] have modified the phase diagram slightly, and the resulting phase diagram is shown in **Figure 2.6**. They have argued that the eutectoid decomposition of TiNi to  $Ti_3Ni_4$  and  $Ti_2Ni_3$  proposed by Massalaski et al. [53] is not correct. Instead, they have concluded that  $TiNi_3$  is a stable phase

in the phase diagram and  $\text{Ti}_3\text{Ni}_4$  and  $\text{Ti}_2\text{Ni}_3$  phases are intermediate phases which appear in the following order with the increase in ageing time.



The effect of diffusional transformation to these intermediate phases with ageing time on martensitic transformation and shape memory behaviour will be further reviewed in the section 2.2.3.3. To observe the pseudoelasticity and shape memory, we are interested in the region bounded by  $\text{Ti}_2\text{Ni}$  and  $\text{TiNi}_3$ . In this region, the  $\text{TiNi}$  forms a complete solid solution with Ni solubility depending on the temperature. At 1090 °C, an order-disorder transition from B2 to BCC for  $\text{TiNi}$  is seen.

### **2.2.3. Factors Affecting the Martensitic Transformations**

Martensitic transformation determines almost all important properties of shape memory alloys. Transformation temperature determines at what temperature (range) such effect can be observed. This is very important for practical applications. For example, if room-temperature application of superelasticity effect is desired, it is necessary to make the alloy to have subzero transformation temperature. However, the transformation temperature cannot be too low; otherwise, it is too hard to induce the transformation and the associated large strain. The different factors that affect the transformation temperatures are reviewed in the following subsections.

#### **2.2.3.1. Effect of Compositional Change**

By changing the composition of the  $\text{TiNi}$  alloys and  $\text{TiNi}$  based alloys, the transformation temperatures and transformation path (single-step or two-step) can be changed to suit the practical need. Although it is possible to change the transformation

temperature and the transformation path by alloying elements [55, 56] in case of ternary TiNi alloys system, changing the Ni concentration alone is good enough to control the transformation in TiNi alloys, which is dealt in section 2.2.3.3. The two important alloying elements in TiNi based alloys are Fe and Cu.

Miyazaki et al. [57] have shown that substituting few percentage Ni in TiNi alloys by Fe the transformation path changes from one step ( $B2 \leftrightarrow B19'$ ) to two step transformation ( $B2 \leftrightarrow R \leftrightarrow B19'$ ). The effect of Cu addition in TiNi alloys are studied by Lo et al. [58]. Using electrical resistivity, DSC and XRD measurements, they have shown that up to 4% of Cu addition changes the transformation path to a two-step transformation and the martensitic transformation temperatures decreases to a very low temperature.

The other alloying elements also affect the transformation temperatures and the transformation paths of TiNi alloys. However, Pd, Pt, Hf, Au, and Zr increase the transformation temperatures and these ternary shape memory alloys are being used as high temperature shape memory alloys [59].

### **2.2.3.2. Effect of Cold Working**

Traditional cold working affects the martensitic transformation temperatures and the final microstructure obtained in TiNi alloys substantially [60-64]. By internal friction, shear modulus measurement and TEM study, Lin et al [60] have studied the effect of cold rolling on martensitic transformation of an equiatomic TiNi alloy. Because of cold rolling up to 40%, the martensite stabilisation takes place and dislocations network generated during rolling depresses the transformation temperatures. The hardness increases from 200 Hv to 415 Hv after 40% reduction in thickness. However, the effect of martensite stabilisation dies

out when the alloys was heated to 250 °C and the reverse transformation takes place. In another study [61], they use cold rolling and annealing to strengthen the equiatomic TiNi alloy. They carried out rolling to give 5%, 10%, 20% and 40% thickness reduction of an equiatomic TiNi alloy. The reported hardness increase for 40% cold rolled sample was from 200 Hv (sample with no cold rolling) to 320 Hv and the shape recovery measured by bending test increases from 90% to 100% with an applied bending strain of 4.5%. Kurita et al. [62] did a similar type of study using DSC measurements on equiatomic alloy. They have also found that with cold working the peak broadening of the transformation peaks take place and the broadening increases with the increase in percentage reduction in rolling.

Chang et al. [64] have also studied the effect of cold rolling on martensitic transformation in an equiatomic TiNi alloy. They have reduced the specimen thickness from 1.9 mm to 1.24 mm giving 35% reduction in thickness. They related the grain size reduction during cold rolling to the multi-stage transformations obtained using DSC and dynamic mechanical analyzer (DMA) measurements. They observed that the grain size distribution in the rolled materials is quite inhomogeneous and at the central area of the cross section of the material has larger grains comparatively, than the grains seen at the rolled surface. They concluded that due to this grain size variation, the transformation takes place at two different temperatures and that is why a four-stage transformation is seen in DSC study as shown in **Figure 2.7**.

During cooling at about 31 °C, a relatively small volume corresponding to the central large grain region transforms from B2 to R<sub>1</sub> first. Further cooling to 20 °C, the untransformed B2 region corresponding to smaller grain size region starts transforming from B2 to R<sub>2</sub>. Upon continuation of cooling, at about 6 °C the R<sub>1</sub> transforms to B19' and at about 16 °C the R<sub>2</sub>

transforms to B19'<sub>2</sub>. The R<sub>1</sub>, R<sub>2</sub> and B19'<sub>1</sub>, B19'<sub>2</sub> are same as R phase and B19' phase respectively, but transformed at two different regions and at two different temperatures. During reverse transformation however, B19'<sub>2</sub> and B19'<sub>1</sub> transform back to B2 phase directly at 39.3 °C and 50.8 °C, respectively. The similar four stage transformations (two two-stage B2 → R → B19') are not seen when the same sample was ground to reduce the thickness of the sample and remove the central bigger grain size region.

It is also reported in the literature [65-68] that with cold rolling the TiNi alloys exhibit crystal to amorphous transformation. Koike et al [65] have studied crystal to amorphous transformation in Ti 50.8at.% Ni alloy using TEM. In this study, they have discussed the driving force for this amorphous transition. They have roughly estimated that the elastic energy caused by the dislocation density of 10<sup>14</sup> /cm<sup>2</sup> is of the same order as the crystallisation energy in TiNi alloys. Based on this estimation they concluded that accumulation of high dislocation density (10<sup>13</sup> to 10<sup>14</sup> /cm<sup>2</sup>) during rolling is the driving force for amorphisation in cold rolled TiNi alloys.

Nakayama et al. [66,67] have studied the effect of cold rolling on the amorphous structure formation of a homogenised Ti 50.2at.% Ni alloy. In as-rolled condition no martensitic transformation was seen at 123 K when the sample was cooled at DSC. Using TEM study they have shown that with 70 % rolling reduction partial amorphisation takes place and the austenite stabilisation takes place. Subsequent annealing makes the structure nanocrystalline and the grain size increase with increasing annealing temperature. **Figure 2.8** [67] shows the TEM micrographs of Ti 50.2at.% Ni alloy after various processing conditions.

Recently, Nam et al. [68] have done a similar study on equiatomic TiNi alloy. Cold rolling at room temperature up to 40 % thickness reduction showed individual domain of



amorphous structure, whereas, in case of 70% rolling reduction band shaped amorphous region was seen among the crystalline area as seen in **Figure 2.8(b)**. They have also reported that with increasing the rolling reduction from 40 to 70%, the crystallisation temperature was decreased from 552 K (279 °C) to 539 K (266 °C). The average grain size after 40 % cold rolling and annealing at 250 °C was 27 nm, which increased to 80 nm when the annealing temperature was increased to 400 °C.

### **2.2.3.3. Effect of Post Deformation Annealing or Ageing**

As seen by the phase diagram in **Figure 2.6** [54] binary TiNi alloy is an intermetallic compound, which shows certain solubility of Ni as a function of temperature up to 58 at.% at 1116 °C, however, similar solubility of Ti is absent. By taking advantage of the Ni solubility in the TiNi matrix, the transformation behaviour can be controlled. In Ni-rich TiNi alloys when quenched from high temperature, the matrix becomes supersaturated with Ni. At low temperature, the Ni solubility is much lower than that at high temperatures (around 1000 °C solubility is 55 at.%). Otsuka et al. [37] have shown that various intermediate phases ( $\text{Ti}_3\text{Ni}_4$ ,  $\text{Ti}_2\text{Ni}_3$ ,  $\text{TiNi}_3$ ) form when the alloys are aged after solution treatment. The Ni dependence of martensitic transformation temperature in binary TiNi alloys is shown in **Figure 2.9** [37].

During aging, the formation of precipitates depends on ageing temperature and time. At lower ageing time (less than 5 h) and lower temperature (typically less than 600 °C),  $\text{Ti}_3\text{Ni}_4$  is formed first. While at higher ageing temperature (around 800 °C) and higher time (beyond 10 h)  $\text{TiNi}_3$  phase appears and at intermediate ageing time and temperature  $\text{Ti}_2\text{Ni}_3$  phase appears. The size and the number of precipitates also increase with ageing time and temperature. When these precipitates form depending on the ageing time and temperature, Ni

content in the matrix varies locally. This results in a two-step ( $B2 \rightarrow R \rightarrow B19'$ ) transformation unlike in the quenched alloys, which exhibit a single step transformation ( $B2 \rightarrow B19'$ ).

Recently, Eggeler et al. [69] have studied the effect of ageing on martensitic transformations in Ni rich TiNi alloys. Using DSC, TEM and neutron diffraction (ND) results, they have shown that transformation behaviour of these alloys is very sensitive to the microstructure of these alloys, which is dependant on ageing temperature and ageing time. They have found that Ti 50.8at.% Ni alloy, upon ageing at 450 °C shows first a two-step transformation at shorter ageing time (15 min to 1 h.) and then with increasing ageing time up to 5 h 3-step transformation is seen. Finally, at ageing time between 25 and 400 h two-step transformation is seen. During 3-step transformation the first and second peak is associated with the normal R phase and B19' phase transformation and the third peak is also for B19' phase transformation. However, this peak occurs at a lower temperature than the former two peaks due to microstructural heterogeneity. The authors termed this phenomena 2-3-2 transformation behaviour with increasing ageing time. Eggler et al. [69] have attributed the reason for this type of transformation behaviour to the homogeneous (precipitates form throughout the grain boundary and grain interior) and heterogeneous (precipitates form selectively at or near grain boundary) precipitation in the microstructure resulting in local composition variation.

### **2.3. Severe Plastic Deformation (SPD)**

The desire for improving the mechanical properties of the structural materials, followed by well know Hall-Petch [70] relationship have generated a lot of interest among

the materials scientists to produce the sub-micron level grain structures, typically less than 100 nm, also called nanocrystalline materials. Materials with grain sizes between 100 nm - 1000 nm are called ultra-fine grained (UFG) materials. There has been a great amount of research on large strain plastic deformation. A number of researchers have worked on how the large strain plastic deformation induced nanostructures change the flow stress, hardness, ductility and texture [71-73]. These authors' work have established that heavy deformations using cold rolling, drawing and torsion can result in a refined microstructure at room temperature. However, the structures formed at room temperature are usually substructures of a cellular type having boundaries with low angle misorientations. At high strains ( $>5$ ) only stable or quasi-stable nanograins with high angle grain boundaries are obtained. Another limitation of these conventional deformation techniques is that they involve reductions in the material dimensions, resulting in thin sheets in case of rolling, or filaments in case of extrusion. These final products have little practical utility as structural material.

Since Glieter [74] presented the concept of nanocrystalline materials two decades ago, many researchers have put effort to produce nanocrystalline or submicron grain structured materials in various ways in addition to SPD. These techniques include gas condensation [74], high-energy ball milling or mechanical alloying [75,76]. However, both of these techniques have their own limitations in terms of sample size and porosity. Alternatively, it has been found that applying a very high plastic strain, submicron grain structure can be produced in wide variety of materials including pure metals, metallic alloys and intermetallic materials [77-80]. Because of high strain applied (equivalent strain going up to 12) in these processing techniques, they are called severe plastic deformation technique

(SPD). High-pressure torsion (HPT) and equal channel angular pressing (ECAP) are the most well known methods of SPD capable of deforming with true strain  $\geq 10$  [81].

### 2.3.1. Equal Channel Angular Pressing (ECAP)

This method is used in the present work to achieve nanocrystalline TiNi alloy, hence it is appropriate to reproduce the details here about this method. In ECAP method, two equal cross-section channels intersect each other at a particular angle and a billet is deformed through this channel. Segal and co-workers [81,82] first invented the method in 1981. The initial goal in this process was to introduce large amount of plastic strain in the material without any reduction in cross section so that the applied strain can be multiplied by deforming the material through a number of cycles. This still remain the main advantage of this process. The deformation in this process happens purely by simple shear. Since its inception, there are many varieties of the process, which include whether, the billet was pressed or drawn and deformation path in subsequent cycles. If the billet is drawn then the process is called equal channel angular drawing [83] and if the billet is punched, then the process is equal channel angular extrusion (ECAE).

**Figure 2.10** [84] shows the three different possibilities of ECAP die design schematically where one edge of two channels intersect each other at an angle,  $\Phi$ , ranging between  $90^\circ$  and  $135^\circ$ . The outer edge of the channels creates three different possibility of the design depending on the corner angle ( $\Psi$ ) at which they intersect.  $\Psi = 0$  and  $\Psi = \pi - \Phi$  corresponds to the two limiting condition for any given  $\Phi$  and in third possibility,  $\Psi$  can take any value between the limiting conditions. The process is generally carried out at low temperature. However, for difficult-to-plastically-deform materials high temperature processing or intermediate annealing between the ECAP cycles is also common [85]. The

channel wall generates a lot of friction during the process, which is taken care by applying suitable lubrication depending on the strength of the pressed material and temperature.

### **2.3.2. Processing Routes and Microstructure Development during ECAP**

There are different processing routes in conventional ECAP where rods and square bars are pressed through the channel for multiple numbers of passes. **Figure 2.11** [86] shows three different processing routes which are named as route A, route B and route C. In route A, the sample is not rotated along its longitudinal axis during successive passes. In route B, the sample is rotated about its longitudinal axis either clockwise or anticlockwise during subsequent passes. Depending on whether the sample is rotated clockwise-anticlockwise ( $\pm 90^\circ$ ) or only in clockwise direction ( $+ 90^\circ$ ) route B is further termed as route B<sub>A</sub> or B<sub>C</sub>, respectively. In route C, the sample is rotated  $180^\circ$  about its longitudinal axis in between each pass.

There have been a number of researches dealing with the microstructural changes in the materials when different processing routes are employed. Iwahasi et al. [86] have studied carefully the grain refinement technique and nature of ultrafine grain structures developed in high purity aluminum during ECAP when the samples are rotated between the successive pressing through  $0^\circ$  (Route A),  $90^\circ$  (route B<sub>C</sub>) and  $180^\circ$  (route C). Using transmission electron microscopy, they have shown that microstructure development depends on the angle of rotation between each pressing. Route B generates an array of high angle grain boundaries most rapidly. The evolution is slower in case of route C and is slowest in route A when the sample is not rotated between each pass. The grain size reduction was from 1 mm to 0.5-1.5  $\mu\text{m}$  in all three processing routes. Chakkingal et al. [87] have found similar results while equal channel angular drawing as cast commercially pure aluminum and with a die angle of

$\Phi=135^\circ$ . They concluded that the route A produces elongated sub-grains, whereas route B and route C results in equiaxed sub-grains. However, they reported that grain boundary misorientation was only about  $1-4^\circ$  and they attributed the probable reason to the die angle being  $135^\circ$ .

Gholinia et al. [88] have also studied the effect of different processing routes on microstructure evolution during ECAP of Al-Mg and Al-Mn alloy with a die angle of  $\Phi=120^\circ$ . They have studied all four different processing routes and characterise the microstructures using electron back scattered diffraction (EBSD) technique. They have concluded different results than Iwahashi et al [86]. They have argued that by maintaining a constant strain path i.e. route A is the most efficient technique for forming submicron grain structure. Route B<sub>A</sub> and route B<sub>C</sub> were less efficient than route A in terms of producing new high angle grain boundaries during subsequent passes and route C was the most inefficient route for grain refinement. They also showed route A produces elongated grain structure and route B produces bimodal grain structure comprised of larger grains and concentrated bands of submicron grains.

### 2.3.3. Strain Calculation during ECAP

The strain induced in the material during ECAP varies largely with the angles at which the channels intersect. In **Figure 2.10(a)** [84], where  $\Psi=0$  the shear strain is given by,

$$\gamma = 2 \cot\left(\frac{\Phi}{2}\right) \quad (2.1)$$

**Figure 2.10(b)** [84], representing the other limiting condition where  $\Psi=\pi-\Phi$ , the shear strain is given by,

$$\gamma = \Phi \quad (2.2)$$

In case of an intermediate situation in **Figure 2.10(c)** [84], the shear strain is given by,

$$\gamma = 2 \cot\left(\frac{\Phi}{2} + \frac{\Psi}{2}\right) + \Psi \cos \text{ec}\left(\frac{\Phi}{2} + \frac{\Psi}{2}\right) \quad (2.3)$$

By inspection, it is observed that equation 2.3 reduces to equation 2.1 when  $\Psi=0$  and equation 2.2 when  $\Psi=\pi-\Phi$ . From mechanics, the equivalent strain,  $\varepsilon_{eq}$  is represented by,

$$\varepsilon_{eq} = \left[ \frac{2}{3} \left[ \varepsilon_x^2 + \varepsilon_y^2 + \varepsilon_z^2 + \frac{\gamma_x^2 + \gamma_y^2 + \gamma_z^2}{2} \right] \right]^{1/2} \quad (2.4)$$

Because of accumulative nature of the strain during ECAP the total strain after a certain number of pass can be obtained by multiplying the strain at each pass by the total number of pass. By substituting the proper values in equation 2.4, the equivalent strain after  $N$  number of ECAP passes,  $\varepsilon_N$  can be obtained by the following equation:

$$\varepsilon_N = \left[ \frac{2 \cot\left(\frac{\Phi}{2} + \frac{\Psi}{2}\right) + \Psi \cos \text{ec}\left(\frac{\Phi}{2} + \frac{\Psi}{2}\right)}{\sqrt{3}} \right] \quad (2.5)$$

A detailed derivation of the strain generated during each pass can be found elsewhere [84]. As seen from equation 2.5, strain during each pass is dependant on  $\Phi$  and  $\Psi$  alone. In **Figure 2.12**, the calculated equivalent strain variation against the corner angle,  $\Psi$ , for three different  $\Phi$  values is shown. From this figure, it is quite clear that angle  $\Phi$  has a greater effect on the strain induced during ECAP than the corner angle,  $\Psi$ .

Nakashima et al. [89] have studied experimentally, the influence of channel angle,  $\Phi$ , on the development of ultrafine grains. With four different channel angles and a slightly different corner angle in each die, they have studied the microstructure development in pure aluminum. They concluded that the die having  $90^\circ$  channel angle and with route  $B_C$  gives the most refined microstructure at low number of passes. The die having the largest channel angle of  $157.5^\circ$  was worst in both generating refined grain structure and in achieving inferior mechanical properties.

#### **2.3.4. Severe Plastic Deformation on TiNi alloys**

Even though the technique of severe plastic deformation is well established, to produce ultrafine grain or nanocrystalline bulk TiNi, researchers did not apply this technique until very recently. Pushin et al. [90-94] have studied the structure formation and phase transformation in TiNi based alloys ( $Ti_{50}Ni_{50}$ ,  $Ti_{49.5}Ni_{50.5}$ ,  $Ti_{50}Ni_{49}Fe$ ,  $Ti_{50}Ni_{25}Cu_{25}$ ,  $Ti_{49.4}Ni_{50.6}$ ). They have deformed the material using SPD technique namely high pressure torsion, ECAP and multi-step SPD deformations – ECAP plus cold rolling [94] both at room temperatures and at high temperatures in the range of  $350-500^\circ C$ . During ECAP, the strain at each pass was about 1.0 and ECAP was continued up to 5-10 passes. Using TEM study they have shown the structure in binary  $Ti_{49.5}Ni_{50.5}$  alloys, especially after ECAP at  $450^\circ C$  consists of average grain size of  $0.2-0.3 \mu m$ . The alloy under all processing conditions undergoes two-step  $B2 \leftrightarrow R \leftrightarrow B19'$  type martensitic transformations. Using in situ XRD and TEM study they have established that both R phase and  $B19'$  phase have a packet morphology consisting of platelike crystals twinned in pair.

Khemelevskaya et al. [95] have also studied the effect of HPT and ECAP on the microstructural formation and recovery strain and recovery stress in both Ti-rich and Ni-rich



TiNi alloys. Recovery strain was measured by heating of samples after bending at 0 °C around mandrels and the recovery stress was measured during heating of the samples which was deformed in tension prior to heating. They found that after doing ECAP at 450 °C for 6-8 passes the recoverable strain increases from 2% to 4% and 8% in case of Ti<sub>50.6</sub>Ni<sub>49.4</sub> and Ti<sub>49.8</sub>Ni<sub>50.2</sub>, respectively. They attributed this increase in recovery strain because of increase in the yield strength of the martensite and increase in difference between the yield strength of the martensite and critical stress for martensite formation or reorientation. For the Ni rich alloy after 8 passes, they found the grain size to be 0.1-0.3 μm.

Stolyarov et al. [96] also studied the SPD of TiNi alloys similar to that of Khemelevskaya et al. [95] with Ti<sub>49.8</sub>Ni<sub>50.2</sub> alloy but with a die of channel angle,  $\Phi=110^\circ$  which induces much lower strain than in the previous studies of other researches as detailed above. Using TEM characterisation, they found that first 1-4 passes results in sharp grain refinement (from 80 μm to 0.45 μm). The subsequent passes does not affect the sub-grain size drastically, as after 8 passes the grain size reduced to 0.24 μm and after 12 passes it was 0.23 μm. However, the subsequent passes beyond 4 passes increase the density and distribution of dislocation and amount of internal stresses. The martensitic transformation sequence observed was also a usual two-step  $B2 \leftrightarrow R \leftrightarrow B19'$  transformation. The transformation temperatures decreases after 4 ECAP passes by 20 – 40 °C when compared to as-received sample and then again increases slightly after 8 passes. They have also reported the increase in yield strength and the stress required to martensite formation or reorientation as shown in **Table 2.2**. This increase in mechanical properties results in higher recovery than the as quenched alloy and the post deformation annealing of the ECAP alloy retains the high strength.

**Table 2.2. Effect of ECAP pass and subsequent annealing on the room temperature mechanical properties of Ti 50.2at.% Ni alloy [96 ].**

<b>Deformation state</b>	<b><math>\sigma_m</math>, MPa</b>	<b><math>\sigma_u</math>, MPa</b>	<b><math>\sigma_{0.2}</math>, MPa</b>	<b>% elongatio</b>	<b><math>(\sigma_{0.2} - \sigma_m)</math>, MPa</b>
Quenched	210	940	600	40	390
ECAP 450 <sup>0</sup> C, 8 Passes	290	1240	1140	25	850
ECAP 450 <sup>0</sup> C, 8 Passes, ageing 450 <sup>0</sup> C	320	1240	1180	33	860
ECAP 450 <sup>0</sup> C, 8 Passes, ageing 500 <sup>0</sup> C	350	1260	1160	50	810
ECAP 450 <sup>0</sup> C, 8 Passes, ageing 600 <sup>0</sup> C	240	1150	860	67	620

Xie et al. [97] have studied the change in transformation temperatures in Ti 50.3at.% Ni subjected to ECAP process with an equivalent strain of 1 in each pass at 550<sup>0</sup>C. They showed that after two ECAP passes at higher temperature when there is no precipitation takes place the transformation temperature decreases. However, when the alloy is annealed for long time and there is precipitation of Ti<sub>3</sub>Ni<sub>4</sub> in the matrix, the Ni depletes from the matrix and the transformation temperature increases again.

Karaman et al. [98] studied the transformation behaviour and unusual twinning in Ti 50.8at.% Ni alloy subjected to ECAP at room temperature and at 450<sup>0</sup>C. Using DSC study they have shown that there is no transformation seen when the alloys was subjected to room temperature ECAP between -60<sup>0</sup>C and 600<sup>0</sup>C. However, when the alloy was subjected to ECAP at high temperature the martensitic transformations were seen and the transformation temperatures have increased than that of as received alloy.

To summarise this section briefly, all the previous work on SPD of TiNi alloys by various authors indicates that the transformation path changes to two-step **B2 → R → B19'** type transformation. The transformation temperatures decrease after the

deformation due to austenite stabilisation when there is no precipitation and the transformation temperatures increase when there is precipitation associated with the deformation process sequence in case of Ni rich TiNi alloys. The yield strength, ultimate strength and the transformation stress also increases after ECAP processing at high temperature. There is substantial amount of grain size reduction after ECAP; the grain sizes reported in the previous work [90-98] varies from 0.1 to 0.3  $\mu\text{m}$ .

### 2.3.5. Why Severe Plastic Deformation of TiNi alloys

All the above study shows that with the help of severe plastic deformation or equal channel angular pressing to be specific, amorphous and nanocrystalline or ultrafine grained TiNi alloys can be produced. The nanocrystalline structure exhibits better mechanical properties in terms of yield strength and recovery strain. In addition, the martensitic transformation temperatures and the transformation paths can also be controlled by applying the optimum thermo- mechanical treatment. The schematic diagram representing the shape memory and transformation pseudoelasticity region in stress-temperature space as shown in **Figure 2. 13** [99] can best explain the effect of the increased yield strength in the pseudoelasticity of TiNi alloys.

It can be seen from the **Figure 2.13** that the critical stress to induce martensite increases with the increase in the temperature beyond  $A_f$  at any given applied stress. There are two parallel lines with negative slope representing the critical stress to introduce slip in the alloy. The solid line represents (situation A) the alloys which have a higher critical stress to introduce slip, typically Ni rich binary TiNi alloys and the dotted line represents those alloys which have very low critical stress to introduce slip, typically Ti rich binary TiNi alloys. Therefore, by deforming TiNi alloys using high strain severe plastic deformation and

achieving finer grain size, it is possible to increase the critical stress to introduce slip in the material. Eventually, the area of transformation pseudoelasticity in the stress-temperature space as shown in **Figure 2. 13** [99] can be increased. However, it is worth to mention that increasing yield strength also increases the elastic recovery in the alloy.

Saburi et al. [100] have studied the effect of grain size on pseudoelasticity of Ti 50.5at.% Ni alloy which was solutionised at 800 °C for 1 hour and then quenched. They have carried out uniaxial tensile testing on a single crystal specimen of the Ti 50.5at.% Ni alloy and on two other specimen of the alloy with a grain size of 50 µm and 1mm, respectively. **Figure 2. 14** shows the result of such uniaxial tensile tests. The tests were carried out at 40 °C, which was 10 °C above the  $A_f$  temperature (30 °C) of the alloy. From **Figure 2. 14**, it is clear that with decreasing grain size the pseudoelasticity increases.

#### **2.4. Instrumented Indentation and Shape Memory Effect**

Traditionally the measurement of shape memory recovery strain and pseudoelastic recovery strain is measured using uniaxial stress-strain experiments [101,102]. However, conducting these experiments is cumbersome and the sample size requirements often limit the traditional way of measuring the mechanical properties of shape memory materials processed under various conditions. Recently, researchers often select micro- and nanoindentation techniques to measure the shape memory and pseudoelastic strain recovery of shape memory alloys [19,20]. In instrumented indentation technique, load is applied on the material using an indenter and both applied load and the displacement of the indenter are recorded. These data are used to calculate mechanical properties like hardness (H) and Young's modulus (E). A various types of indenters are normally (spherical, Berkovich, sphero-conical, Vickers, Knoop) used in these experiments though, spherical and Berkovich

type of indenters are more commonly used. Oliver and Pharr [23,24] have proposed a method which is now widely used to measure the hardness and Young's modulus of various materials. In the following section, terminologies related to instrumented indentation and Oliver-Pharr method is introduced.

#### 2.4.1. Oliver-Pharr Method [23,24]

In this method, an indenter is used to apply the load on the surface of the material as shown in **Figure 2.15(a)** and (b). The total displacement of the indenter at any time during the indentation is given by,

$$h_m = h_c + h_s \quad (2.6)$$

Where,  $h_c$  is the contact depth and  $h_s$  is the displacement of the surface at the contact perimeter. It was assumed that while unloading the load-displacement profile obeys a power law relation as given by,

$$P = A(h - h_f)^m \quad (2.7)$$

Where  $P$  is indentation load,  $h$  is displacement at any given time,  $h_f$  is the final indentation depth at zero load, the constants  $A$  and  $m$  are fitting parameters determined by least square fitting of relationship between  $P$  and  $(h-h_f)$ . The three key parameters required to calculate the hardness and Young's modulus are the max load  $P_{max}$ , the depth at max load  $h_m$  and the initial unloading stiffness  $S$ , which can be calculated mathematically by differentiating equation 2.7 and taking the derivative at the peak load, as given by,

$$S = \left. \frac{dP}{dh} \right|_{h=h_{max}} \quad (2.8)$$

However in practice, the unloading stiffness,  $S$ , is measured from the load-displacement curve directly by drawing a tangent to the initial linear-unloading portion of the curve. The relation between  $S$  and the reduced Young's modulus  $E^*$  is given by the following equation [23,24],

$$E^* = \frac{S}{2} \sqrt{\frac{\pi}{A_c}} \quad (2.9)$$

Where,  $A_c$  is the projected contact area at maximum load and the reduced composite Young's modulus  $E^*$  is defined as,

$$A_c = f(h_c) \quad (2.10)$$

$$E^* = \left[ \frac{(1-\nu_s)^2}{E_s} + \frac{(1-\nu_i)^2}{E_i} \right]^{-1} \quad (2.11)$$

Where,  $\nu_i$ ,  $\nu_s$ ,  $E_i$ , and  $E_s$  are the Poisson's ratios and Young's moduli of the indenter and the samples. Now, from the definition of hardness  $H = P_{max}/A$ , we can see that knowing  $S$  and  $A_c$ , the hardness,  $H$  and Young's modulus of the sample,  $E_s$  can be calculated from the above equations. Another important point to be noted while using Oliver and Pharr [23,24] method is that the equation 2.10 is valid for a Berkovich indenter. While using a conical indenter that produce spherical indents or in case of spherical indenter, the contact area is directly calculated from the contact radius ( $a$ ). From the geometry of the spherical indentation as shown in the **Figure 2.15** (b) the contact radius,  $a$ , is calculated from the following equation:

$$a = \sqrt{2Rh_c - h_c^2} \quad (2.12)$$

## 2.4.2. Quantitative Characterisation of Shape Memory and Pseudoelastic Recovery

Using micro and nanoindentation techniques, it is possible to measure the shape memory recovery and pseudoelastic recovery. Cheng et al. [19,20,22], Shaw et al. [103] and Gall et al. [104] have showed that the load-displacement curves obtained in instrumented indentation technique can be used to characterise the shape memory recovery and pseudoelastic recovery quantitatively. **Figure 2.16** shows a typical load displacement curve wherein, various terminologies required for the calculation of recovery ratios are shown. The indentation-induced pseudoelastic depth recovery ratio,  $\eta_{PE}^h$ , is defined as,

$$\eta_{PE}^h = \frac{h_{max} - h_f}{h_{max}} \quad (2.13)$$

The pseudoelastic energy recovery ratio during indentation,  $\eta_{PE}^w$ , is defined as the ratio of recoverable work ( $W_r$ ) to the total work ( $W_t$ ) [20]:

$$\eta_{PE}^w = \frac{W_r}{W_t} = \frac{\int_{h_r}^{h_{max}} Pdh}{\int_0^{h_{max}} Pdh} \quad (2.14)$$

From practical point of view, the energy recovery ratio is a better representation of pseudoelasticity than depth recovery ratio, as the former is calculated by measuring the area under loading and unloading curve unlike in the later case where only a point on the load-displacement profile is considered in the calculation.

In case of shape memory recovery the indentation induced depth recovery ratio,  $\eta_{SME}^h$ , is calculated by measuring the maximum residual indent depth at zero load before heating,

$h_{max}^{BH}$ , and the maximum residual indent depth of the same indent after heating,  $h_{max}^{AH}$  and is given as [19],

$$\eta_{SME}^h = \frac{h_{max}^{BH} - h_{max}^{AH}}{h_{max}^{BH}} \quad (2.15)$$

## 2.5. Wear Behaviour of TiNi Alloys

In the literature TiNi alloys are explored for its macro- and micro-scale wear behaviour. On macroscopic scale, sliding wear [18,105-108] and corrosive wear [29,30] experiments are conducted. Liao et al [106] have studied the dry sliding wear behaviour of equiatomic TiNi alloy (martensitic at room temperature) and Ti 51at.% Ni (austenitic at room temperature) alloy against a hard steel ball with Pin-on-disk configuration. The experiments were conducted at different loads starting from 10 N to 60 N with an increment of 10 N and the sliding distance for all the tests were up to 600 m. They have concluded that martensite reorientation and pseudoelasticity enhance their wear resistance. They claimed that adhesion, abrasion, brinelling (wavy wear tracks) and surface fatigue are the four main mechanism of wear in TiNi alloys.

Using dry sliding wear experiments and finite element modelling (FEM), Li at al. [109-111] have studied tribological properties and wear mechanism of binary TiNi alloys and how pseudoelasticity helps in improving wear characteristics of TiNi alloys. In one study, they have compared the wear behaviour of a Ni rich TiNi alloy with 304-stainless steel and concluded that in case of low load experiments where pseudoelasticity is completely functional, the wear resistance is two orders of magnitude less than the stainless steel. Using SEM analysis, they have studied the characteristics of the worn surfaces. The alloy, which



had higher degree of pseudoelasticity (measured by indentation and tensile testing method) showed narrower plastic deformation bands. In addition the average surface roughness of the worn surface was lower in the alloy having higher degree of pseudoelasticity. When the load was increased such that the plastic strain exceeds the pseudoelastic strain limit, tensile strength, strain-hardening capacity and the fracture strain has a greater effect on wear resistance. Tensile strength and strain hardening capacity measured by uniaxial tensile testing showed that TiNi alloys were superior than the 304-stainless steel which makes the TiNi alloys more wear resistant than the stainless steel at higher loads.

In another study, Li et al. [111] have proposed a modified Archard's equation to predict the wear behaviour for highly elastic or pseudoelastic material, as given in the following equation:

$$V_{\text{loss}} = \left[ K_1 \frac{1}{d} + K_2 (1-\eta) d^2 \right] \frac{L_1}{L_2} s, \quad 0 < \eta < 1 \quad (2.16)$$

Where,  $K_1$  ( $\text{nm}^3$ ) and  $K_2$  (dimensionless) are constants,  $L_1$  and  $L_2$  the wearing load (i.e. the normal load) and indentation load, respectively,  $s$  the sliding distance.

Recently Qian et al. [112,113] have studied the micro-wear behaviour of pseudoelastic TiNi alloy (austenitic at room temperature) conducted using a Hysitron tribometer at temperatures ranging from 22<sup>o</sup> to 120<sup>o</sup>C. Using in situ AFM images analysis they have shown that at room temperature abrasive wear dominates the wear process. Abrasive wear by ploughing takes place beyond a threshold load for each type of indenter. Applying Hertzian contact theory, they have analysed the role of phase transformation and plasticity in room temperature wear of TiNi alloys and they concluded that indentation hardness of pseudoelastic TiNi alloy is not a single material property but it indicates the

material's ability against plastic deformation and phase transition. By carrying out indentations at different load and at different temperatures, they have developed a way of calculating the hardness. Using this model, they showed that the hardness of TiNi alloy actually increases with temperature, which is mainly due to the increase in transition stress. They have also conducted a series of micro-wear tests at different temperatures and the result show that with increasing temperature and increasing hardness the wear depth in TiNi alloys decreases. They have attributed this unusual behaviour to the interplay among the three temperature dependent factors: elastic modulus of austenite, phase transformation and plastic deformation below the indenter.

Ni et al. [114] have studied the effect of  $H/E^*$  ratio on the friction and wear behaviour of bilayer coatings where chromium, martensitic TiNi and austenitic TiNi are used as interlayer beneath a chromium nitride coating. In this study the coating with austenitic TiNi (termed in the original work as S1) had the highest  $H/E^*$  ratio and this material showed the minimum wear loss under dry sliding conditions with pin-on-disk geometry as shown in **Figure 2. 17**. Qualitatively, the effect of  $H/E^*$  ratio on friction has been explained by these authors [114] using pile-up and sink-in phenomena. For materials with large yield strength to Young's modulus ratio (equivalent to  $H/E^*$ ) tendency of sinking-in is observed and the vice-versa is true. Hence, in case of sink-in the ploughing force, which contributes to the friction in addition to adhesive force, is smaller than in case of pile-up.

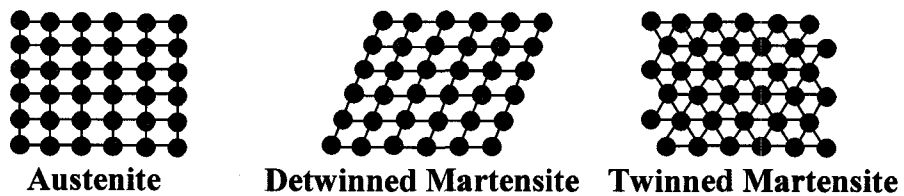
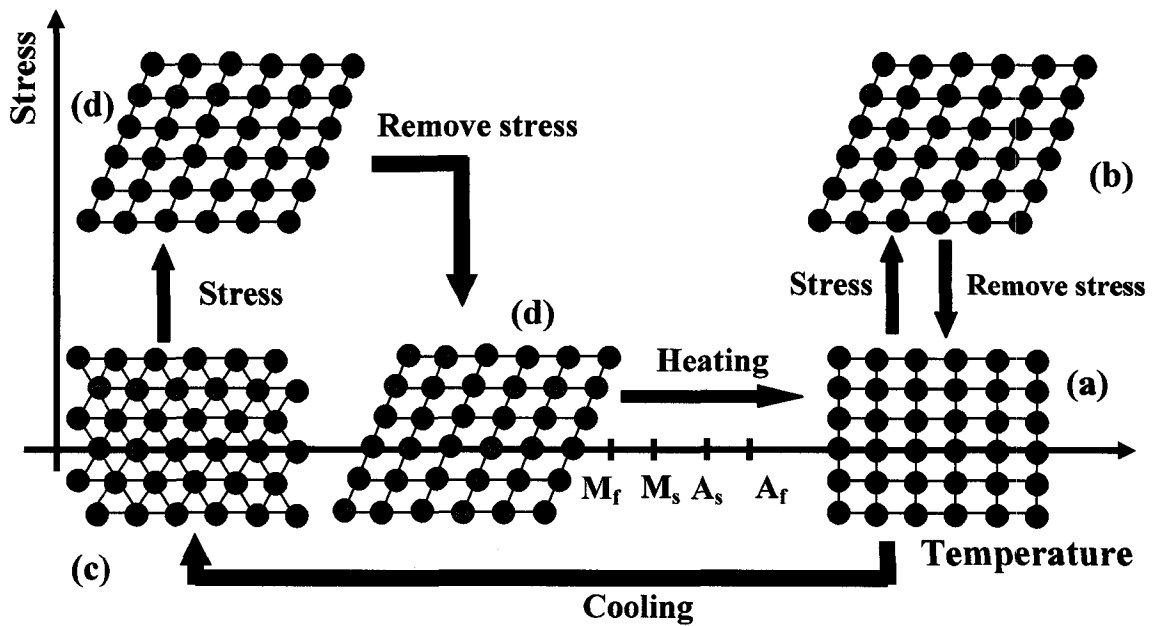
## **2.6. Executive Summary of Literature Survey**

The literature survey in this thesis on various aspects of TiNi alloys showed the following :

1. TiNi alloys possess superior mechanical properties compared to conventional materials.

2. The martensitic transformation path and the transformation temperatures depend on composition (at.% Ni and addition of ternary alloying elements), plastic deformation (both conventional and newer techniques like SPD) and post deformation annealing or ageing.
3. The TiNi alloys show improvement in mechanical properties (yield strength, true strength, % elongation, and strain recovery after mechanical unloading and/or thermal effects) after plastic deformation.
4. Cold rolling with subsequent annealing and ECAP at room temperature and high temperature produces ultra-fine grain structure to nanocrystalline structure.
5. The reduction in grain size is attributed to the increase in mechanical properties measured by simple uniaxial testing.
6. The TiNi alloy has potential to become an alternative to conventional wear resistant material, which is due to its thermally induced self-healing (SME) and mechanically induced self-healing (pseudoelasticity) property.

However, greater understanding of complex loading and the interplay between plastic deformation and stress induced martensitic transformation is required to take the benefit of the unique properties of these alloys successfully. Even though researchers have studied the self-healing effect during indentation loading and scratch loading there has not been much study to explore the possibility of using pseudoelasticity to achieve self-healing effect. Thus the objective of this work has been to enhance the mechanical properties of Ti 50.8at.% Ni alloy by reduction of grain size to nanometre level and achieve self-healing under indentation and scratch loading.



Phase in TiNi alloys	Structure
• Austenite (B2)	Cubic
• Martensite (B19')	Monoclinic
• Martensite (R)	Trigonal

**Figure 2.1. Appearance of shape memory effect and pseudoelasticity. Demonstration using a schematic diagram showing two dimensional crystal structures of austenite and martensite. (a) Austenite above  $A_f$ ; (b) SIM above  $A_f$ ; (c) twinned martensite below  $M_f$ ; (d) detwinned martensite below  $M_f$ . The nomenclature and the structure for various martensites are shown below.**

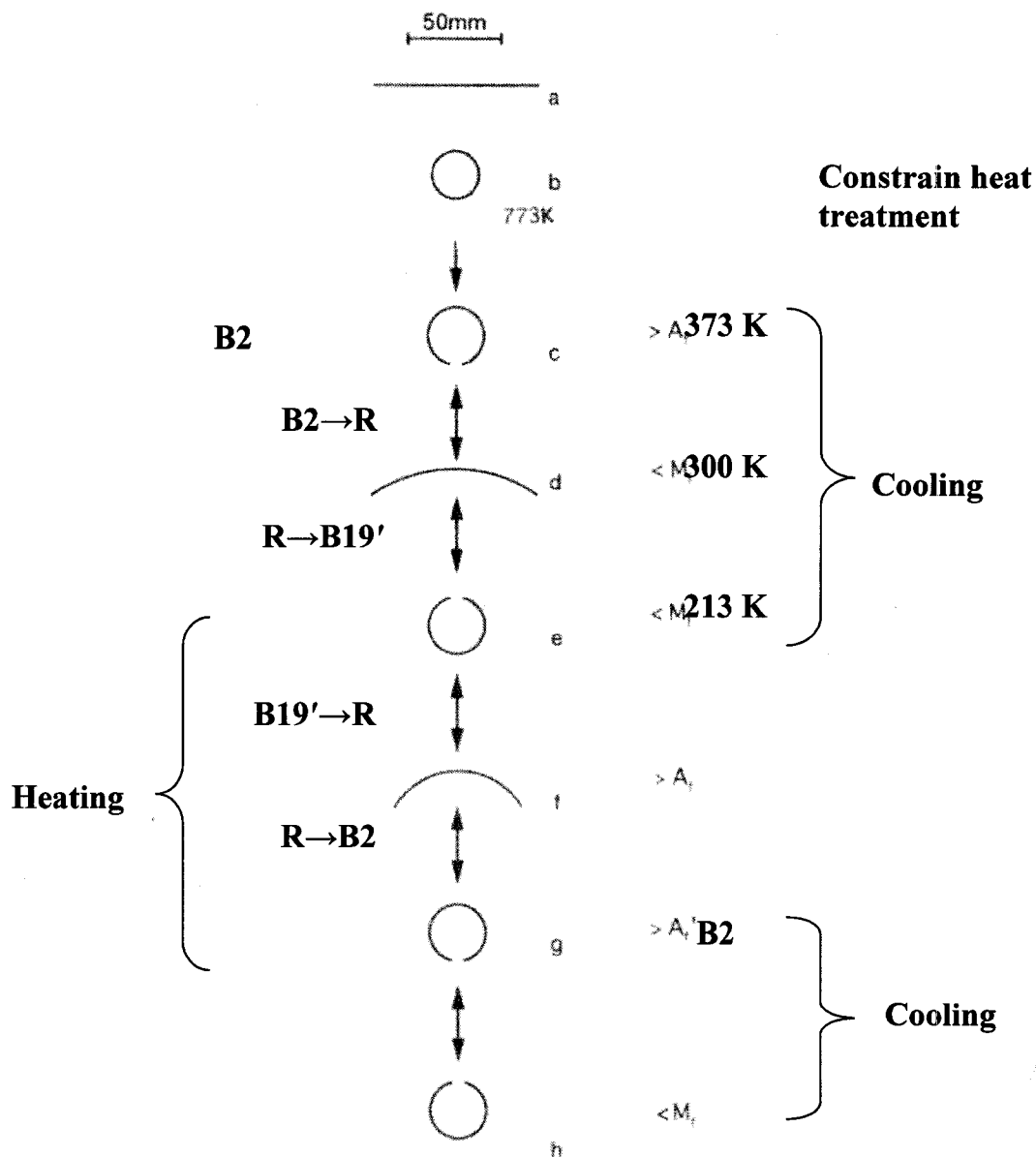


Figure 2. 2. Two way shape memory of a Ti 51 at.% Ni alloy; (a) 0.3 mm thick sheet; (b) sheet shape during constrain heat treatment; (c) shape of parent phase at 373 K; (d) intermediate shape during cooling to 300 K with R phase; (e) shape of B19' phase at 213 K; (f) intermediate shape with R phase during heating (g) shape of parent phase at 373 K; (h) shape of B19' phase after cooling down to 213 K. Note that shape of both parent and martensite phase is remembered [33].

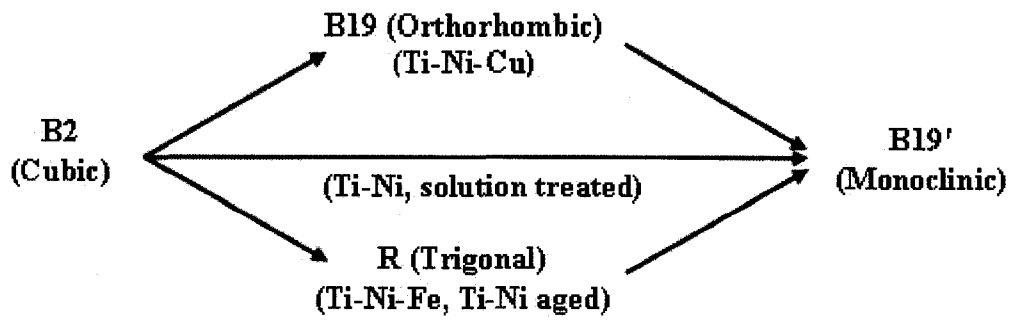


Figure 2. 3. Three transformation paths for TiNi based alloys [32].

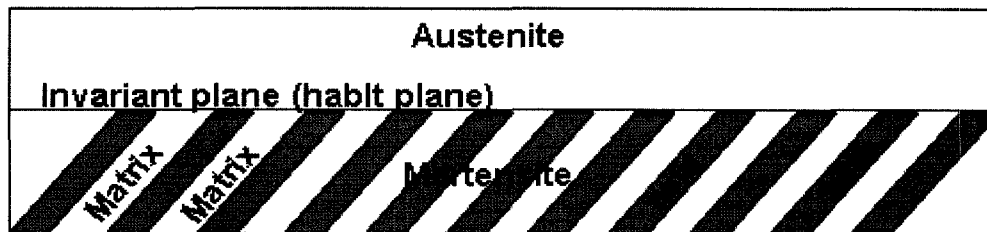


Figure 2. 4. Schematic diagram of existence of habit plane in austenite and martensite matrix [37].

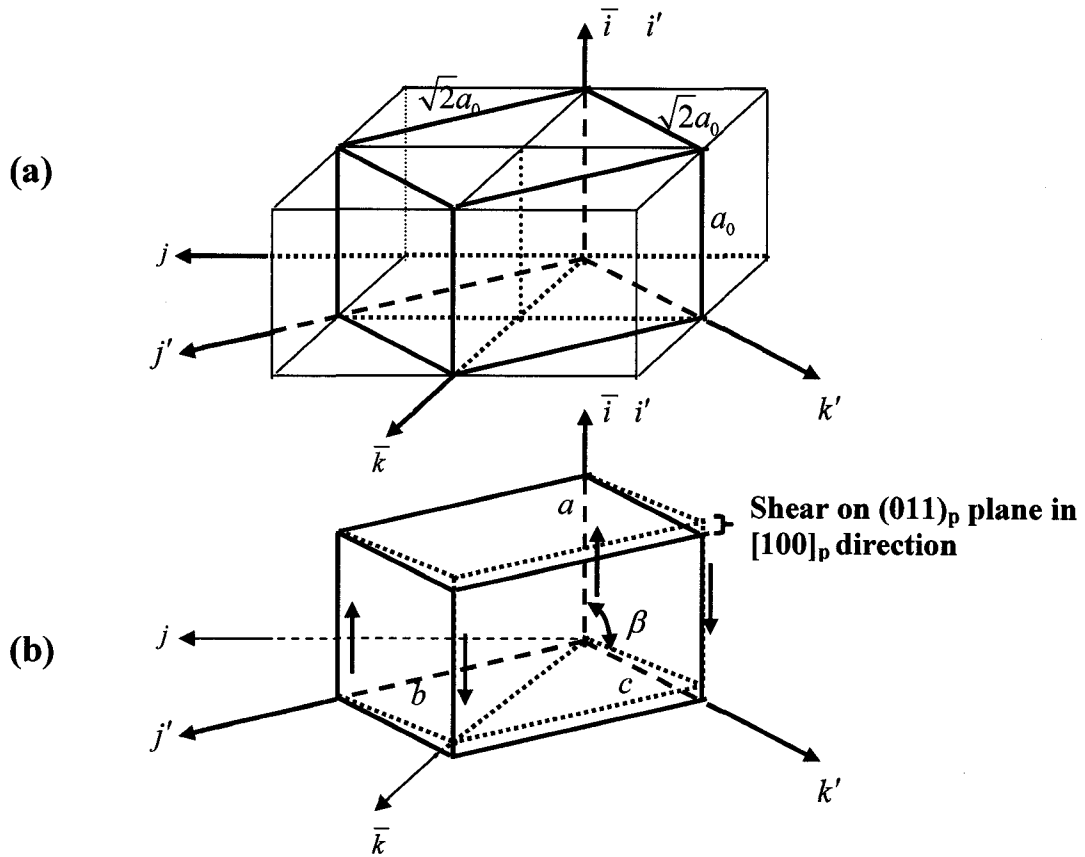


Figure 2. 5. The lattice change from B2 parent phase, (a) to B19' martensite phase, (b)  $i, j, k$  refers to parent lattice and  $i', j', k'$  refers to the martensite lattice. A shear on  $(011)_p$  plane converts the parent structure into B19' martensite structure [37].

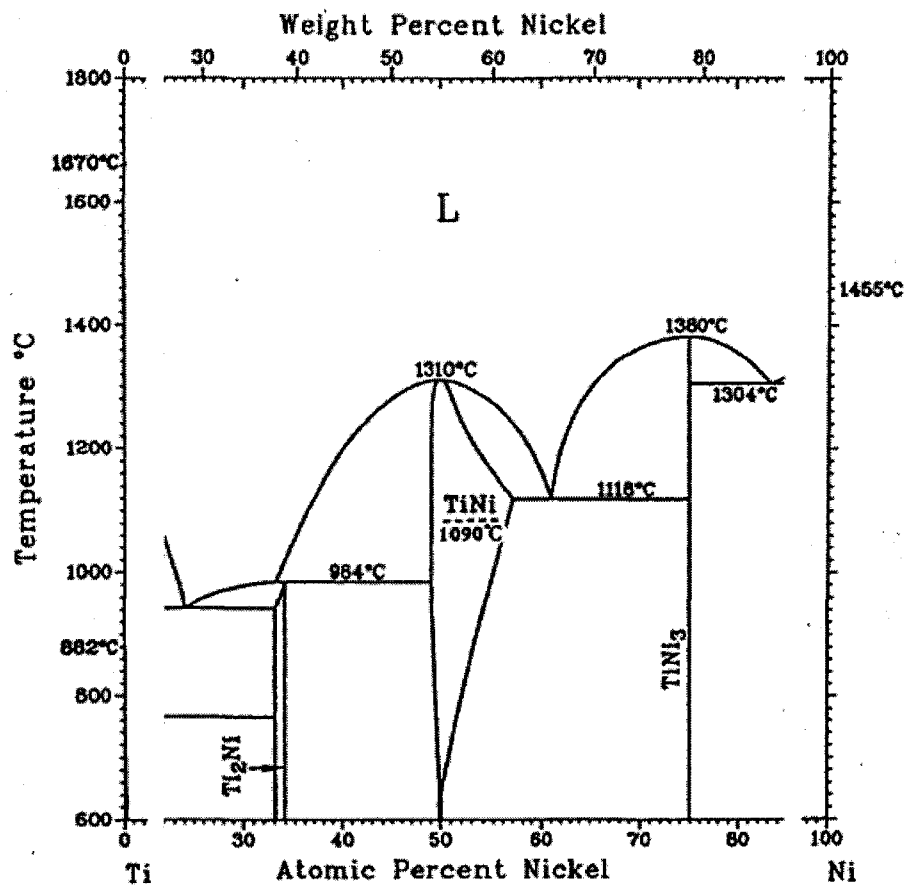


Figure 2. 6. The phase diagram of TiNi binary alloys by Otsuka et al. The dotted line represents the order-disorder transition for TiNi alloys at 1090<sup>0</sup> C [54].



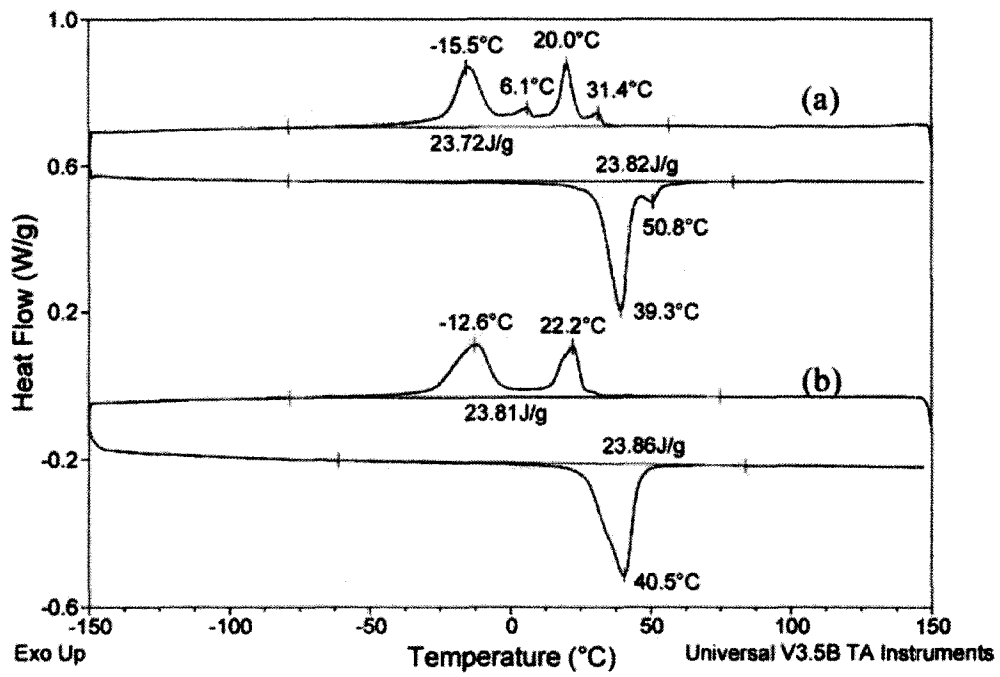
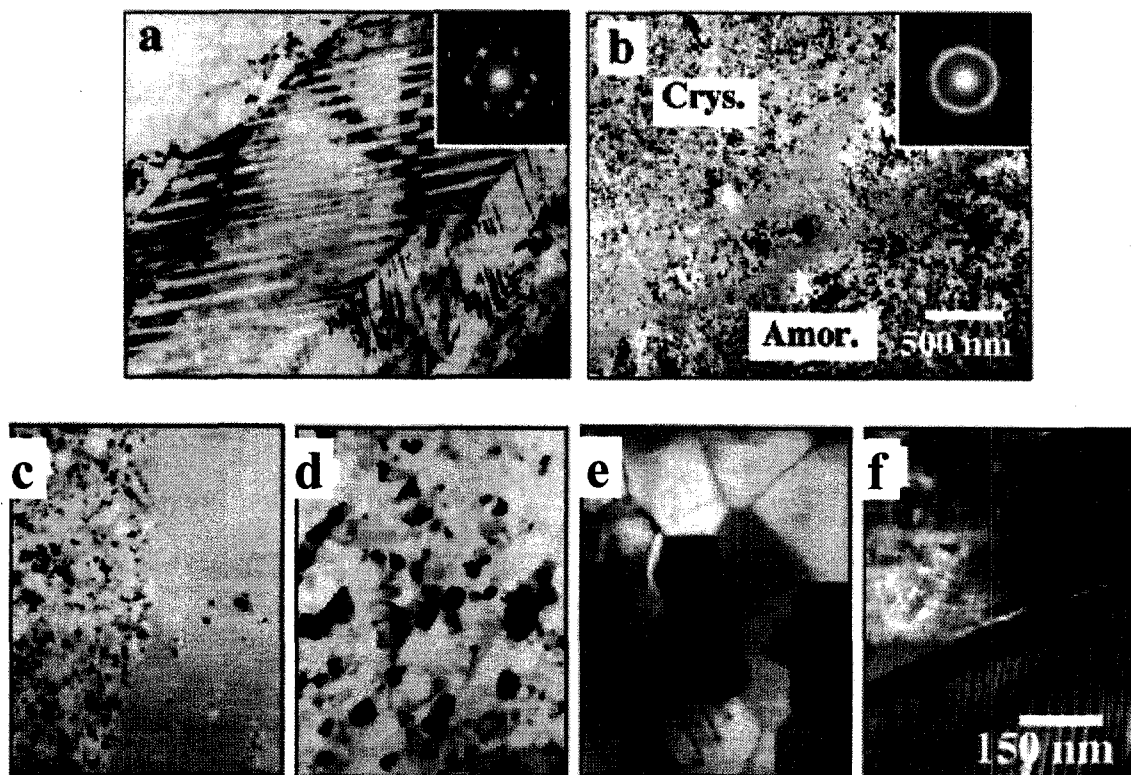


Figure 2. 7. DSC curves for cold rolled Ti<sub>50</sub>Ni<sub>50</sub> alloy annealed at 500 °C for 3 h. (a) original specimen with 1.2 mm thickness, (b) the ground specimen to 0.4 mm thickness [64].



**Figure 2. 8.** TEM images of (a) homogenised, (b) 70% rolled; rolled and annealed at (c) 573 K, (d) 673 K, (e) 773 K and (f) 873 K for 1 h. Insets are corresponding SAD [67].

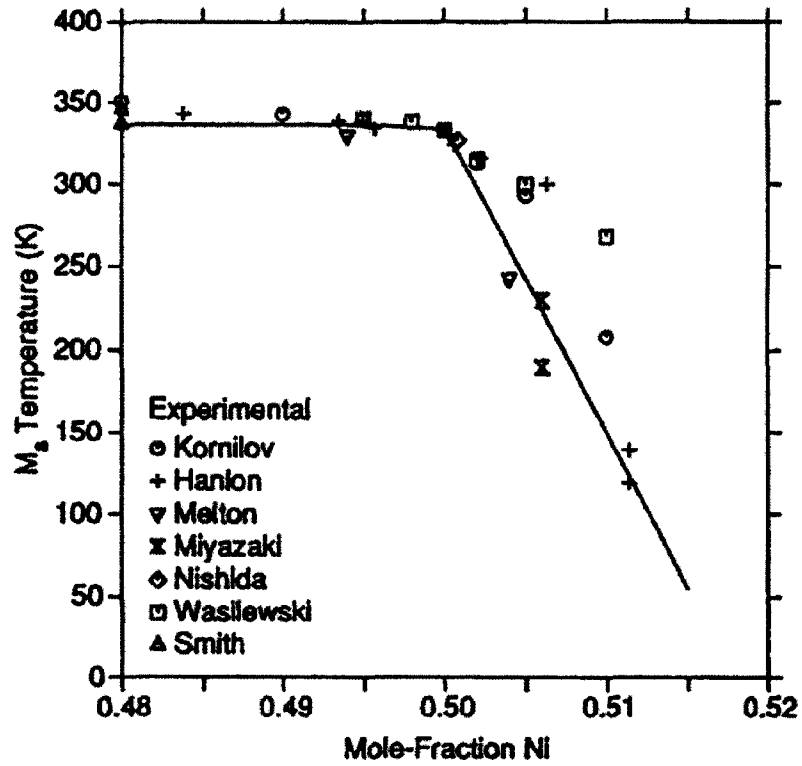


Figure 2. 9.  $M_s$  temperature as a function of Ni content for binary TiNi alloys. Different data symbol represents data from different authors and the solid line is given by thermodynamic calculations [37].

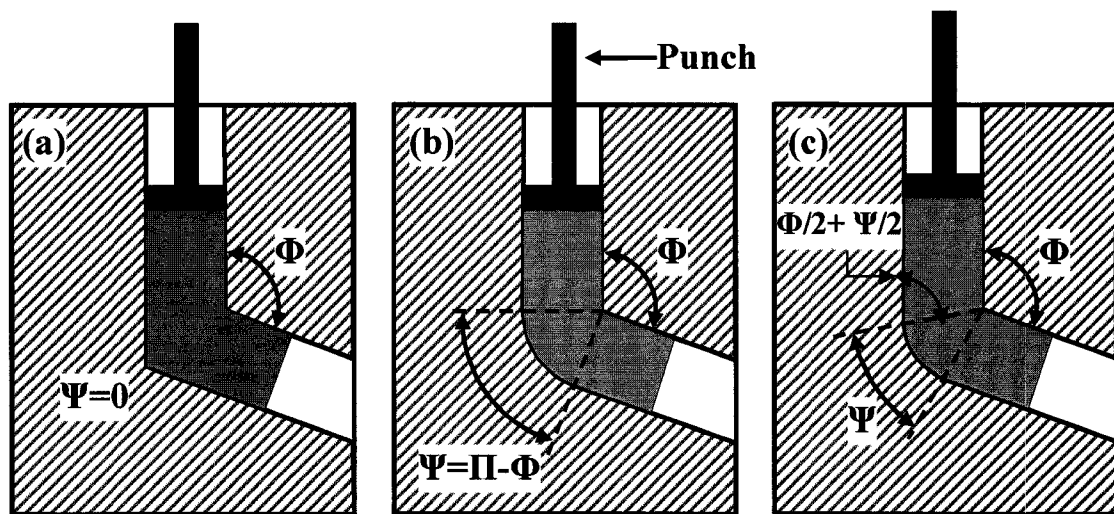


Figure 2. 10. The different possibilities of die design. (a)  $\Psi = 0$ , (b)  $\Psi = \pi - \Phi$  represents two limiting condition and (c) represents an intermediate situation where the strain can be varied for any given channel angle,  $\Phi$ , [84].

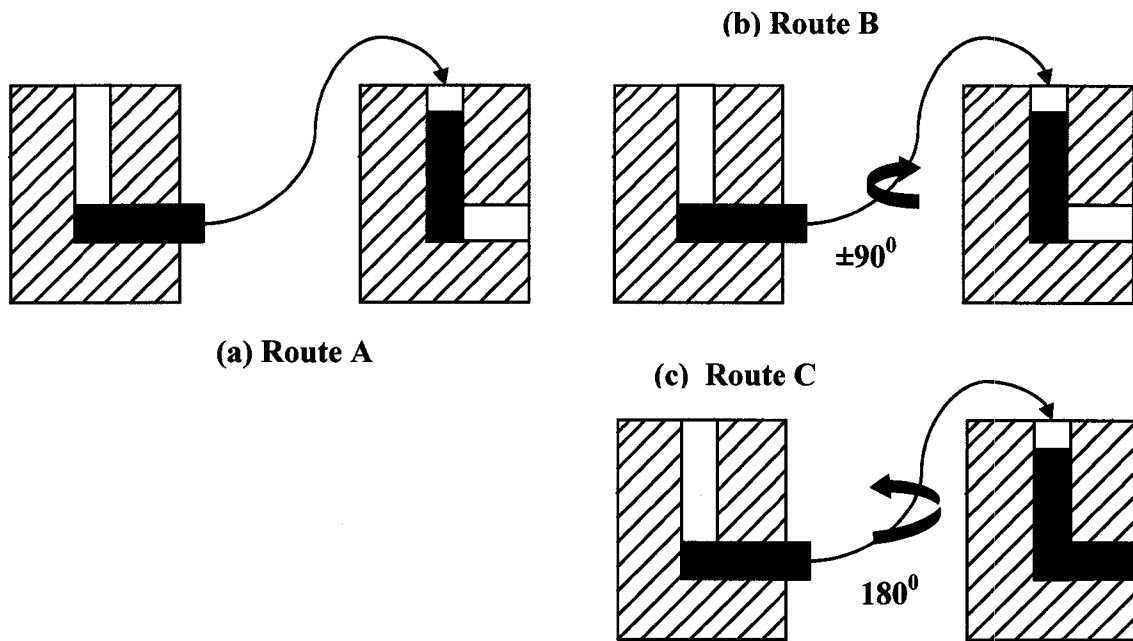


Figure 2. 11. Different processing routes for any given die design; (a) No rotation of sample, (b) rotation of sample either by  $\pm 90^\circ$  alternatively or  $+ 90^\circ$  alternatively, and (c) rotation by  $180^\circ$  [86].

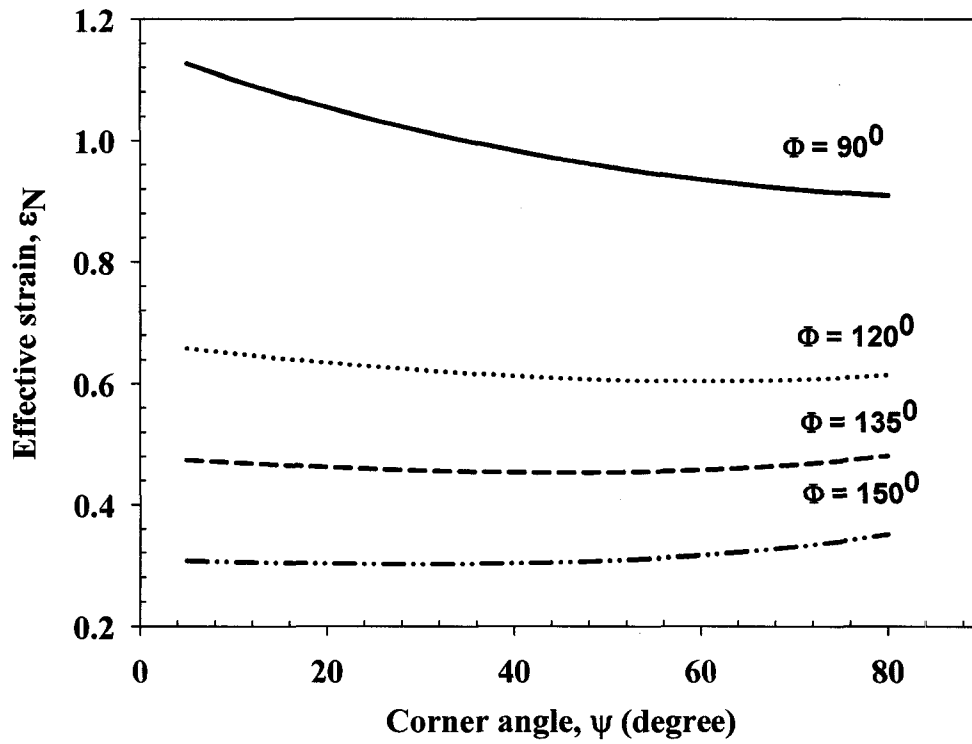


Figure 2. 12. Effective strain variation of with corner angle,  $\Psi$  for four different channel angle,  $\Phi$ .

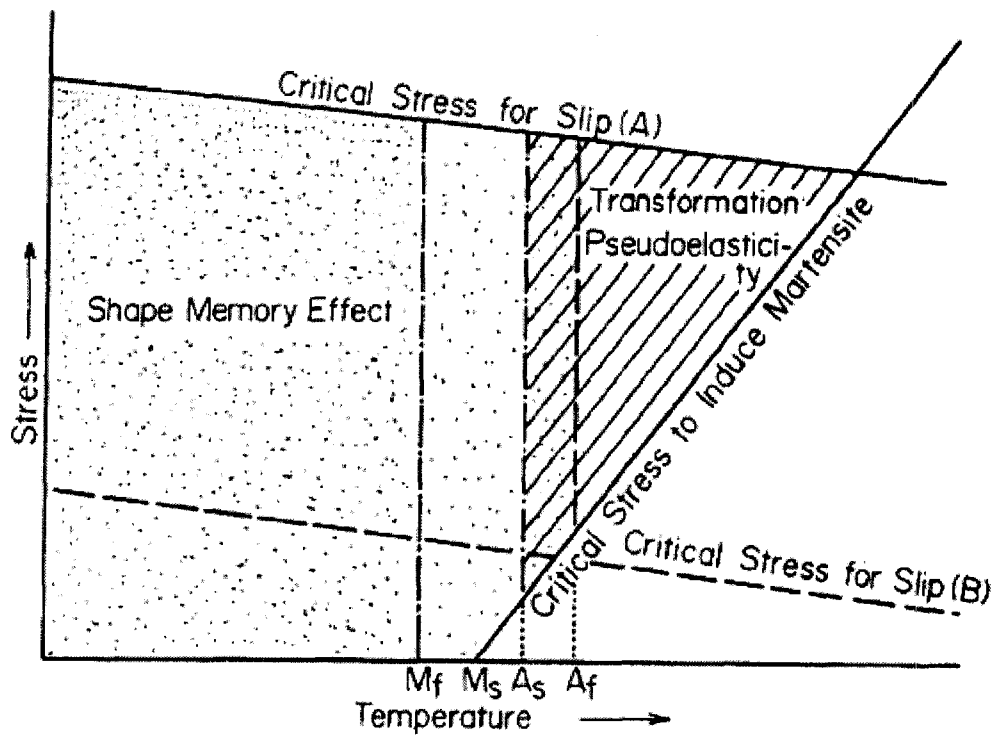


Figure 2. 13. Schematic diagram representing region of shape memory effect and transformation pseudoelasticity in temperature-stress coordinates [99].

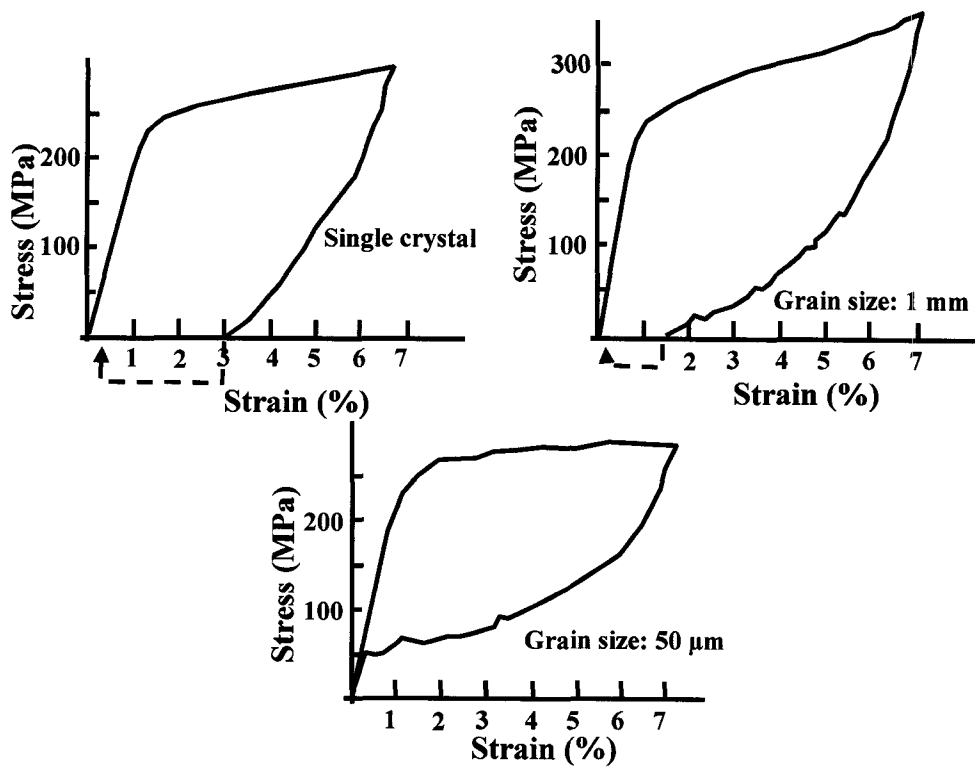


Figure 2. 14. Stress-strain curves obtained from uniaxial testing showing the effect of grain size on pseudoelasticity of Ti 50.5at.% Ni alloy [100].



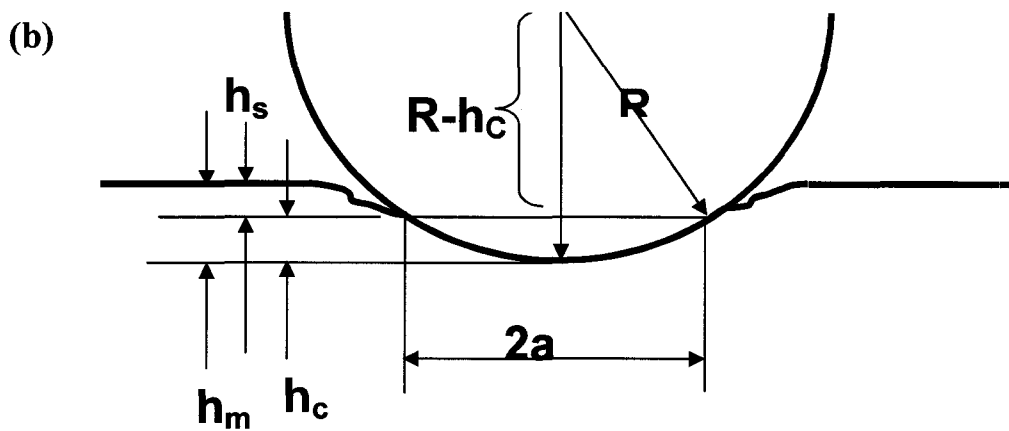
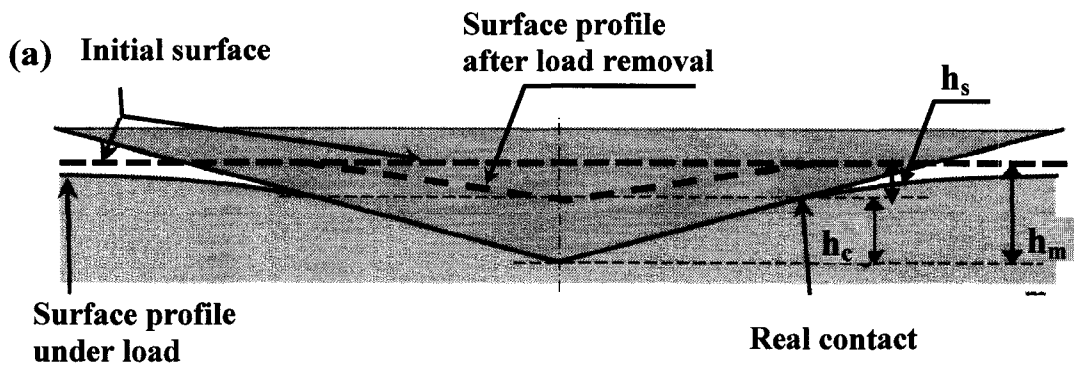


Figure 2. 15. Schematic cross-section of (a) sharp indentation (b) spherical indentation under load.

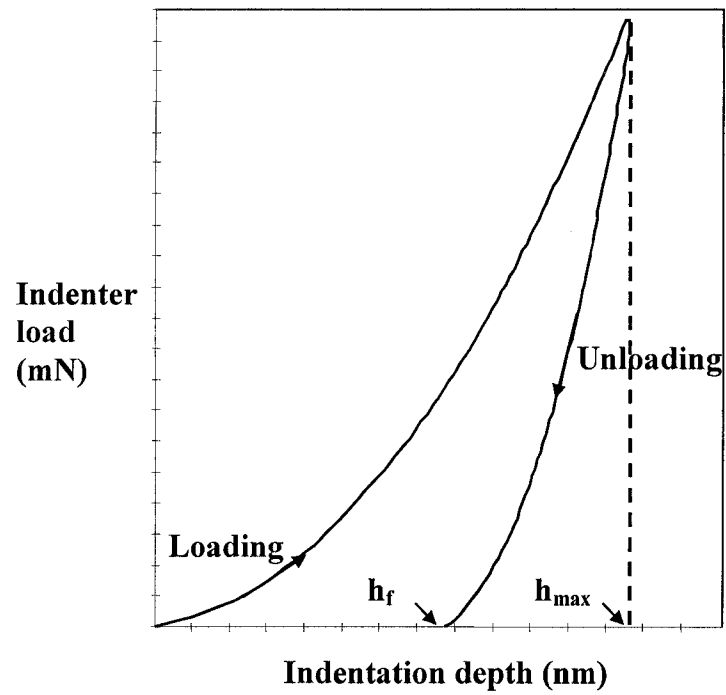


Figure 2.16. Typical load displacement curve in instrumented indentation experiments and definition of various parameters measured.

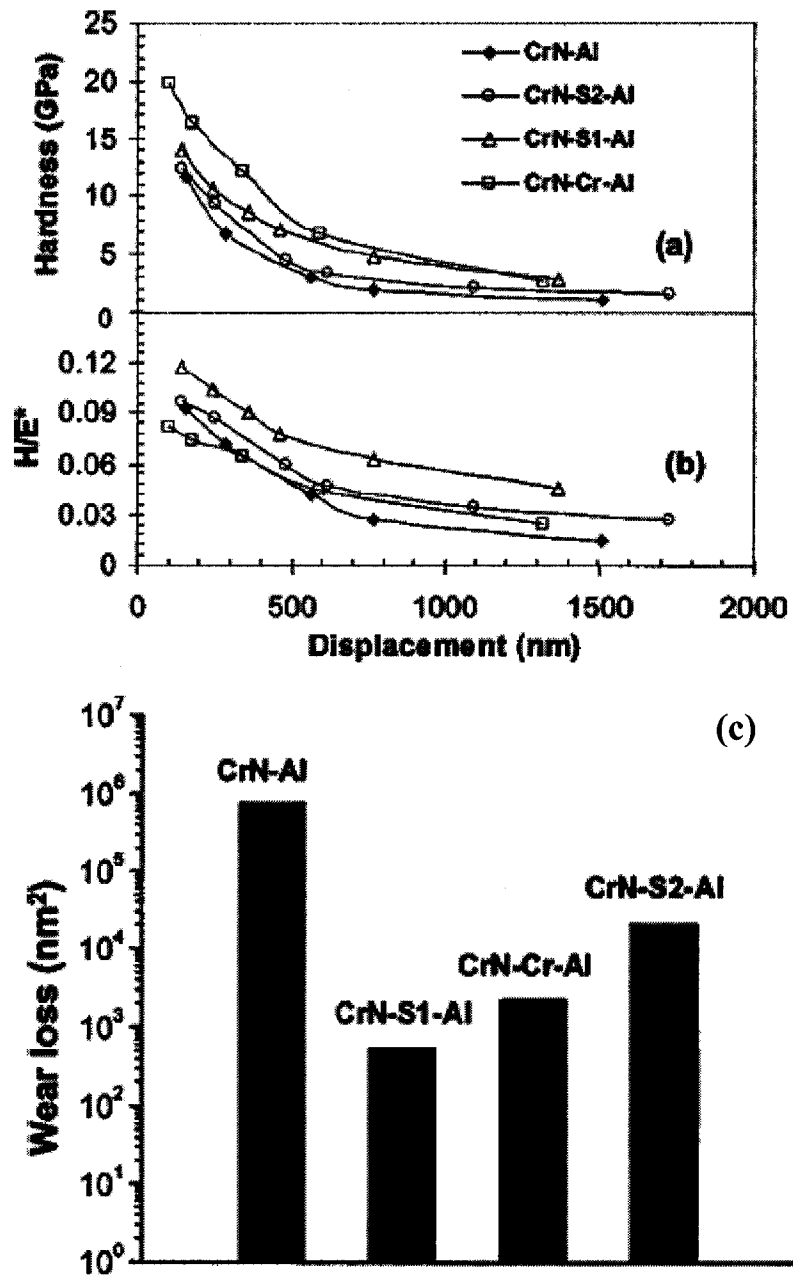


Figure 2. 17. (a) Hardness; (b)  $H/E^*$  ratio; and (c) wear loss of various specimens. The Y-axis in (c) is in logarithmic scale [114].

## CHAPTER 3

### 3. Experimental Methods

#### 3.1. Composition and As-Received condition of TiNi alloy

The alloy used in this study was a pseudoelastic grade Ni rich binary TiNi alloy. The alloy composition in weight percentage is given in Table 3.1. Upon converting the weight percentage to atomic percentage, the alloy composition becomes 44.12 at.% Ti 50.8at.% Ni and designated here after as Ti 50.8at.% Ni. The alloy was procured from Special Metals, New Hartford, NY. The as-received alloys were in the plate form with 10 mm thickness and 200 mm in length and width. They were hot rolled, flattened, and finally grit blasted. The transformation temperatures of as received material in fully annealed condition (as quoted by the supplier) are  $M_S$ :  $-22\text{ }^{\circ}\text{C}$ ,  $M_f$ :  $-37\text{ }^{\circ}\text{C}$ ,  $A_S$ :  $-13\text{ }^{\circ}\text{C}$  and  $A_f$  :  $+3\text{ }^{\circ}\text{C}$ . The transformation temperatures were confirmed using differential scanning calorimetric (DSC) measurement and shown in **Figure 3.1**. The details of DSC measurement will be provided in section 3.3. There is a slight variation in the transformation temperatures to that of fully annealed condition as obtained from the manufacture. The microstructure of the as-received alloy was observed and the microstructure reveals elongated grains up to 200  $\mu\text{m}$ . The details of metallographic specimen preparation are given in the following section.

**Table 1. Composition of as received TiNi alloy**

Element	Nickel	Titanium	Oxygen	Carbon	Hydrogen	Boron	Other elements
wt.%	55.85	44.12	<0.05	<0.05	<0.005	<0.001	<0.01
at.%	50.796	49.203	<0.0004	<0.0005	<0.002	<0.00001	-

### **3.1.1. Metallographic Specimen Preparation for Optical Microscopy**

For optical microscopy of various samples, low speed diamond saw was used to cut the sample. Then, the cut samples were mounted using cold setting resin and the samples are rough ground using Buehler make silicon carbide abrasive paper starting from 240 grit size to 1200 grit size. Each time care is taken that the scratches from previous grinding paper are completely removed. After the grinding is over, the samples were polished using diamond paste of 6  $\mu\text{m}$ , 3  $\mu\text{m}$ , 1  $\mu\text{m}$  and finally with 0.5  $\mu\text{m}$ . Finally, after polishing the samples were etched using a mixture of nitric acid ( $\text{HNO}_3$ ), hydrofluoric acid (HF) and water ( $\text{H}_2\text{O}$ ) in a proportion of 2.5:1:5 in volume.

### **3.2. Preparation of Bulk Nanocrystalline Structure**

To produce the bulk nanocrystalline structure, two deformation techniques namely cold rolling and equal channel angular pressing (ECAP) were employed. The samples cut from the original plates were in the form of slab of dimension 40 mm $\times$ 6 mm $\times$ 10 mm.

#### **3.2.1. Cold Rolling of Ti 50.8at.% Ni**

Two sets of cold rolling experiments were performed. First, the cold rolling was carried out on the as received alloy with 30 % thickness reduction. In the second sets of rolling experiments, the as-received samples were first solution treated at 900  $^{\circ}\text{C}$  for 0.5 h and then quenched in water. During this process, the samples were encapsulated in quartz tube under vacuum so that no oxidation takes place during the treatment. This solution treatment was done to eliminate any pre-strain in the samples. The transformation temperature after the solution treatment was measured again using DSC. The details of DSC measurements are elaborated in a separate section (See section 3.3). Then the samples were cold rolled to give a thickness reduction of 10%, 20%, 50% and 80%. For 50% and 80%

rolled samples an intermediate annealing at 600 °C for 15 min was done after 30 % and 60% thickness reductions, respectively. During annealing, the samples were packed with dry alumina powder to minimise the oxidation and after annealing the samples were again ground using 240 grit silicon carbide papers. This annealing was done to facilitate rolling without cracking the samples. For all rolling experiments, the thickness reduction was achieved in multiple steps with about 5% thickness reduction in each step.

Hereafter, the rolled samples will be named with a number representing the percentage reduction it has undergone during cold working followed by letters “CW” representing cold working. After cold rolling the microstructure of all the samples were observed using an optical microscope. The samples were prepared as described earlier in the section 3.1.1.

### **3.2.2. Equal Channel Angular Pressing (ECAP) of Ti 50.8at.% Ni**

Equal channel angular pressing of Ti 50.8at.% Ni was carried out using cylindrical samples. The as received slab samples were machined to 6.35 mm diameter (1/4" inch) using wire-electro discharge machining (wire-EDM). Then the samples were cut to 40 mm long. These samples were vacuum encapsulated in quartz tube and solution treated at 900 °C for 0.5 h. The samples were again ground using 240 grit silicon carbide paper and cut into two halves of 20 mm in length prior to ECAP.

The ECAP die was designed to have a channel angle,  $\Phi$  of 120° and corner angle,  $\Psi$  of 20° (for definition of  $\Phi$  and  $\Psi$  refer **Figure 2.10** in section 2.3.1). This die produces an equivalent strain,  $\epsilon_{eq}$ , of 0.635 during each pass. **Figure 3.2** gives the schematic of the ECAP die assembly. All components of the assembly except the sample and the plunger was made out of AISI H13 steel and was hardened to give a hardness of 54±2 HRC. The die was made

out of two halves each being the mirror image of the other. The inside surface of the die was ground to have a better surface roughness and make an exact circular channel. A disk shape carbide insert was press fitted inside the plunger guide to prevent the plunger being pushed into the plunger guide during pressing. The channel was milled using a carbide reamer before the heat treatment and a finishing cut was given with the carbide reamer to maintain a tolerance of +0.001 inch (0.0254 mm) between the channel surface and the plunger surface.

The plunger was made out of a mixture of cobalt (10% by weight) and tungsten carbide (90% by weight). The carbide plunger was locally procured from KBC Tools & Machinery, Inc. Windsor, Canada. The plungers were 5 inches (127 mm) in length and 0.25 inch (6.35 mm) in diameter. All ECAP experiments were performed by keeping the die at a temperature of 450 °C. A rectangular shaped ceramic heater of 100 mm×79.89 mm×76.2 mm dimensions from Omega Heater Company, NY was used to heat the die. **Figure 3.3** shows an actual photograph of the die assembly with the heater mounted around the die. The pressing was done using a 150 ton capacity hydraulic press from Tinius Olsen, Willow Grove, PA, USA, located at University of Windsor. The die was heated keeping on the base of the press and the temperature was measured using a thermocouple inserted at the exit channel of the die. Thin ceramic cloth type insulation was used in between the die and the base of the press. Just before the pressing, the thermocouple was removed from the channel and the surface temperature was measured during the pressing. The sample was heated keeping it inside the channel for 5 min. An approximately constant ram speed during the pressing was maintained manually.

The samples were subjected to a total four number of passes and the samples after first, second, third and fourth ECAP passes will be called as 1st ECAP, 2nd ECAP, 3rd

ECAP and 4th ECAP, respectively. The equivalent strain applied after first, second, third and fourth ECAP passes will be 0.635, 1.27, 1.905 and 2.54, respectively.

### **3.3. Differential Scanning Calorimetric (DSC) Measurements**

The transformation temperature of as-received (AR), solutionised and quenched sample (ARS), 10CW, 20CW, 30CW, 50CW and 80CW samples were measured using differential scanning calorimeter. DSC Q2000 V23.5 Build 72 from TA Instruments located at GM R&D centre, Warren, Michigan, was used for the measurements. The calorimetric measurement was done between  $-90^{\circ}\text{C}$  and  $100^{\circ}\text{C}$  and all the measurement was started after bringing the sample temperature to  $-90^{\circ}\text{C}$  at a heating and cooling rate of  $5^{\circ}\text{C}/\text{min}$ . During heating and cooling, the temperature was modulated by  $\pm 0.5^{\circ}\text{C}$  in every 60 seconds. The sample weights were between 10 to 20 mg, which was cut using low speed diamond saw. Commercial paint thinner (Varsol) was used as a coolant during cutting to avoid any thermal effects.

### **3.4. X-Ray Diffraction Measurement of Cold Rolled and ECAP Samples**

After cold rolling, the alloys did not show any transformation peaks in DSC measurements. To find out the phases present after cold rolling, the samples were subjected to X-Ray diffraction analysis using a Rigaku DMAX-1200X-Ray diffractometer located at University of Windsor. The diffraction peaks related to various phases present were observed using Cu K- $\alpha$  radiation. The samples after ECAP was also subjected to X-ray diffraction study to complement the DSC findings.



### **3.5. Indentation Experiments**

Both micro- and nanoindentation experiments were performed on cold rolled and ECAP samples. All the samples were ground using silicon carbide abrasive papers starting from 240 grit to 1200 grit size and then finally polished using 6, 3, 1 and 0.1-micron diamond paste before indentation to give an average roughness of less than 100 nm. Micro indentation experiments were conducted on CSEM micro scratch tester with indentation capability located at GM R&D centre, Warren, Michigan and nanoindentation experiments were conducted on nanoindenter XP from MTS located at GM R&D centre, Warren, Michigan.

#### **3.5.1. Conical Indentation of Cold Rolled Samples**

The as received sample after solutionisation (ARS), 10CW, 20CW, 50CW and 80CW samples were subjected to spherical indentation to calculate the pseudoelastic recovery. The indentation was performed using a conical indenter with a spherical tip of 107  $\mu\text{m}$  radius. This type of indenter produces spherical indentation for low loads. A progressive type of loading cycle was used wherein a number of indentation cycles are performed in one place with a progressive loading. A typical loading cycle is shown in the **Figure 3.4**. During the indentation, initial and the final loading were 500 mN and 2500 mN with a progressive increase of 500 mN resulting five indentation cycles.

#### **3.5.2. Berkovich Indentation of Cold Rolled Samples**

Berkovich indentation was also carried out for as received sample, cold rolled samples to find out the recovery ratio, Young's modulus and hardness of the samples. After 80% cold rolling reduction, the sample was aged to 450  $^{\circ}\text{C}$  to study the effect of ageing on the transformation temperature and shape memory and pseudoelastic behaviour. This sample

was also subjected to the micro-indentation. Both, constant multi-cycle (CMC) and progressive multi-cycle (PMC) indentations were conducted. CMC indentations were conducted at 500 mN and 2500 mN and for the PMC indentations, similar loading-unloading cycles to that of spherical indentations were used. For all the micro indentation using Berkovich tip, loading and unloading rates were 1000 mN/min and 10000 mN/min. This fast unloading was used to avoid the nose formation at the start of the unloading cycle of load-displacement curve. In addition, a pause of 5 s was given at the maximum load to avoid nose formation. For each sample and each type of loading three different indentations were performed. The hardness, Young's modulus and the depth recovery ratio was calculated from the load displacement curve. The Poisson's ratio and Young's modulus of diamond indenter was taken to be 0.07 [23] and 1141 GPa [23] and the Poisson's ratio of Ti 50.8at.% Ni samples was takes to be 0.3 [21].

### **3.5.3. Indentation of ECAP Samples**

After ECAP, the samples were cut in longitudinal and cross-sectional directions, mounted using cold setting resin, ground and polished with 0.1  $\mu\text{m}$  diamond paste. Nanoindentation using a sharp Berkovich tip was carried out on 1st ECAP, 2nd ECAP, 3rd ECAP and 4th ECAP samples. A loading cycle with 100 mN maximum load was used for the nanoindentations. The hardness, Young's modulus and the recovery ratio was calculated from the load displacement curves.

To find out the indentation induced shape memory ability of Ti 50.8at.% Ni alloy after ECAP, spherical indentation using a sphero-conical diamond indenter of 200  $\mu\text{m}$  tip radius was used. Indents were made using 0.5 N, 1 N, 5 N, 10 N and 20 N load and single indentation cycle. The 3-D profiles of the indents were then measured using WYKO HD

3300 optical surface profilometer located at GM R& D centre, Warren, Michigan. During the profilometer measurement, vertical scanning interferometry (VSI) mode was adopted. From these measurements the residual indent depth before heating ( $h_{max}^{BH}$ ) was measured. After measuring the indents, each sample was heated to a temperature of 75 °C using electrical heater and the same indents were observed using WYKO optical profilometer to measure the residual indent depth after heating ( $h_{max}^{AH}$ ). Finally, indentation induced shape memory recovery ratio ( $\eta_{SME}^h$ ) was calculated. The temperature of the sample was monitored using thermocouple during the heating and once the temperature of the samples were stabilised within  $\pm 3$  °C profilometer measurements were taken.

To find out the indentation induced pseudoelasticity of Ti 50.8at.% Ni alloy after ECAP, indentation was done again using the same sphero-conical indenter with 200  $\mu\text{m}$  tip radius at 5 N, 10 N and 20 N load. However, the indentations were carried out at an elevated temperature of 75 °C where the microstructure of the samples was completely austenitic. The indentation was carried out using the same scratch tester located at GM R& D centre, Warren, Michigan. The indents were imaged again using the WYKO optical profilometer at 75 °C. The sample temperature was monitored during the indentation and WYKO measurement. The measurements were done once the temperature is stabilised within  $\pm 3$  °C. **Figure 3.5** shows the actual photograph of heating arrangement of the samples during indentation and profilometer measurement. Finally, the pseudoelastic depth recovery ratios ( $\eta_{PE}^h$ ) were calculated from the load displacement curves.

### **3.6. Scratch Experiments**

To study the recovery behaviour during tangential loading, which typically exists in the macro-scale wear experiments, the cold rolled and ECAP processed Ti 50.8 at.% Ni alloy samples were subjected to scratch loading conditions. The scratches were generated on the mechanically polished surface using two different types of indenters in CSEM micro scratch tester located at GM R&D centre, Warren, Michigan. The pseudoelastic behaviour of cold rolled sample and ECAP processed sample were studied.

#### **3.6.1. Scratch Testing of Cold Rolled Samples**

Scratch tests were carried out on 10CW, 20CW, 50CW and 80CW samples and the maximum scratch depth during loading and recovery depths after unloading were compared to that of ARS sample. Again, all the samples were mechanically polished using 0.25  $\mu\text{m}$  diamond paste to generate a surface roughness less than 100 nm. A rounded conical diamond tip of 269  $\mu\text{m}$  radius was used to make the scratches using a progressive type of loading starting at 0.1 N up to a maximum of 10 N. The scratch length was of 2 mm and a scratch speed of 2 mm/minute was used. On each sample totally 6 scratches were made and the maximum scratch depth ( $P_d$ ) during loading was recorded from the scratch tester. After the load removal, the scratches exhibit self-healing property due to pseudoelasticity induced back transformation. The scratches were observed under WYKO optical profilometer to measure the residual scratch depth at no load. The pseudoelastic recovery was calculated at a point corresponding to the maximum load (at the end of the scratch) applied during the scratch.

### 3.6.2. Scratch Testing of ECAP Samples

After each pass of ECAP, the samples were again cut in their longitudinal direction, mechanically polished to generate a surface roughness less than 100 nm. The samples were then glued to a flat aluminum sheet and OMEGA<sup>®</sup> CC high temperature cement was applied around the sample to place the sample firmly under load. Scratches were made using the same sphere-conical indenter with 200  $\mu\text{m}$  tip radius. Again, progressive mode was used with load starting from 0.1 N to 10 N. The scratch length was 1 mm and the speed was 1 mm/min. The scratches were made at a temperature of 75  $^{\circ}\text{C}$  using the same heating arrangement as shown in **Figure 3.5**. The residual scratch depth at no load was measured using WYKO optical profilometer at the same temperature the scratches were made. Finally, the pseudoelastic recovery was calculated at a point corresponding to the maximum load (at the end of the scratch) applied during the scratch.

### 3.7. Spherical Indentation of Cold Rolled Samples

Spherical indentation with progressive multi-cycle (PMC) indentation was carried out on ARS sample, 10CW sample and 80CW sample. The purpose of the spherical indentation was to generate an indentation induced stress-strain curve for the alloy having three different microstructures. As the strain under a spherical indenter varies with contact depth depending on the load, during PMC the load was varied from a very low load of 100 mN to a very high load of 20 N. The measured hardness indicates the stress applied during indentation. The indenter used was the same sphero-conical indenter with 200  $\mu\text{m}$  tip radius and the indentations were carried out at room temperature (23  $^{\circ}\text{C}$ ). Two sets of PMC indentations were carried out on each sample and the results from both experiments were plotted together. In the first set of PMC indentations loads were incremented by 100 mN in each successive

cycle starting from 100 mN to 1000 mN and for the last two cycles the load was 1.5 N and 2.0 N. Complete unloading was done during each cycle. In the second sets of indentation, the loads used were 1 N, 2.5 N, 5 N, 10 N, 15 N, and 20 N and unloading during each cycle was done up to 50% of the maximum load in the corresponding cycle.

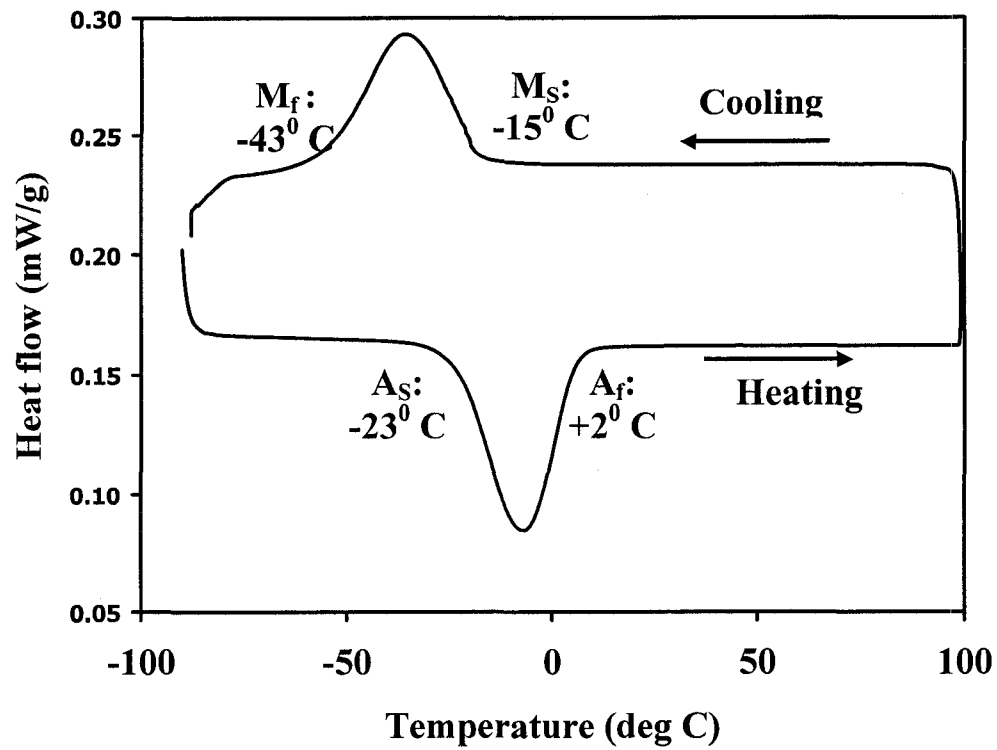
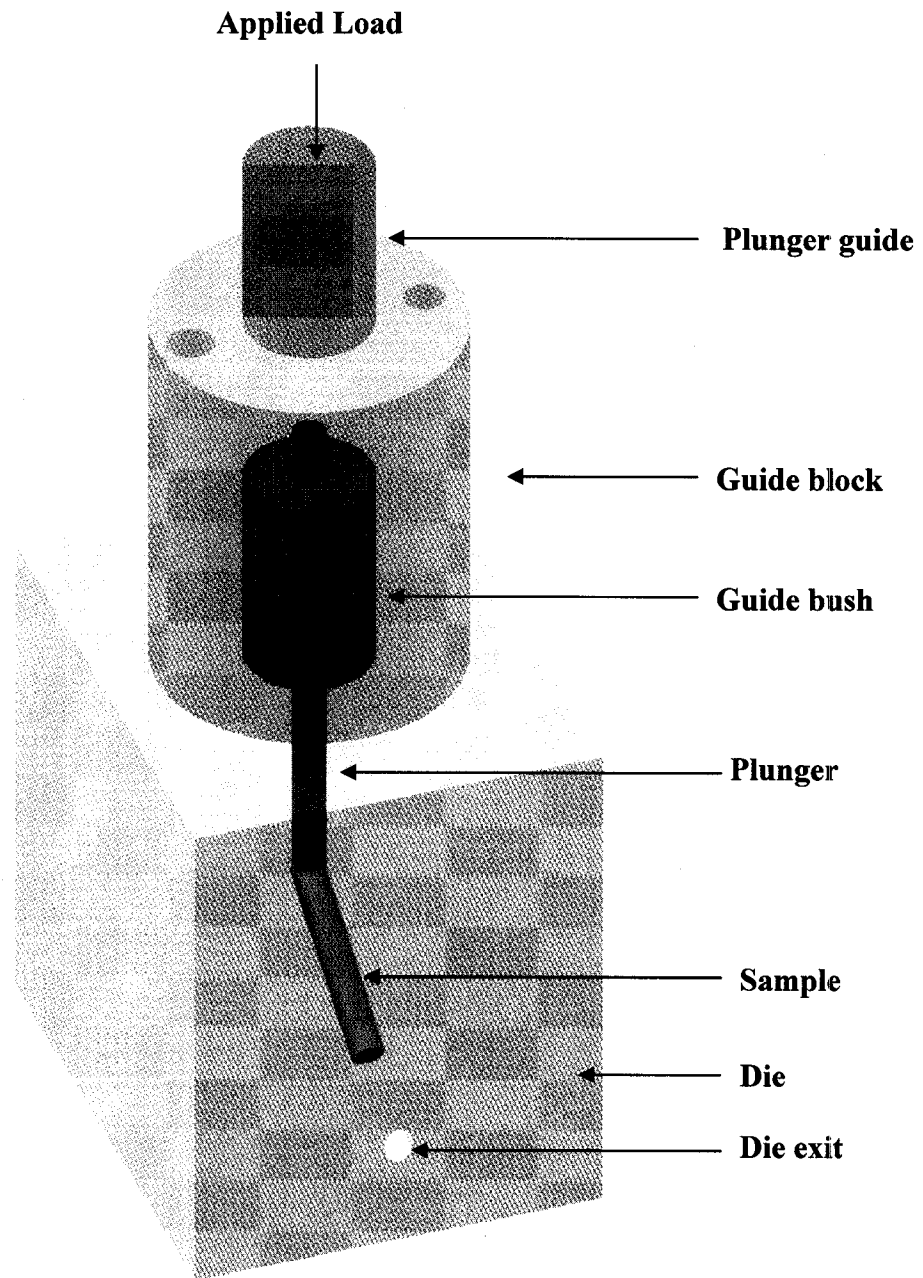
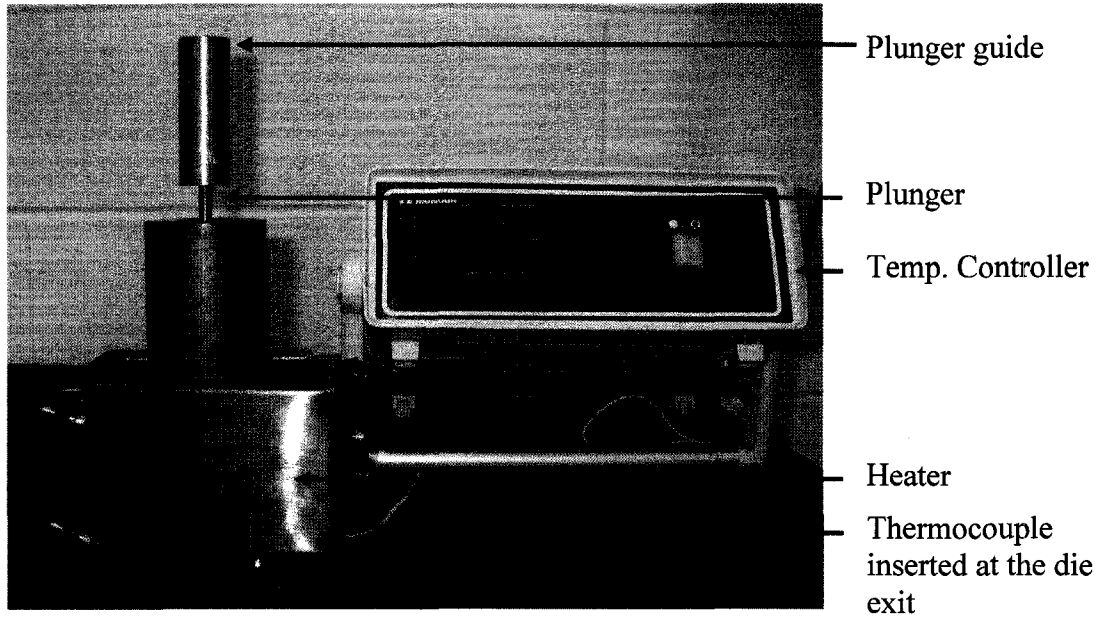


Figure 3. 1. DSC profile showing the transformation behaviour of as-received Ti 50.8at.% Ni alloy with a heating and cooling rate of 5°C/min



**Figure 3. 2. A schematic of the ECAP die assembly showing various parts.**





**Figure 3. 3. An actual photograph of the die and heating arrangement for ECAP. The die is at room temperature in the photograph**

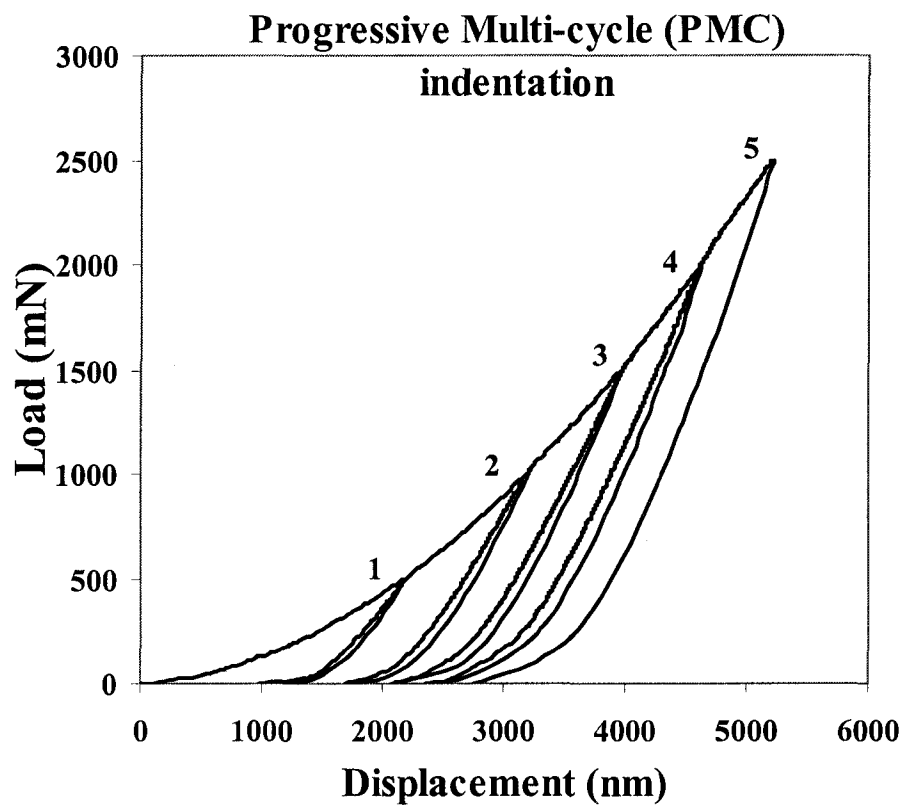


**Figure 3.4. A typical progressive multi-cycle (PMC) loading-unloading cycle during instrumented indentation**

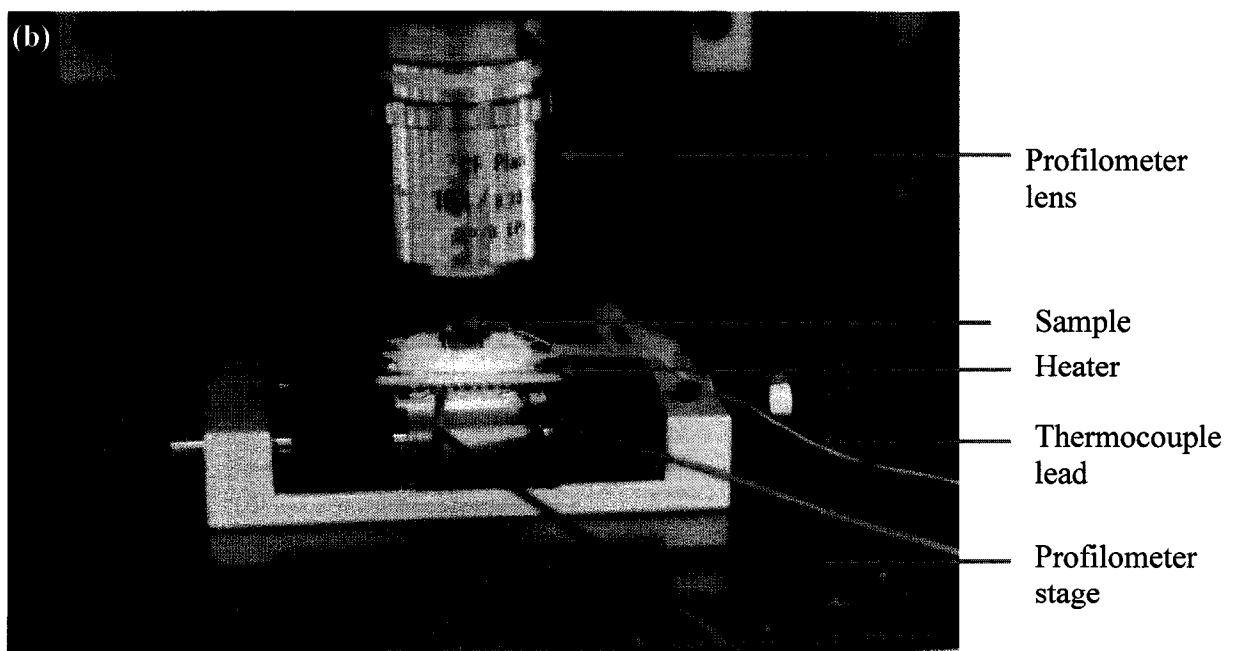
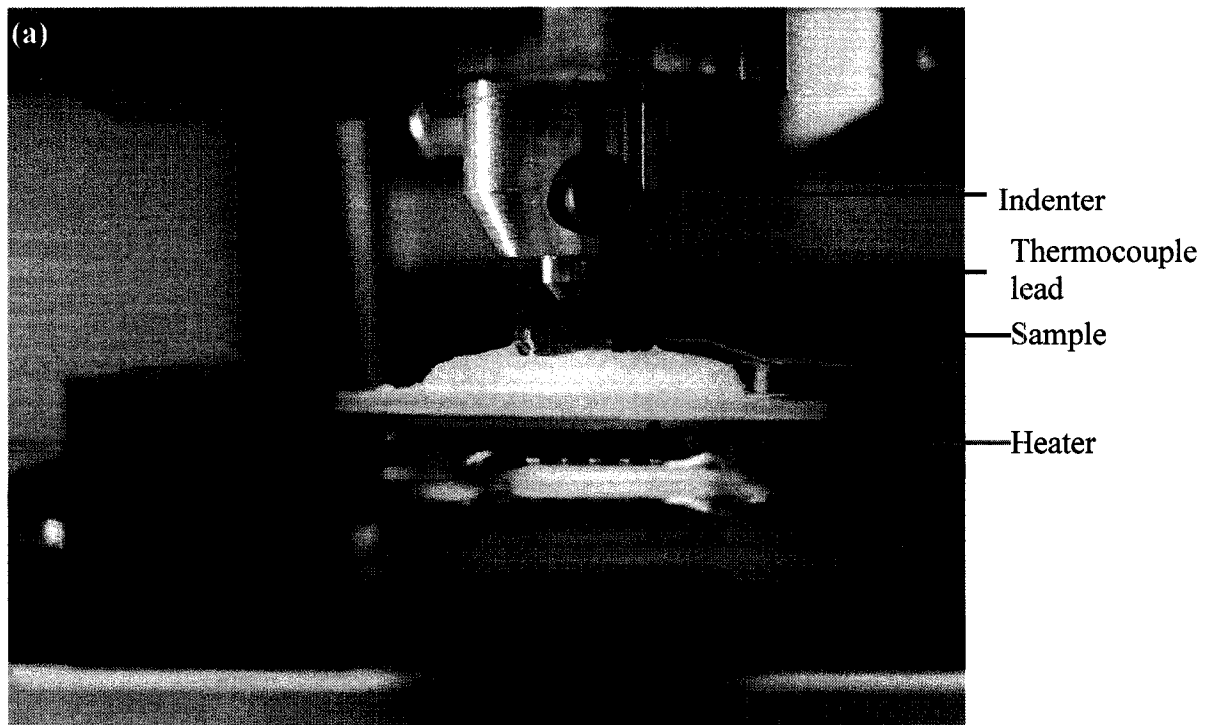


**Figure 3.5. Actual photograph of the heating arrangements during (a) indentation and (b) profilometer measurement**

## CHAPTER 4

### 4. Results

#### 4.1. Optical Microscopy of Cold Rolled Samples

**Figure 4.1** shows the optical microstructures of Ti 50.8at.% Ni alloys in as-received condition which was hot rolled and grit blasted, after solution treatment (ARS) at 900 °C for 0.5 h followed by quenching and after various amount of cold rolling reduction in thickness. The optical microstructure does not reveal much information in TiNi alloys especially when they are deformed plastically. In **Figure 4.1(a)** and **4.1(b)**, the alloy in as-received condition and after solution treatment reveals grain boundaries fairly well. The grain size in as-received alloy varies from about 10 – 80 µm and the same in ARS alloy is 50-60 µm. It is quite clear from the optical microstructure that a more homogenised structure is present in the ARS sample when compared to the as-received sample. After cold rolling, the microstructure evolution was different; the 10CW and 20CW samples reveal plate-like or lenticular morphology, which is an indication of partially transformed structure. **Figure 4.1(c)** and **(d)** shows twins of lenticular morphology, which resembles to a martensitic structure in between austenite grains. However, when the thickness reduction during cold rolling increases to 50% and 80%, heavily deformed banded structure is observed as shown in **Figure 4.1(e)** and **(f)**. The grain sizes could not be measured from the optical micrograph in these two samples as the grain boundaries are not visible.

#### 4.2. Differential Scanning Calorimeter

**Figure 4.2(a)** shows the transformation profile of as-received Ti 50.8 at.% Ni sample recorded using DSC. The as-received alloy shows a single step transformation from  $B2 \rightarrow B19'$  and  $B19' \rightarrow B2$  upon cooling and heating, respectively. The structure in the as-

received condition is austenitic at room temperature (23 °C). After solution treatment followed by quenching the DSC profile for the alloy is recorded again using DSC and is shown in **Figure 4.2(b)**. The transformation path is single-step similar to that of as-received sample with slight variation in transformation temperatures. The transformation temperatures of both as-received and ARS sample are listed in Table 4. 1.

**Table 4. 1. Transformation temperatures of as-received TiNi alloy and after solutionisation followed by quenching (ARS)**

Sample	Transformation temperatures ( °C)			
	A <sub>s</sub>	A <sub>f</sub>	M <sub>s</sub>	M <sub>f</sub>
As-received	-23	+2	-15	-43
ARS	-23	+6	-19	-50

#### 4.2.1. DSC of Cold Rolled Samples

After cold rolling to give various thickness reductions, the DSC profile of various samples were measured and are shown in **Figure 4.3**. The cold rolling in general decreases the martensitic transformation temperatures. As it is seen from **Figure 4.3**, the thickness reduction beyond 30% suppresses the forward and reverse transformations. This indicates that the microstructures for 50CW and 80CW samples are austenitic at room temperature.

#### 4.2.2. Differential Scanning Calorimetry of ECAP Samples

The DSC profiles of Ti 50.8at.% Ni alloy after various passes of ECAP at 450 °C are also recorded using DSC and are shown in **Figure 4.4**. After ECAP, the transformation path and the transformation temperatures are markedly different from that of ARS and rolled samples. After first pass of ECAP, the martensitic transformation temperatures are increased substantially and the alloy becomes martensitic at room temperature. After subsequent passes

in ECAP, the transformation temperatures are not increased much and remained almost constant. In addition, the transformation path changes from single-step transformation to two-stage transformation  $B19' \rightarrow R \rightarrow B2$  during heating and a single-step transformation  $B2 \rightarrow B19'$  during cooling in DSC. Also, in 2nd ECAP sample, a multi-stage transformation behaviour is seen during heating in DSC chamber. However, the cooling cycle was no different from that of other ECAP samples. The transformation temperatures of various ECAP samples are plotted against the equivalent strain applied during ECAP in **Figure 4.5**. The increase in martensitic transformation temperatures can be observed more clearly in this figure. In addition, the R phase transformation temperatures are also plotted for ECAP processed samples. The solid horizontal line indicates the room temperature and it can be seen from **Figure 4.5** that the alloys after ECAP processing has a martensitic structure comprising B19' and R phase.

#### 4.2.3. Summary of DSC Results

The DSC results presented in section 4.2.1 and 4.2.2 shows that the martensitic transformation behaviour in Ti 50.8at.% Ni alloy is affected by the plastic strain induced during deformation, temperature of deformation and subsequent treatment. Cold rolling initially stabilise martensite partially in the alloy and beyond 30% rolling, austenite stabilisation is seen and no martensitic transformation is seen even at  $-90^{\circ}\text{C}$ . However, the transformation path remains  $B2 \leftrightarrow B19'$  type similar to ARS sample. ECAP process changes the martensitic transformation behaviour differently from that of cold rolling. After first ECAP pass, the martensitic transformation temperature increases and the transformation paths also becomes a two-step process during heating cycle. After second pass in ECAP a multi-step transformation is seen and again after third and fourth pass a two-step

transformation process is observed. The martensitic transformation process after various processing condition is summarised in Table 4.2 and Table 4.3.

**Table 4.2. Martensitic transformation behaviour of ARS and Cold rolled samples**

<b>Sample name</b>	<b>Processing condition</b>	<b>Room temp. structure<sup>1</sup></b>	<b>Transformation sequence in DSC</b>
ARS	Solutionised at 900 °C and quenched in water	Austenite (B2)	B2 ↔ B19'
10 CW	Cold rolling (CR) to give 10% thickness reduction	B2 + B19'	B2 ↔ B19'
20 CW	CR to give 10% thickness reduction	B2 + B19'	B2 ↔ B19'
50 CW	50% CR with one intermediate annealing at 600 °C for 15 min	B2	No transformation up to -90 °C
80 CW	80% CR with two intermediate annealing at 600 °C for 15 min	B2	No transformation up to -90 °C

**Table 4.3. Martensitic transformation behaviour of ECAP processed samples**

<b>Sample name</b>	<b>Processing condition</b>	<b>Room temp. structure<sup>2</sup></b>	<b>Transformation sequence in DSC</b>
1st ECAP	One pass in ECAP and ageing in the die	B19' + R	B19' → R → B2 during heating and B2 → B19' during cooling
2nd ECAP	Two pass in ECAP and ageing in the die	B19' + R	Two B19' → R peaks and one R → B2 peak during heating and B2 → B19' during cooling
3rd ECAP	Three pass in ECAP and ageing in the die	B19' + R	B19' → R → B2 during heating and B2 → B19' during cooling
4th ECAP	Four pass in ECAP and ageing in the die	B19' + R	B19' → R → B2 during heating and B2 → B19' during cooling

<sup>1,2</sup> This is determined from XRD results. Refer section 4.3 for more details



### 4.3. X-Ray Diffraction Study

#### 4.3.1. X-Ray Diffraction of Cold Rolled Samples

To confirm the results obtained from DSC and to find the phases present after cold rolling, X-ray diffraction study was made for rolled samples. **Figure 4.6** shows the XRD pattern of ARS sample and various cold rolled samples. Individual peaks were identified using Bragg's law in the reciprocal space. In ARS sample, diffraction from  $(110)_{B2}$ ,  $(200)_{B2}$ ,  $(211)_{B2}$  and  $(220)_{B2}$  plane is observed confirming the structure of the alloy being austenitic at room temperature. Upon rolling, with increasing amount of rolling reductions peak broadening of the various diffraction peaks takes place. The 50CW sample shows diffraction corresponding to  $(110)_{B2}$  plane only. However, diffractions from  $(211)_{B2}$  and  $(220)_{B2}$  plane were seen in 80CW sample, in addition to the diffraction from  $(110)_{B2}$  plane.

Form the XRD profiles, typical full-width at half-maximum intensity (FWHM) of  $(110)_{B2}$  peak was measured and plotted against the thickness reduction percentage during cold rolling. **Figure 4.7** shows the broadening effect of  $(110)_{B2}$  peak during cold rolling. This broadening is due to decrease in grain size during cold rolling and will be further discussed in subsequent sections.

#### 4.3.2. X-Ray Diffraction of ECAP Samples

X-ray diffraction study was done after conducting ECAP of Ti 50.8at.% Ni alloys. **Figure 4.8** shows the intensity versus two-theta plot for 1st ECAP, 2nd ECAP, 3rd ECAP and 4th ECAP sample. All the samples showed reflections from  $(002)_{B19'}$ ,  $(111)_{B19'}$ ,  $(121)_{B19'}$ , and  $(\bar{2}12)_{B19'}$  plane of B19' martensite. There were also reflections from  $(121)_R$  and  $(322)_R$  plane of R phase. For ECAP samples also, the peak broadening effect was measured for

(111)<sub>B19'</sub> peak and **Figure 4.9** shows the plot of FWHM against total equivalent strain applied during ECAP. From the peak broadening, it can be inferred that the sample with maximum deformation during ECAP, i.e. the sample after 4th ECAP has the smallest grain size.

#### **4.4. Indentation Experiments**

In this section, the results of the indentation experiments will be introduced. The indentation was carried out using conical indenter with different tip radii so that the pseudoelastic behaviour under different applied strain can be measured.

##### **4.4.1. Hardness and Young's Modulus of Cold Rolled Samples**

Progressive multi-cycle (PMC) indentations with Berkovich indenter were carried out to measure the hardness (H) and Young's modulus (E) of the alloy after cold rolling and then compare the results with that of ARS sample. Oliver-Pharr method was employed to calculate the hardness and Young's modulus of the various samples. **Figure 4.10** (a) and (b) show the measured hardness and Young's modulus values, respectively for various samples against percentage thickness reduction during cold rolling at two different indentation loads.

In addition to hardness and Young's modulus, the DRR was also calculated after the Berkovich indentations. **Figure 4.11** shows the calculated DRR values for ARS and cold rolled samples at different indentation loads. From this figure, it can be observed that the depth recovery ratio in case of Berkovich indentation is much lower than the conical indentation, which produces spherical indents. The results of such indentation are presented in section 4.4.4. However, 80CW sample shows the highest recovery even at higher loads. The reason for such lower degree of pseudoelasticity in case of Berkovich indentations will be discussed later in section 5.4.

#### 4.4.2. Spherical PMC Indentation on Cold Rolled Samples

After the indentations were carried out, the representative strain under the indenter during each cycle was calculated using the following equation first proposed by Johnson [115]:

$$\varepsilon_r = 0.2 \frac{a}{R} \quad (4.1)$$

Where  $a$  is the contact radius calculated using Oliver and Pharr method [23,24] and  $R$  is the indenter radius.

The calculated hardness values were plotted against the representative strain for ARS, 10CW and 80CW sample and are shown in **Figure 4.12**. Hardness and representative strains were calculated from the two different sets of PMC indentation experiments as described in section 3.7 and then plotted together.

#### 4.4.3. Hardness and Young's Modulus of ECAP Processed Samples

After ECAP, nanoindentation with a Berkovich tip was carried out to measure the hardness and Young's modulus value of the alloy after different number of ECAP pass. For comparison, nanoindentation was carried out for ARS sample also. The measured values of hardness and Young's modulus is shown in **Figure 4.13** against the total equivalent strain applied during each pressing of ECAP. There is a drop in hardness in 1st ECAP sample when compared to that of ARS sample. There is a slight increase in hardness after second pressing in ECAP. After that, the hardness continues to decrease with increase in number of pass in ECAP. The possible reason for this variation in hardness will be discussed in Chapter 5.

#### 4.4.4. Pseudoelasticity of Cold Rolled Samples

To find out the effect of cold rolling on the pseudoelasticity, conical indentation was carried out in all the samples after cold rolling and the degree of pseudoelasticity of rolled samples was compared with that of ARS sample. As discussed earlier, the pseudoelasticity in this work is measured by the depth recovery ratio calculated from load-displacement curve after indentation. **Figure 4.14** shows the depth recovery ratio (DRR) measured from a progressive multi-cycle (PMC) indentation cycle for ARS, 10CW, 20CW 50CW and 80CW Ti 50.8at.% Ni alloy. DRR was measured using equation 2.13 as described in section 2.4.2. The error bar represents the standard deviation calculated from six individual indentation measurements. From this figure, it is seen that the depth recovery ratio increase with increase in cold rolling and 80CW sample shows highest degree of pseudoelasticity. In addition, the recovery ratio is also increasing with the increasing load.

#### 4.4.5. Pseudoelasticity of ECAP Processed Samples

To find out the pseudoelastic recovery under indentation load, all the ECAP samples were subjected to simple indentation cycle at three different loads of 1N, 10N, and 20N. The same sphero-conical indenter with 200  $\mu\text{m}$  tip radius was used for the indentation. At each load, four different indentations were carried out, the depth recovery ratios were calculated from the load-displacement plot, and the result is shown in **Figure 4.15(a)**. The error bars represent the standard deviation measured from four different indentations. After indentations, the residual impressions were observed on all samples. The recovery ratios were calculated in the same as it was described in the earlier sections. In **Figure 4.15(b)** residual impressions of one set of indents made on each sample are shown. It is seen from **Figure 4.15(b)** that there is no impression seen in 2nd ECAP, 3rd ECAP and 4th ECAP

sample for the indent corresponding to 5N. It is clear that the depth recovery ratio increases with the increasing equivalent strain during ECAP process at each indentation load. In addition, the depth recovery ratio is quite high even at 20N load. For 3rd ECAP and 4th ECAP samples the recovery ratio at 20 N is 0.95 and 0.93 as against 0.77 and 0.81 for ARS and 1st ECAP sample respectively. However, one may argue that for the ARS sample the recovery ratio was measured at room temperature and for ECAP processed sample the recovery ratios were measured at 75 °C. However, in both cases the recovery ratio is measured in austenite phase and comparison between these samples is valid.

#### 4.4.6. Shape Memory Behaviour of ECAP Processed Samples

As the DSC results from **Figure 4.4** and **4.5** show that after ECAP at 450 °C, the alloy becomes martensitic at room temperature. To find out the shape memory ability of the alloy after different number of ECAP pressing spherical indentation was carried out at 0.5 N, 1 N, 5 N, 10 N and 20 N at room temperature (21 °C). The images of the indents were captured using optical profilometer at room temperature and after heating the samples to 75 °C because as seen from **Figure 4.5**, at this temperature the structure in ECAP processed alloy is completely austenitic. In **Figure 4.16** the top-view of residual impression of spherical indents made at different loads for 1st ECAP, 2nd ECAP, 3rd ECAP and 4th ECAP samples is shown. The left hand side view correspond to the image of indents before heating (BH) and the right hand side view corresponds to the image of indents after heating (AH), taken at 75 °C. The coloured scale bar shows the depth in µm.

**Figure 4.17** shows the cross sectional profile of the indent made at 20 N for all ECAP samples before and after heating. From this figure, it is seen that the 2nd ECAP sample has the smallest indentation depth before heating, however there is very small difference in the

residual indent depth among all the four samples after heating. This difference in maximum indent depth could be because of the hardness variation in the sample. As it is seen from **Figure 4.13**, the 2nd ECAP sample has the highest hardness value.

#### **4.5. Scratch Experiments**

During indentation, the loading is static and in most of the practical applications, the contact surfaces undergo deformation during sliding or rolling. To observe the effect of cold rolling on pseudoelastic recovery under loading conditions similar to practical applications, scratch testing under progressive loading was carried out.

##### **4.5.1. Scratch Testing of Cold Rolled Samples**

A conical indenter with  $269\mu\text{m}$  tip radius was used to make the scratch in progressive loading mode starting from 0.01 N to 10 N. The scratch length was 2mm and the scratch speed was 2mm/min. **Figure 4.18** shows the scratch depth profile along the length of the scratch for ARS sample and cold rolled samples. The broken lines indicate the scratch depth under loading, i.e. while making the scratch. The solid lines indicate the residual scratch depth after unloading measured by WYKO. The scratch depth is shown for the last 0.825 mm of the scratch because the scratch length was 2 mm and the total length of the scratch was not possible to be recorded in one image at the lowest magnification (5X) used. To have better visual representation of the scratches made different samples, 3D WYKO images of the scratches made on ARS and rolled sample is shown in **Figure 4.19**. From this figure, it is clear that with increase in rolling reduction the amount of pile-up is decreasing, 80CW sample showing the least amount of pile-up.

As it is seen from **Figure 4.18**, the depth profile shown is along one line corresponding to the deepest point of the scratch (AA'). It is also of interest to view the cross-section of the residual scratch depth perpendicular to the scratch direction. **Figure 4.20** shows the cross section profile of the scratches made on ARS and cold rolled samples where the residual depth profile is measured at a position corresponding to the maximum load, i.e., at 10N. Six individual scratches were made on each sample and average maximum scratch depth during loading and average residual scratch depth after unloading was calculated. **Figure 4.21** shows the summary of scratch testing, where the average maximum depth during loading and average residual scratch depth after unloading is plotted against the thickness reduction in cold rolling.

#### **4.5.2. Scratch Testing of ECAP samples**

The scratch testing of the ECAP samples were done at 75 °C to measure the pseudoelastic recovery under scratch loading, because at this temperature the structure is completely austenitic. The progressive loading was used starting from 0.1 to 10 N with a sphero-conical indenter with 200 µm tip radius. The scratch depth during loading was recorded by the scratch tester and after the unloading the scratches were observed using WYKO optical profilometer at 75 °C to measure the residual scratch depth. Total three scratches were performed in each sample. The average scratch depth and average residual depth is calculated and plotted in **Figure 4.22**. The point to be noted here is that all the scratches were made in austenite phase to see the recovery due to SIM transformation under load and then back transformation upon removal of the load.

The result shows that after first and second pressing in ECAP, the average scratch depth measured at maximum load (10 N) in respective sample was very high compared to the

sample after 3rd and 4th pressing in ECAP. However, there is not very much difference in the residual scratch depth in all the samples after ECAP. To do a comparison similar scratch was performed in ARS sample. While the scratch depth in ARS sample is lower compared to all ECAP samples, the residual scratch depth in ARS sample is higher than the ECAP samples. **Figure 4.23** shows the 3D images of residual depth of one scratch on each sample measured by WYKO.



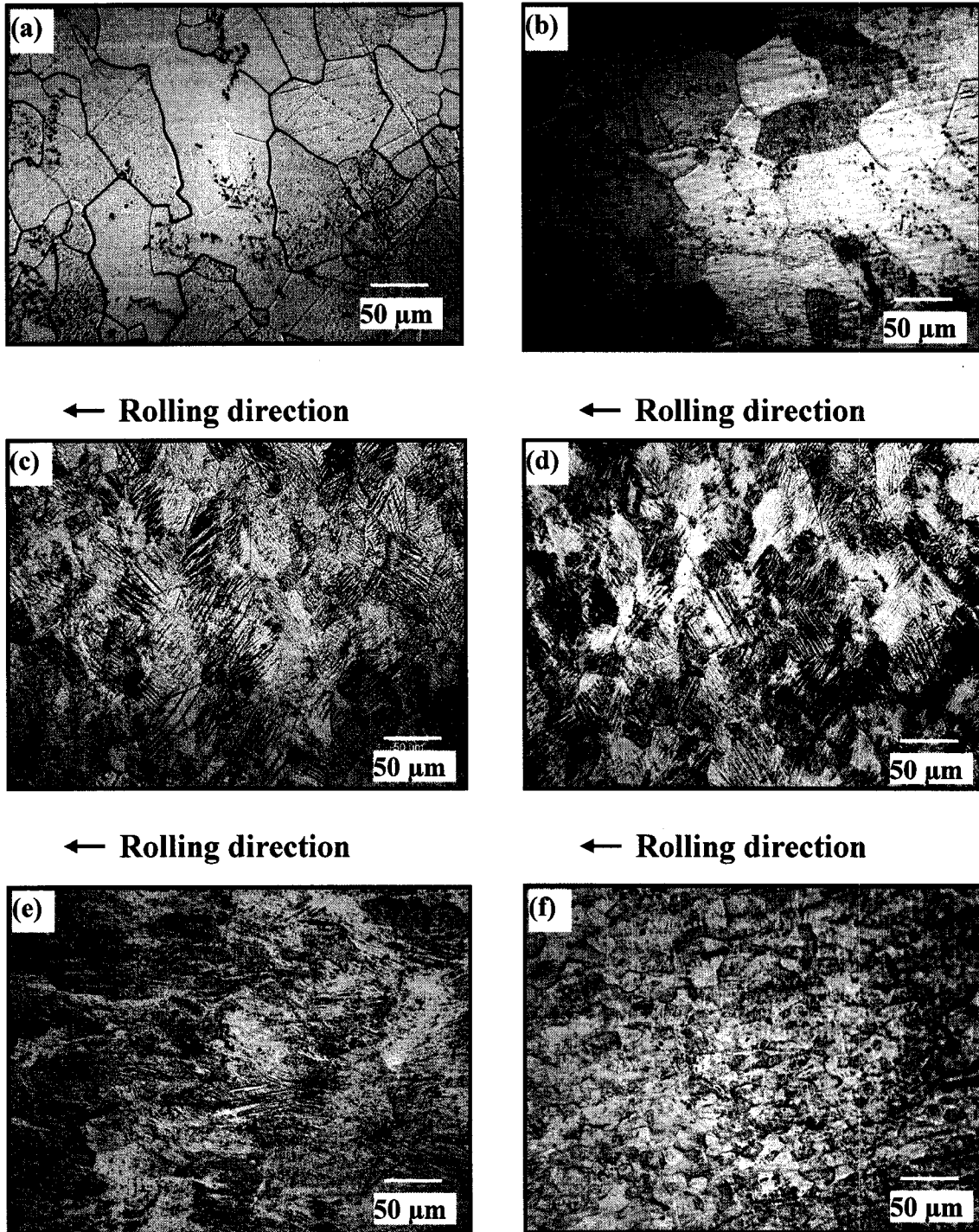


Figure 4.1. Optical microstructure of (a) as received; (b) solutionised; (c) 10CW; (d) 20CW; (e) 50CW and (f) 80CW sample. Intermediate annealing was done for 50CW and 80CW sample at 600 °C for 15 min.

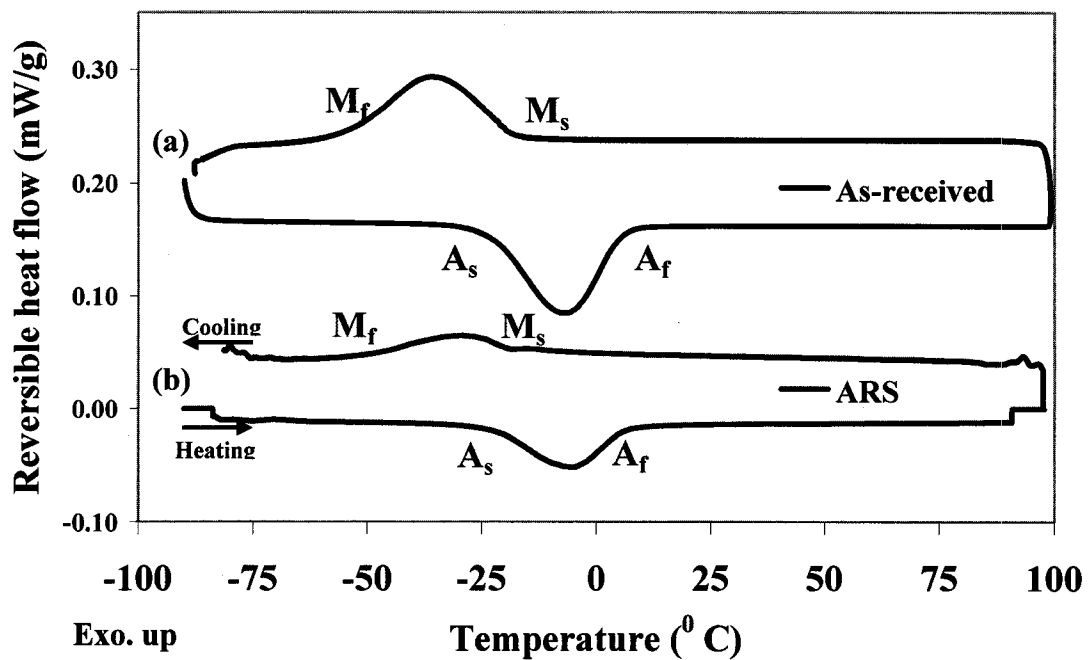
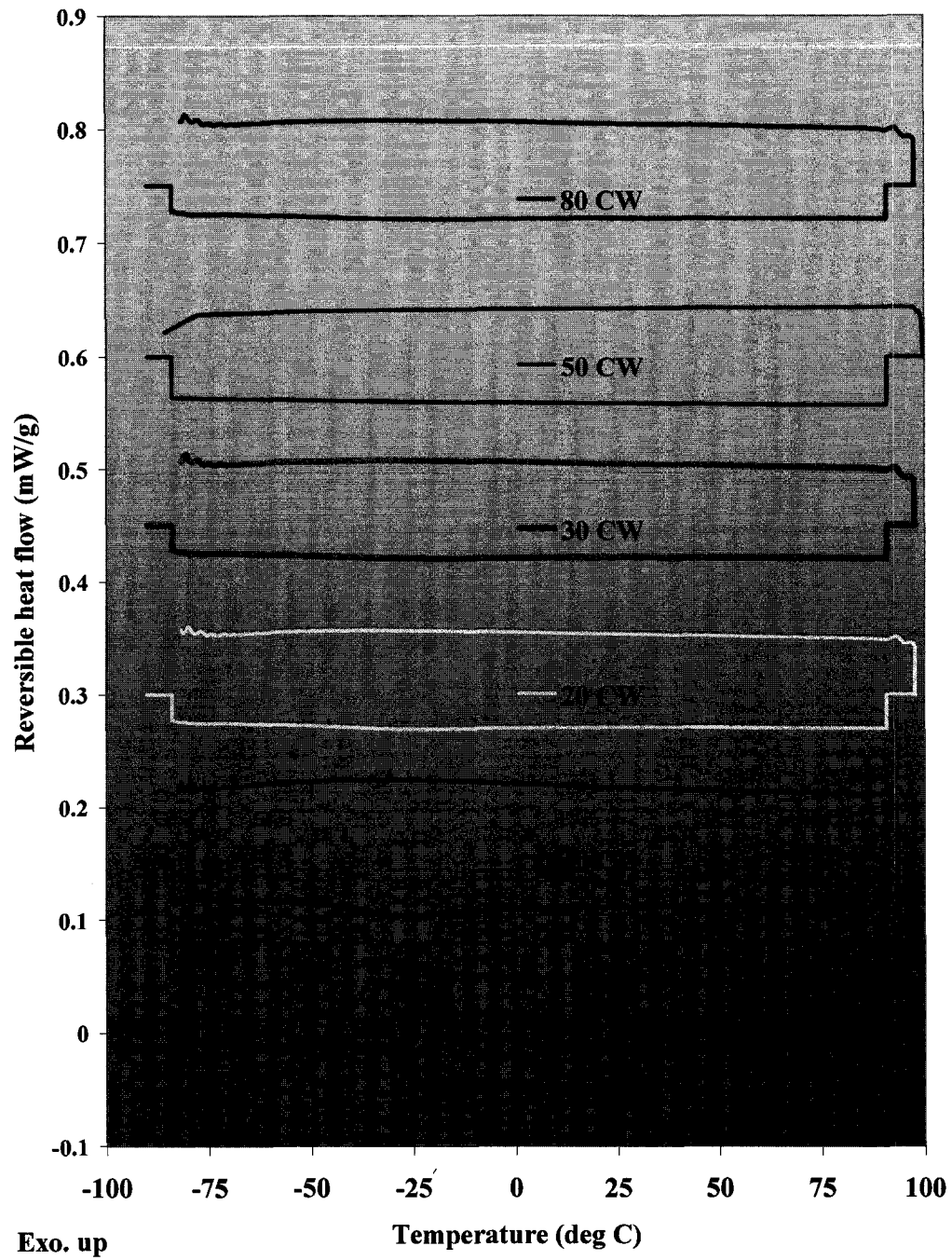


Figure 4.2. Differential scanning calorimeter profile of (a) as-received alloy and (b) as-received alloy after solution treatment and quenching (ARS)



**Figure 4.3.** DSC profiles for various cold rolled samples. Intermediate annealing was done for 50CW and 80CW sample at 600°C for 15 min. The legend inside each profile corresponds to the sample name.

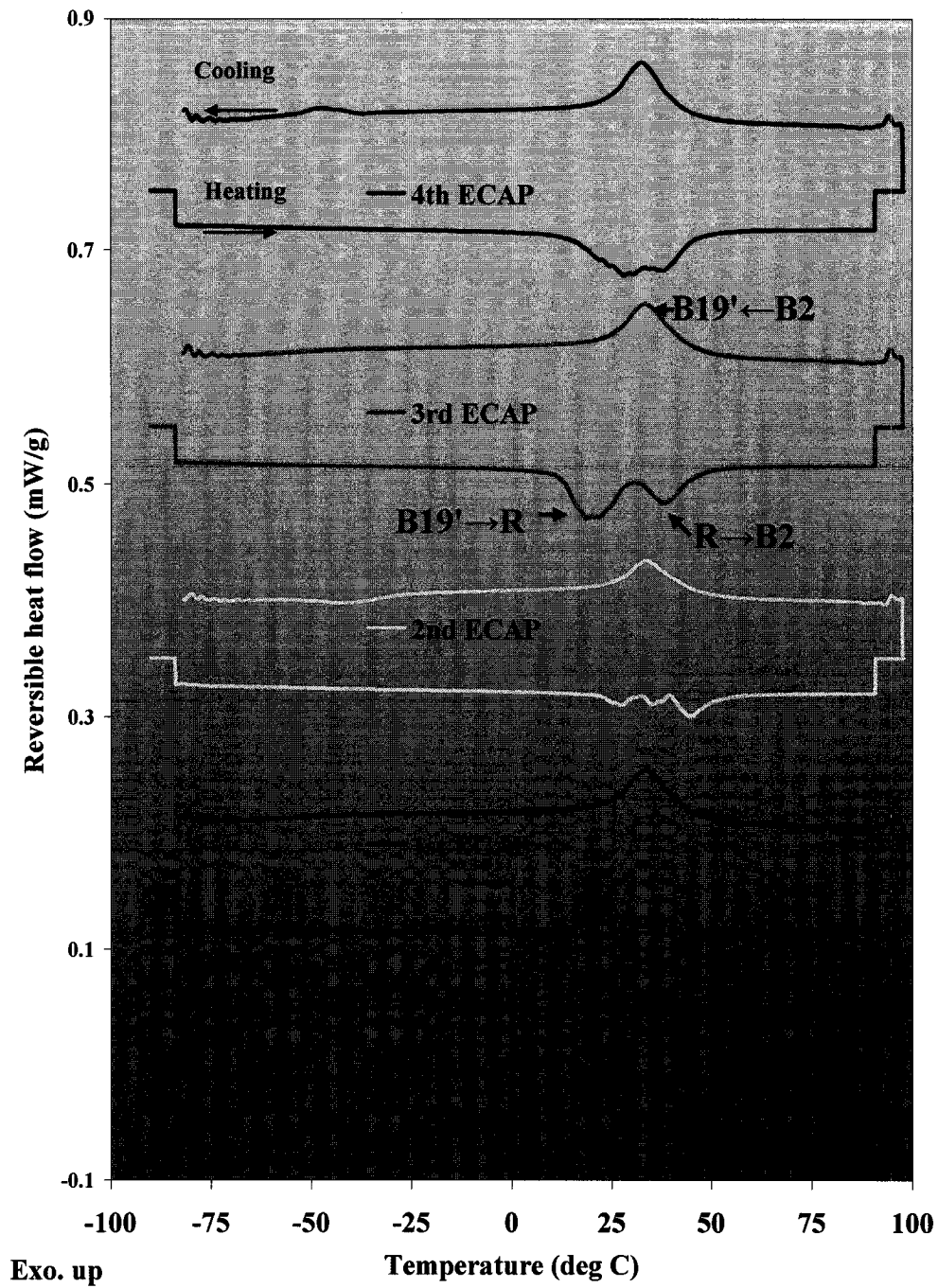


Figure 4.4. DSC profile for ARS and ECAP samples. The equivalent strain in solutionised, 1st ECAP, 2nd ECAP, 3rd ECAP and 4th ECAP sample are 0, 0.64, 1.27 1.91 and 2.54, respectively. The legend inside each profile corresponds to the sample name.

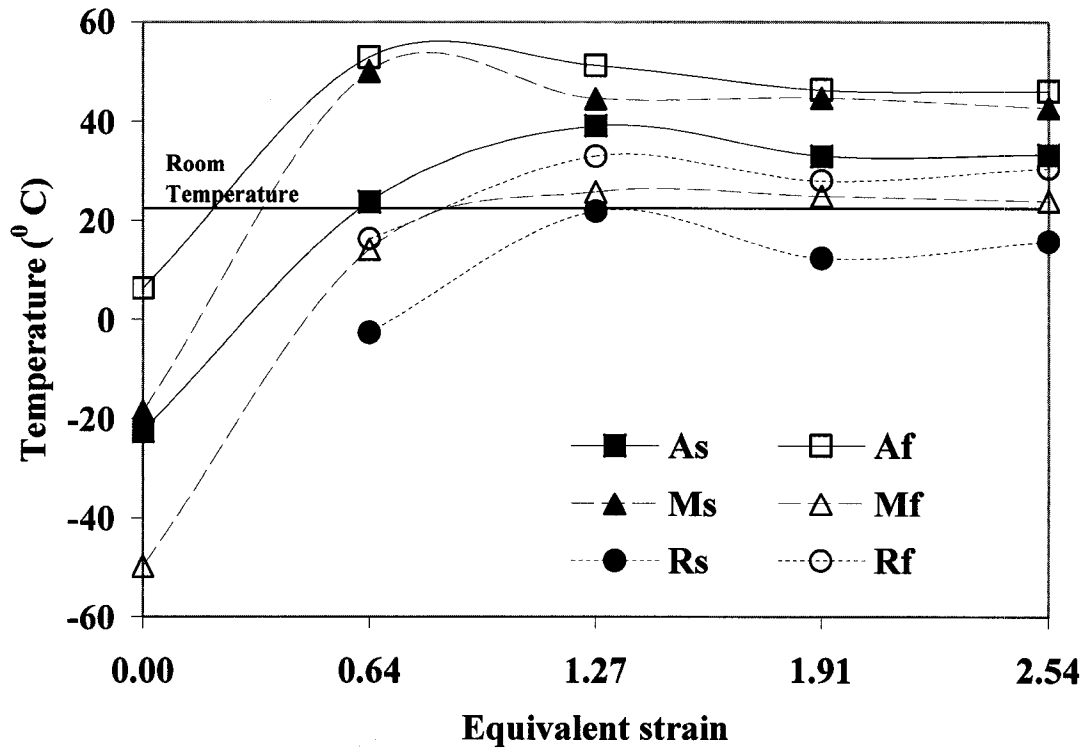


Figure 4.5. Transformation temperatures of Ti 50.8at.% Ni after various passes of ECAP. The X-axis shows the total equivalent strain applied during ECAP. Equivalent strain of 0 indicates ARS sample.

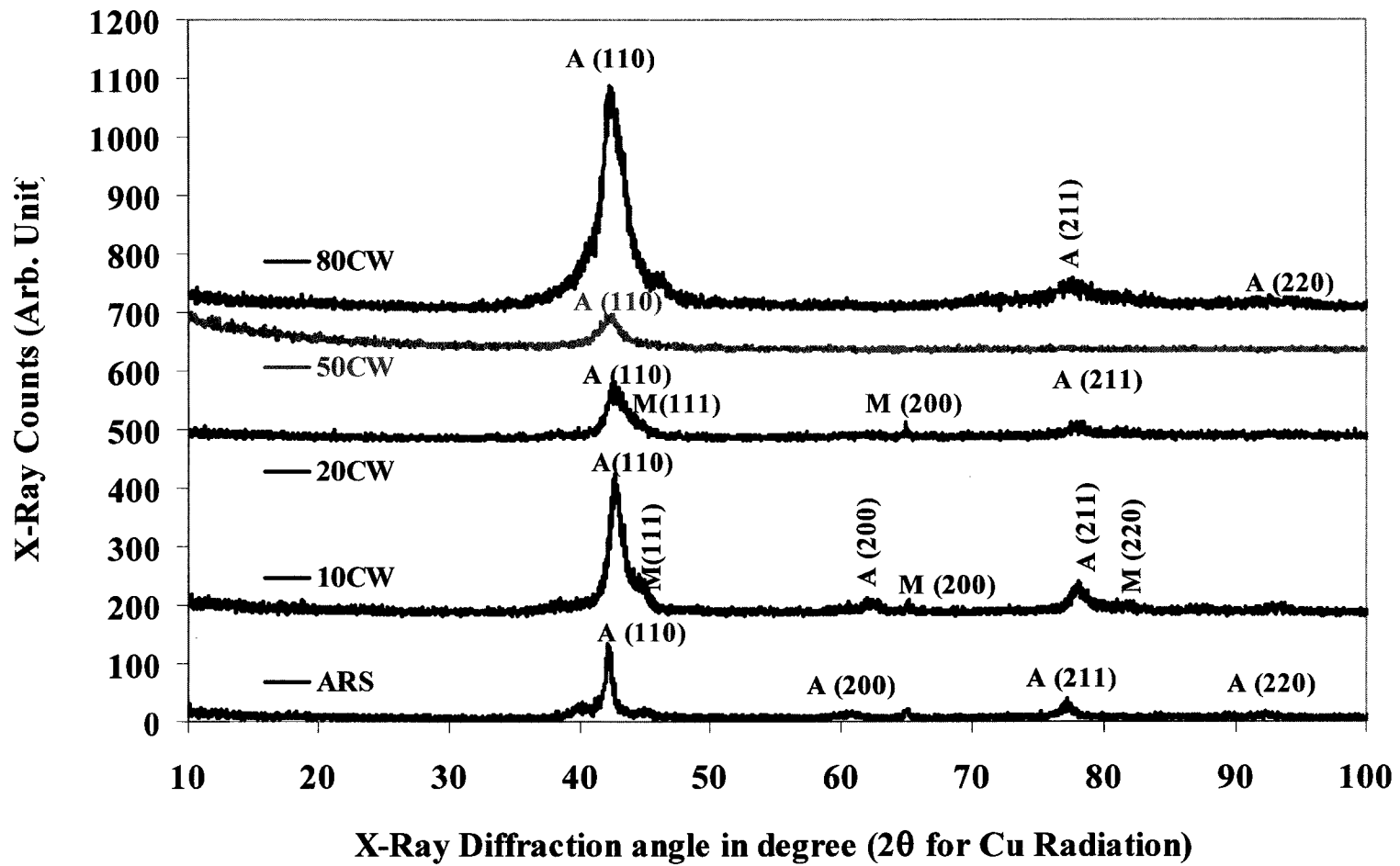


Figure 4.6. X-Ray diffraction analysis of Ti 50.8at.% Ni ARS sample and after cold rolling to 10, 20, 50 and 80% thickness reduction.

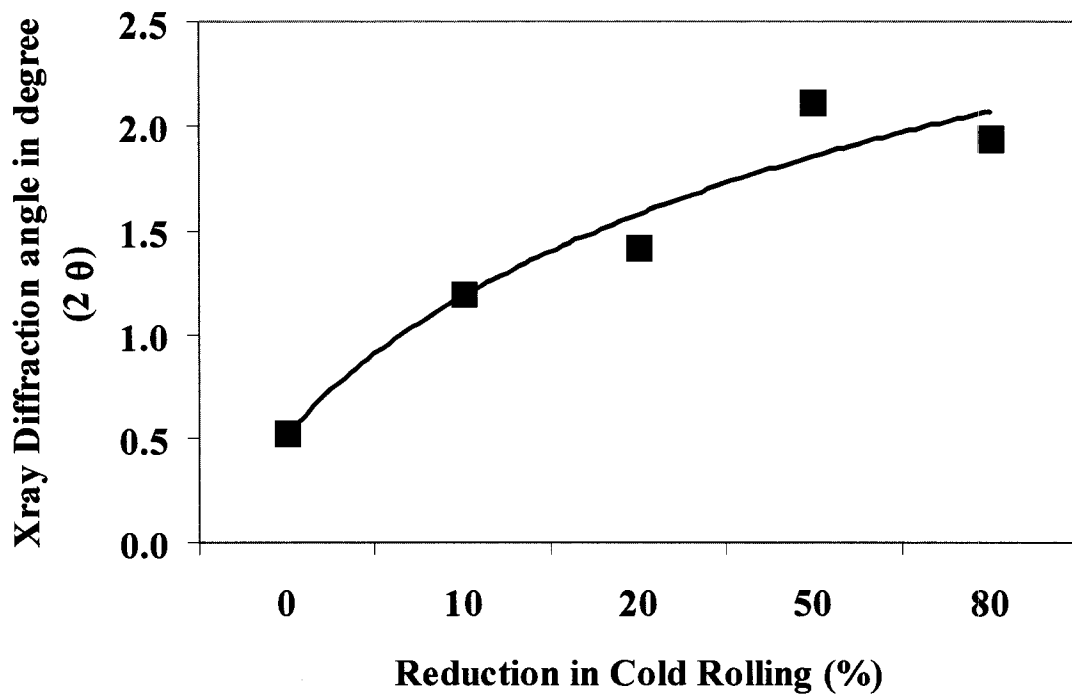


Figure 4.7. Typical full width half maximum of  $(110)_{B2}$  peak in ARS and cold rolled samples. (0% reduction indicate ARS sample)

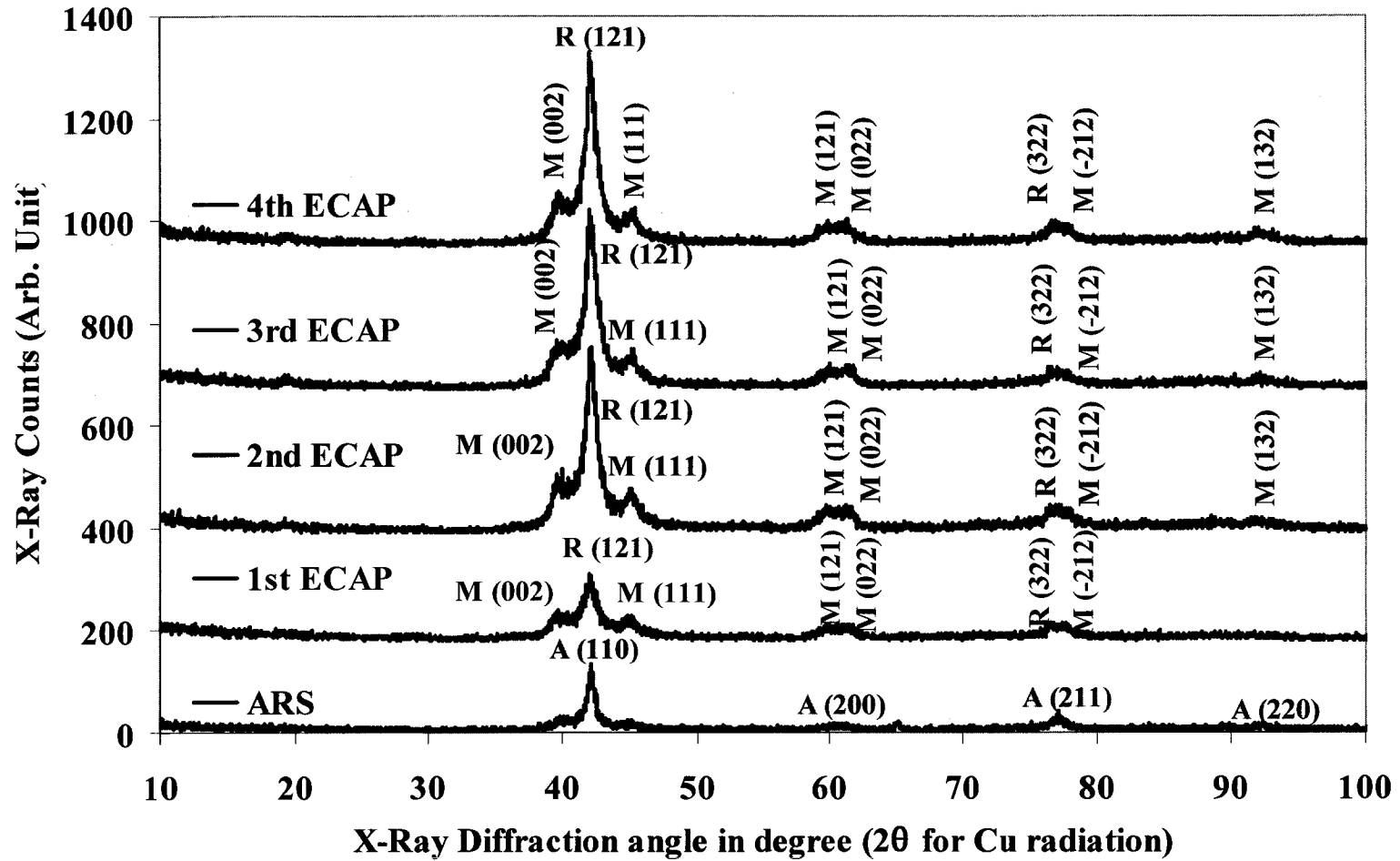


Figure 4.8. X-ray diffraction analysis of Ti 50.8at.% Ni alloy after various passes of ECAP. Data for ARS sample is also shown.



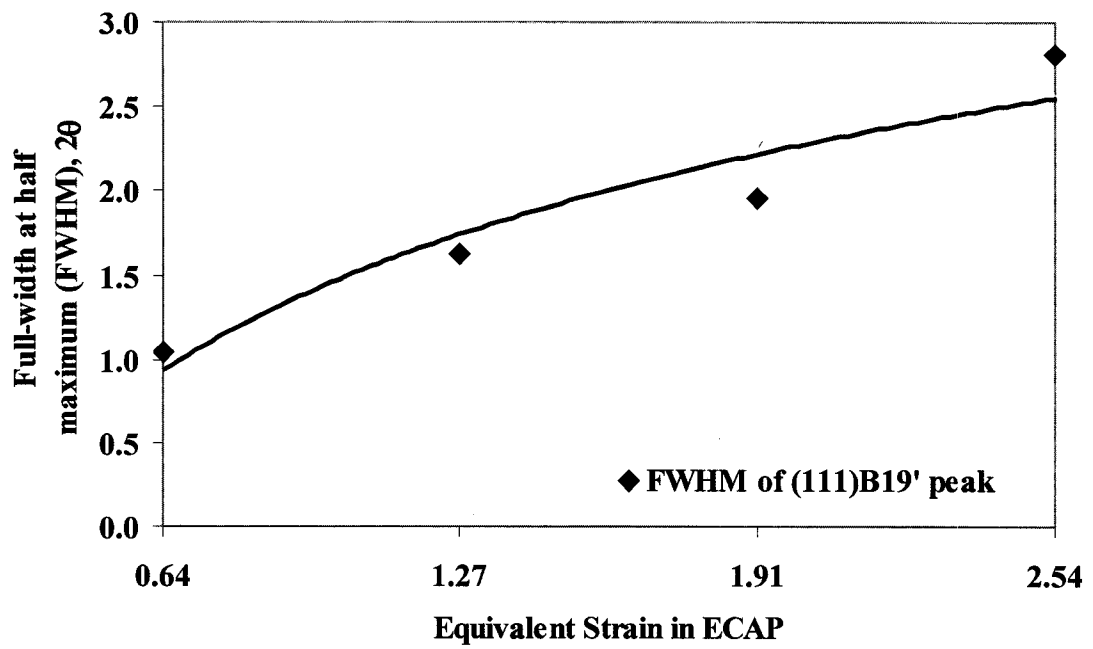


Figure 4.9. Typical full width half maximum of (111) B19' peak in various ECAP samples.

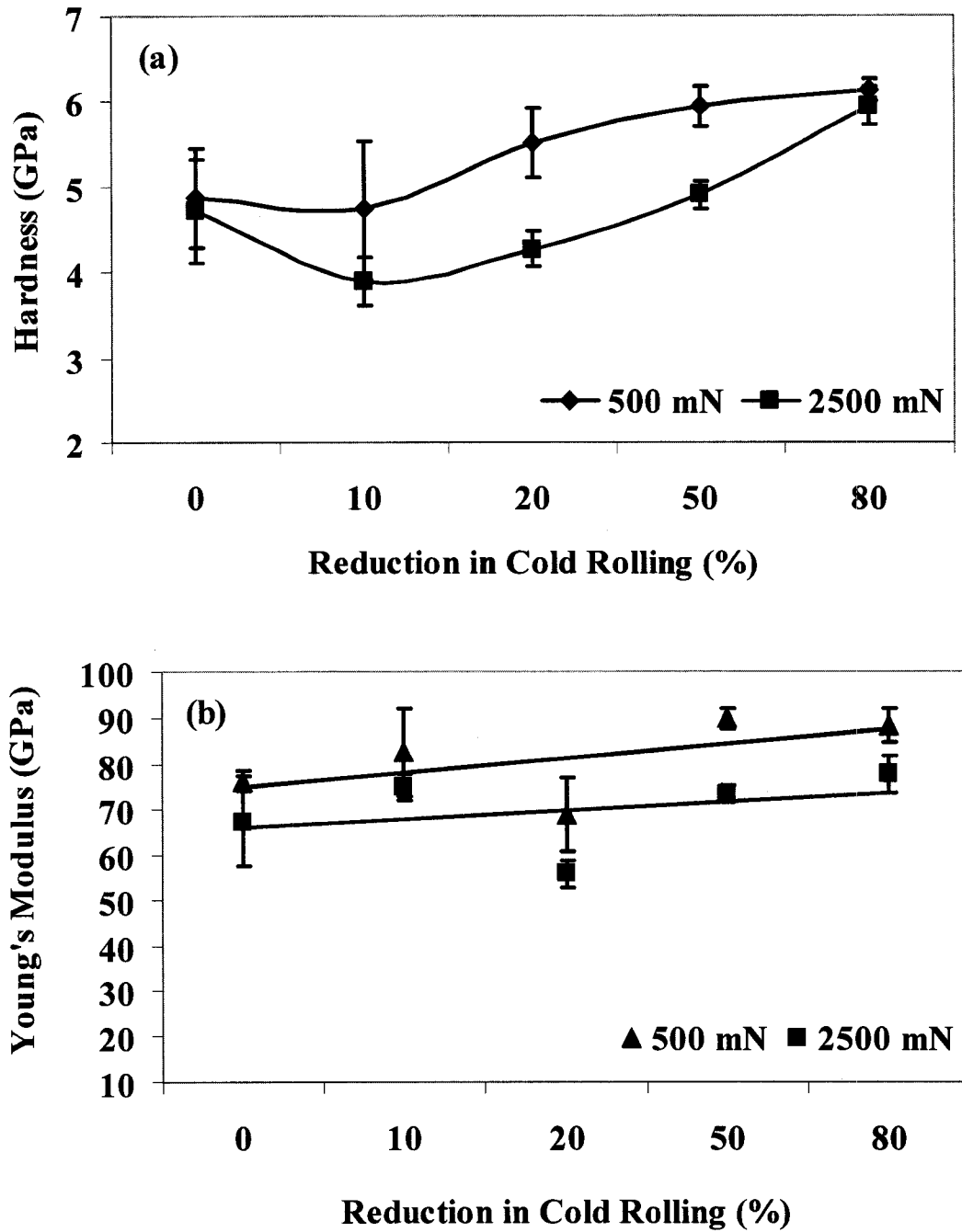


Figure 4.10. (a) Hardness and (b) Young's modulus of ARS and cold rolled Ti 50.8at.% Ni samples measured during progressive multi-cycle indentation using a Berkovich indenter at 500 mN and 2500 mN indentation loads.

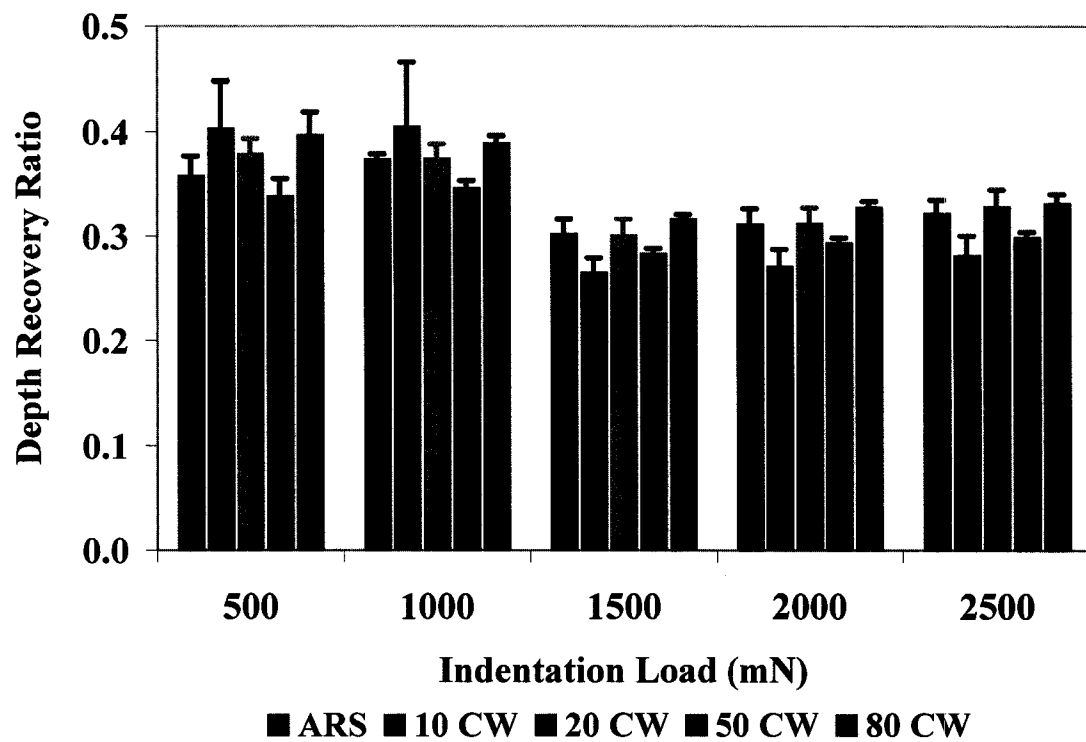


Figure 4.11. Depth recovery ratio of ARS and cold rolled samples during progressive multi-cycle indentation using a Berkovich indenter.

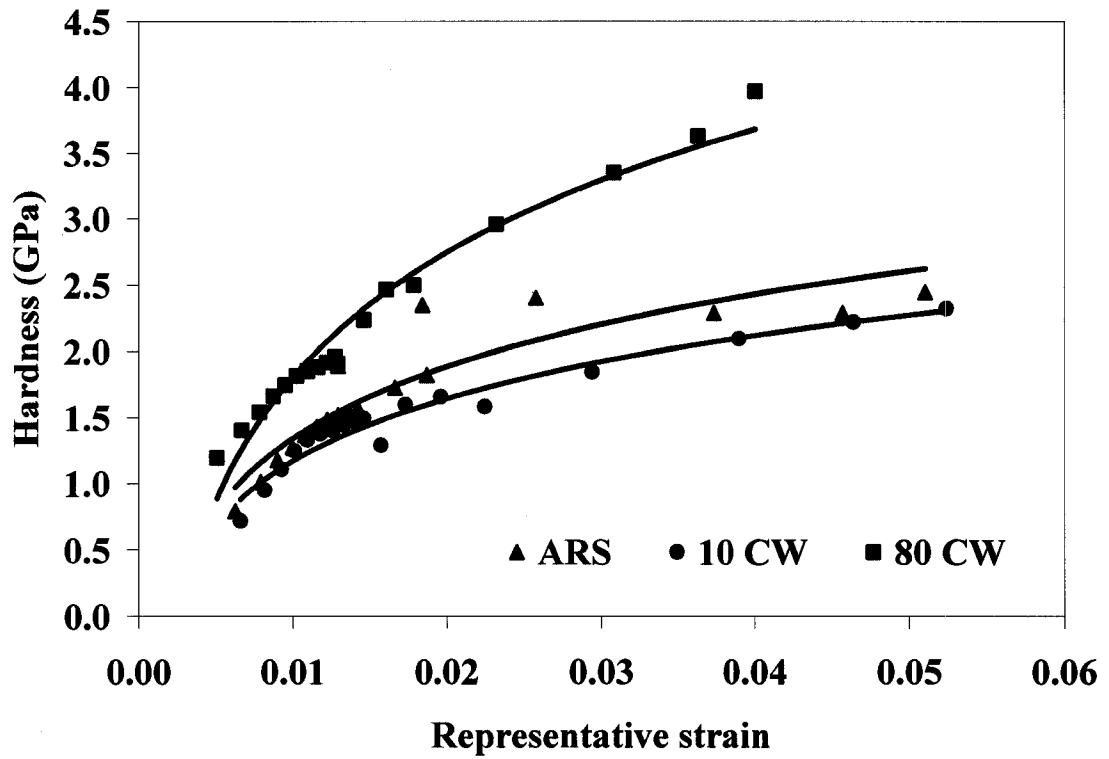


Figure 4.12. Plot showing hardness vs. representative strain for ARS, 10CW and 80CW sample. The data is from two different PMC indentation experiments.

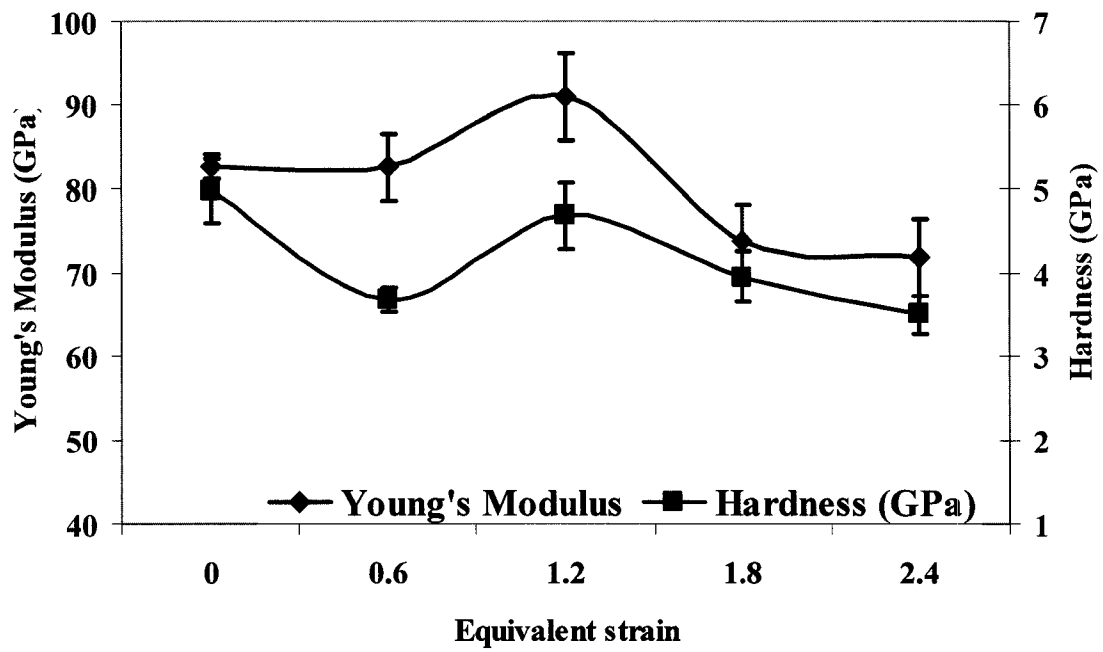


Figure 4.13. Hardness and Young's modulus of ARS and ECAP processed Ti 50.8at.% Ni samples measured during nanoindentation using a Berkovich indenter at 100 mN.

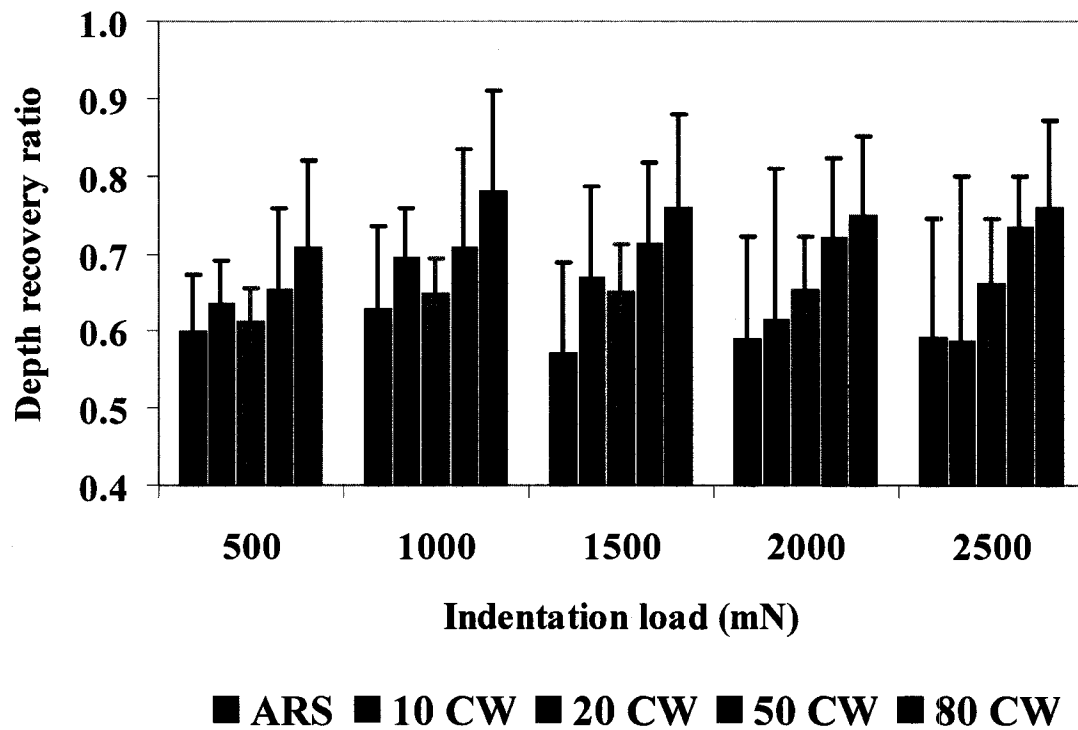


Figure 4.14. Depth recovery ratio of ARS and cold rolled samples during progressive multi-cycle indentation using a conical indenter with 107  $\mu\text{m}$  tip radius.

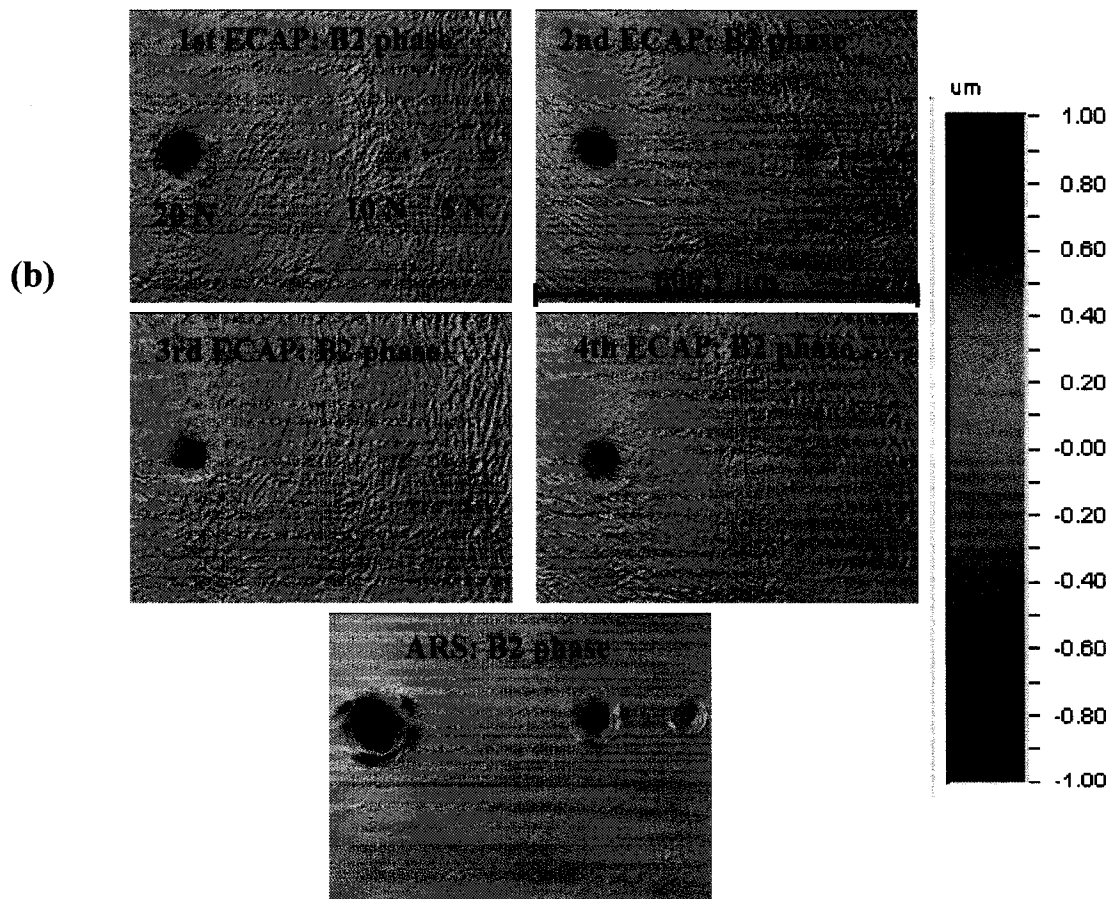
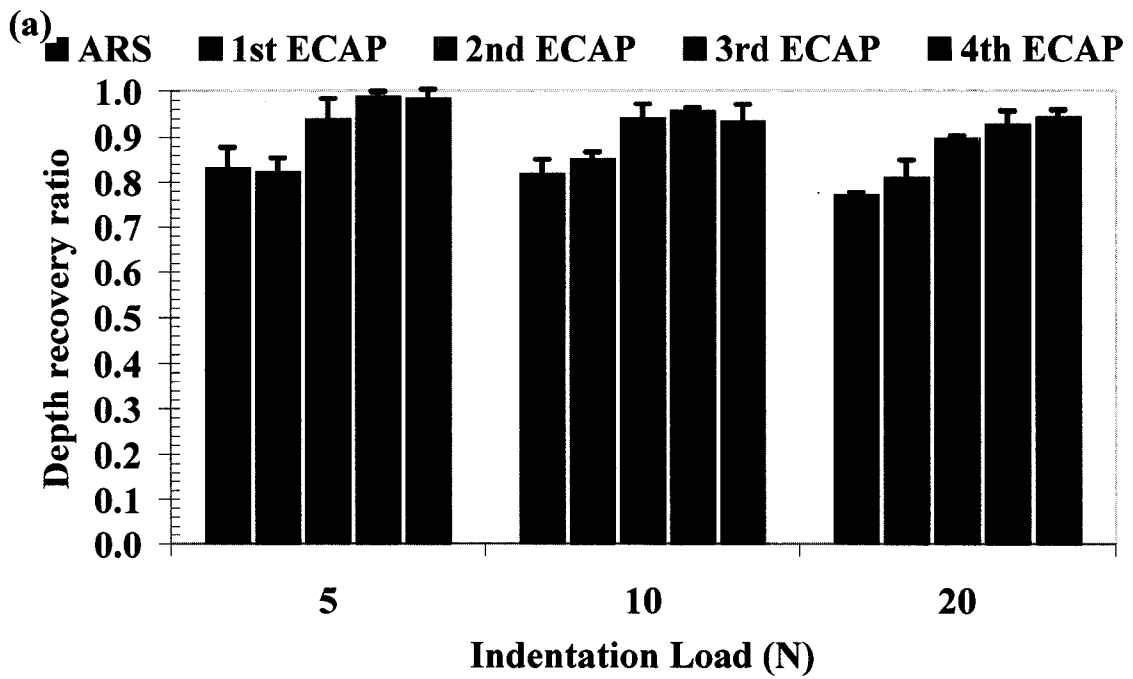
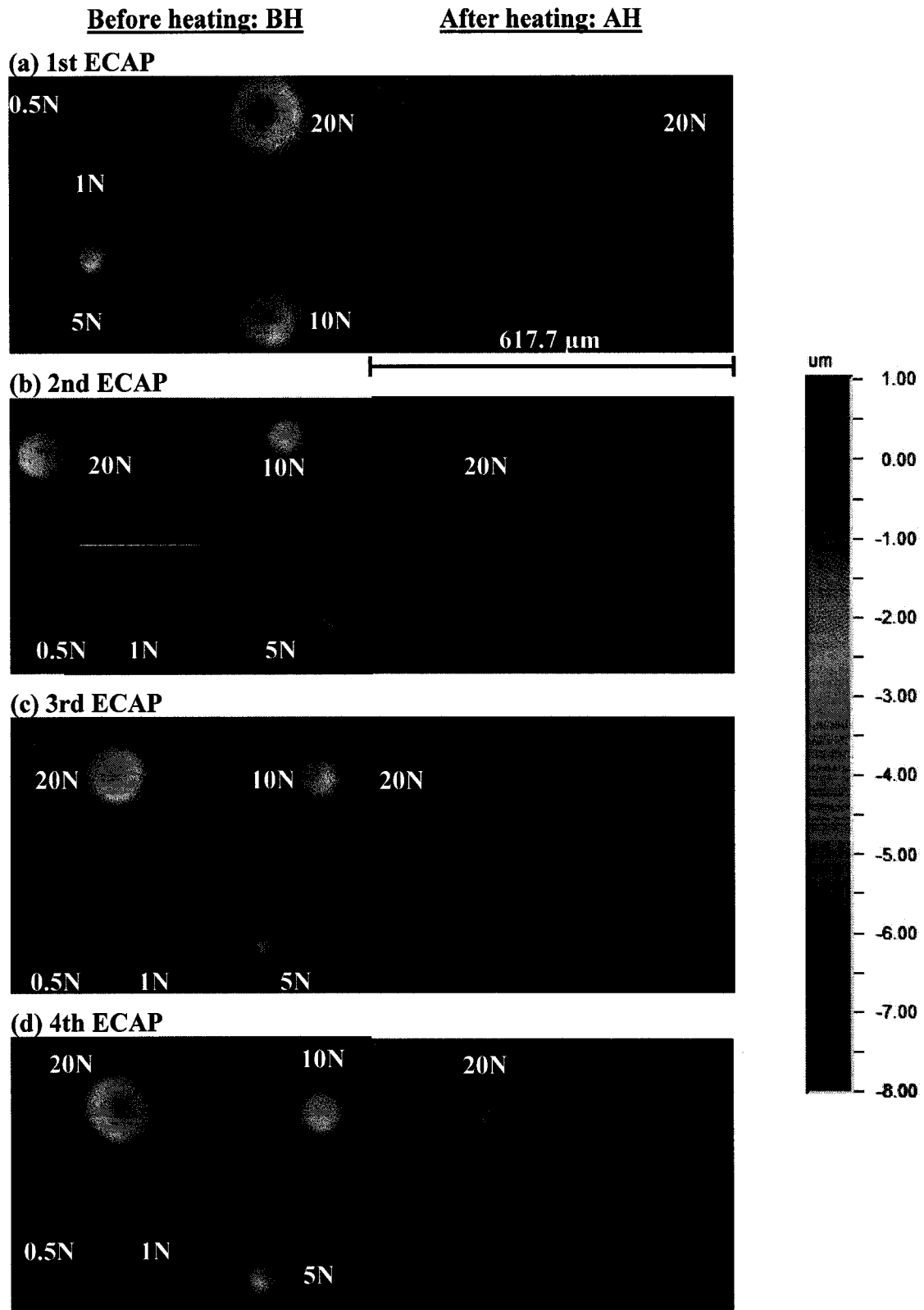


Figure 4.15. (a) Depth recovery ratio of ARS measured at room temperature and ECAP samples measured at three different loads at 75 °C; (b) Residual impression of one such set of indents for ARS and ECAP samples taken from WYKO optical profilometer.



**Figure 4.16.** WYKO 2D images of indent recovery of Ti 50.8at.% Ni samples after ECAP showing SME at various loads; BH: before heating, AH: after heating.



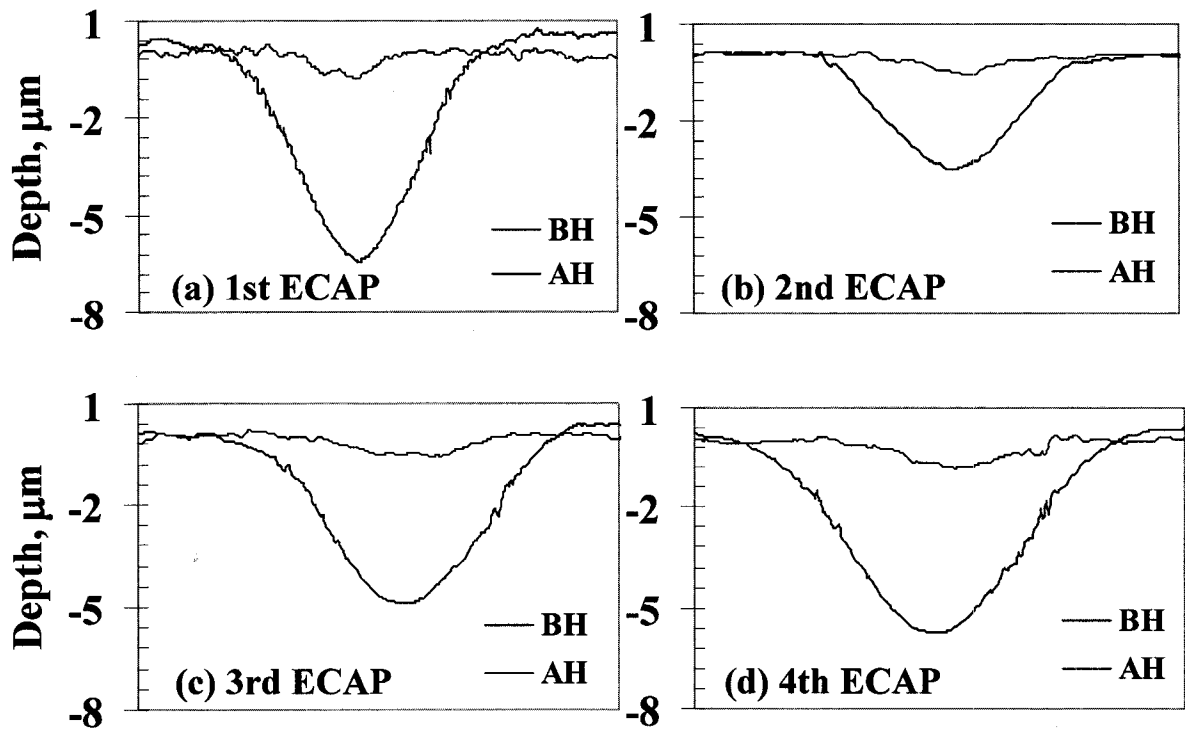


Figure 4.17. Cross section of the indents made on (a) 1st ECAP, (b) 2nd ECAP, (c) 3rd ECAP and (d) 4th ECAP sample before heating (BH) and after heating (AH) at 20N load

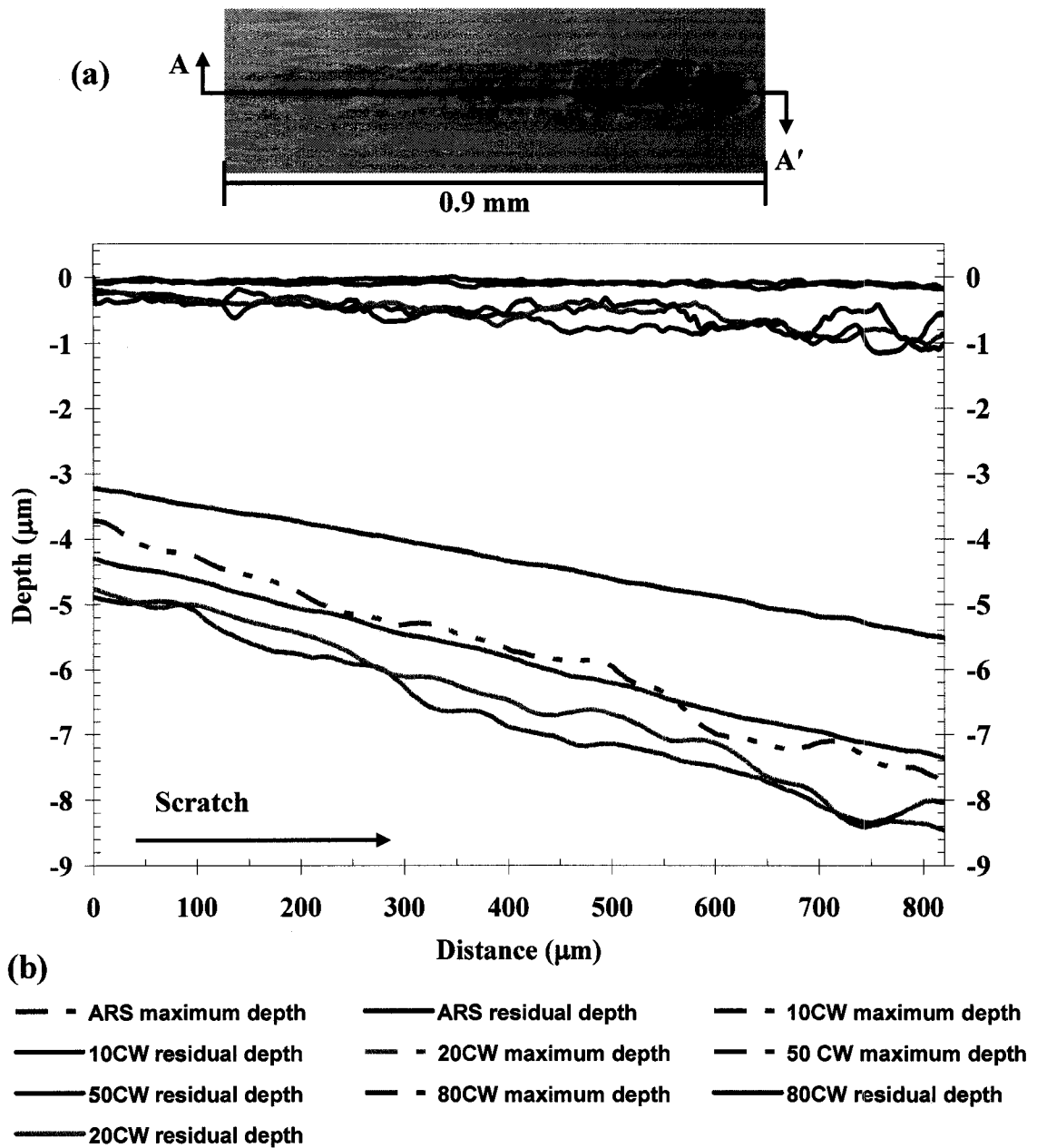
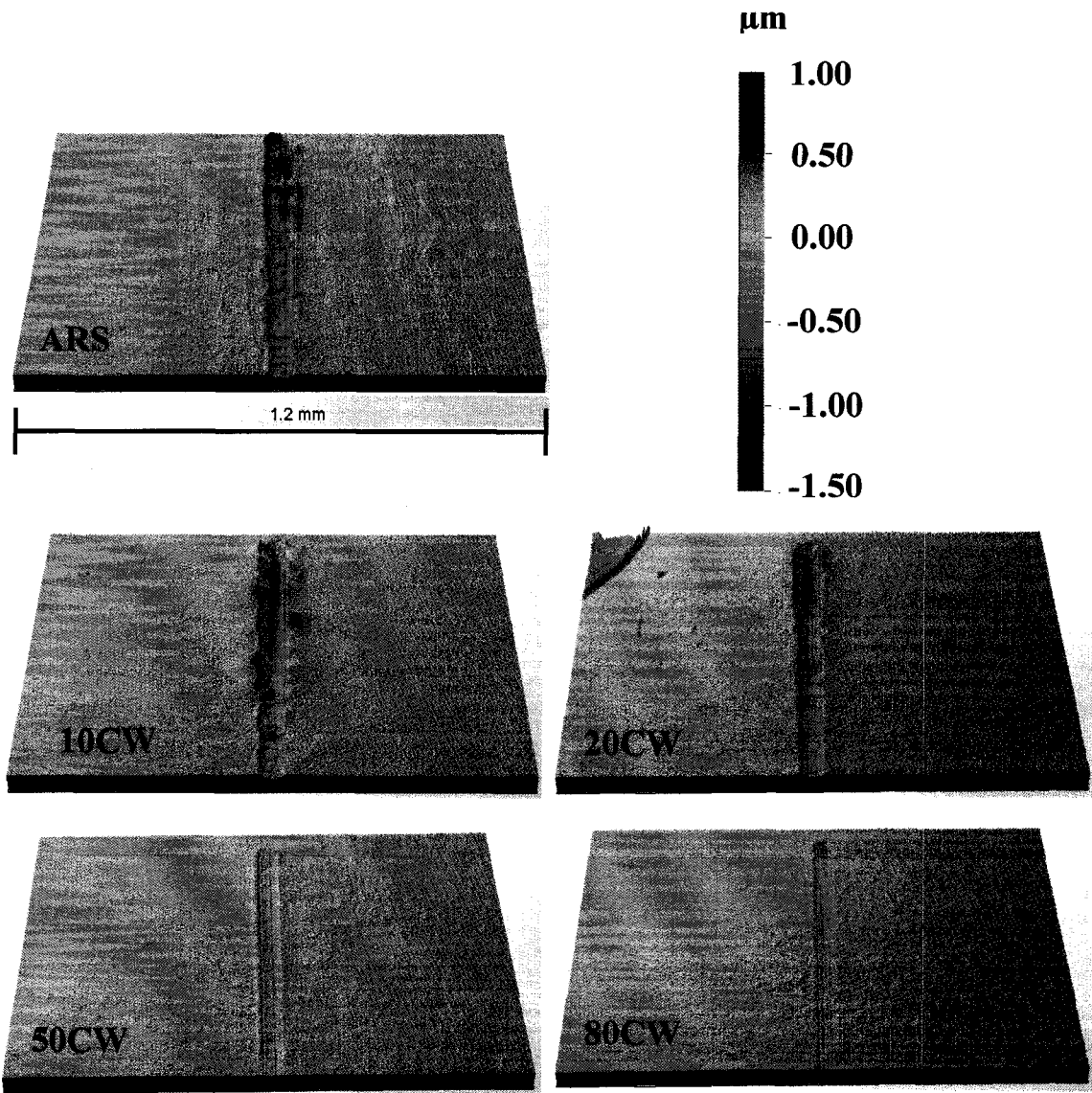


Figure 4.18. (a) WYKO optical surface profile image of a typical scratch showing the position from where the depth is measured (only 0.825 mm of the scratch distance is shown); (b) Maximum scratch depth (during loading, measured by scratch tester) and the residual scratch depth (after unloading, measured by WYKO) profile along the length of the scratch showing the pseudoelastic recovery of ARS and cold rolled Ti 50.8at.% Ni sample.



**Figure 4.19.** WYKO 3D optical surface profilometer images of the scratches made on ARS and cold rolled Ti 50.8at.% Ni samples showing PE effect. Only half of the scratch length ( $\sim 1$  mm) is shown.

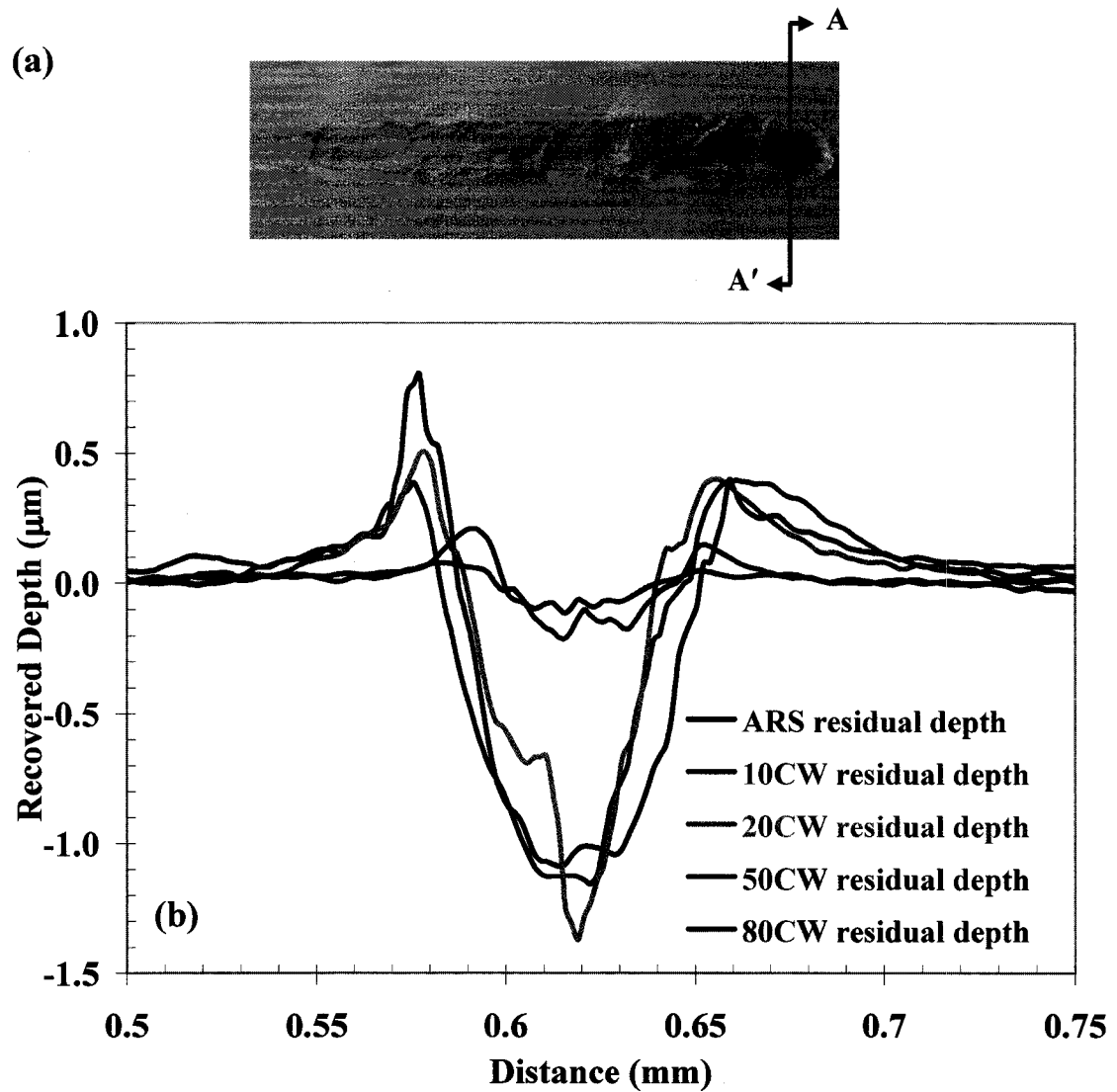


Figure 4.20. (a) Optical surface profile image showing how the depth along the cross section profile was taken; (b) The cross section profile of the recovered scratches at the maximum depth corresponding to 10N load, measured from WYKO images. The depth indicates recovered depth after unloading.

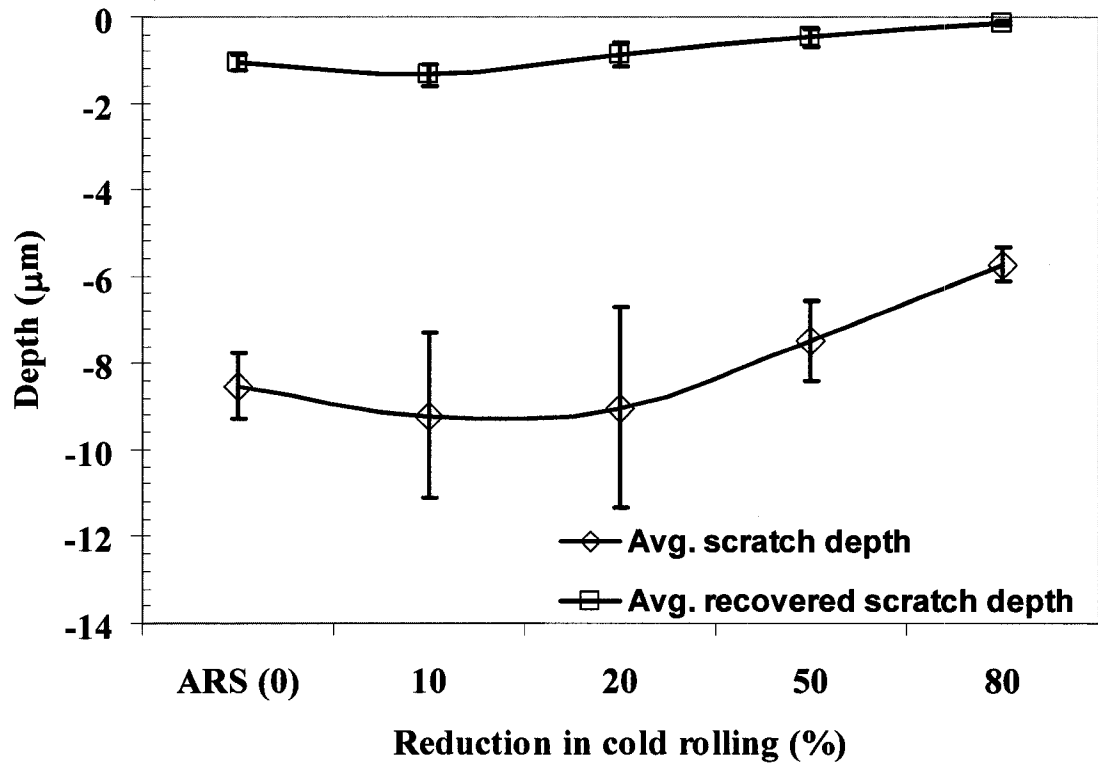


Figure 4.21. Average scratch depth (during loading) and average recovered scratch depth (after unloading) at maximum scratch load of 10 N for ARS and cold rolled Ti 50.8at.% Ni sample. The error bar indicates six individual measurements on each sample.

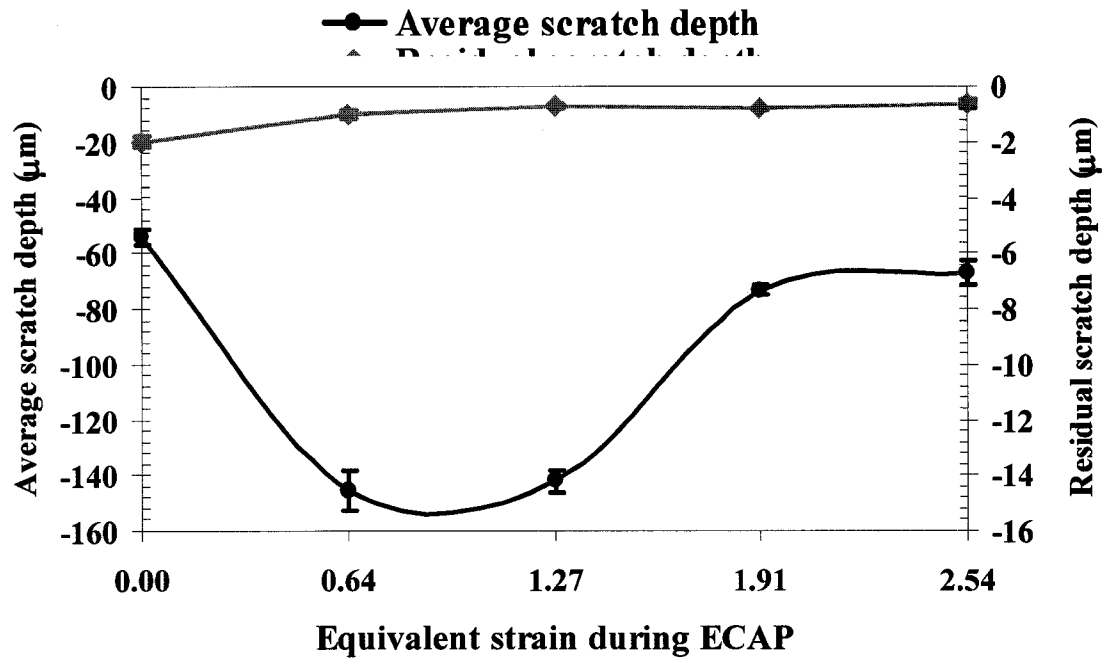
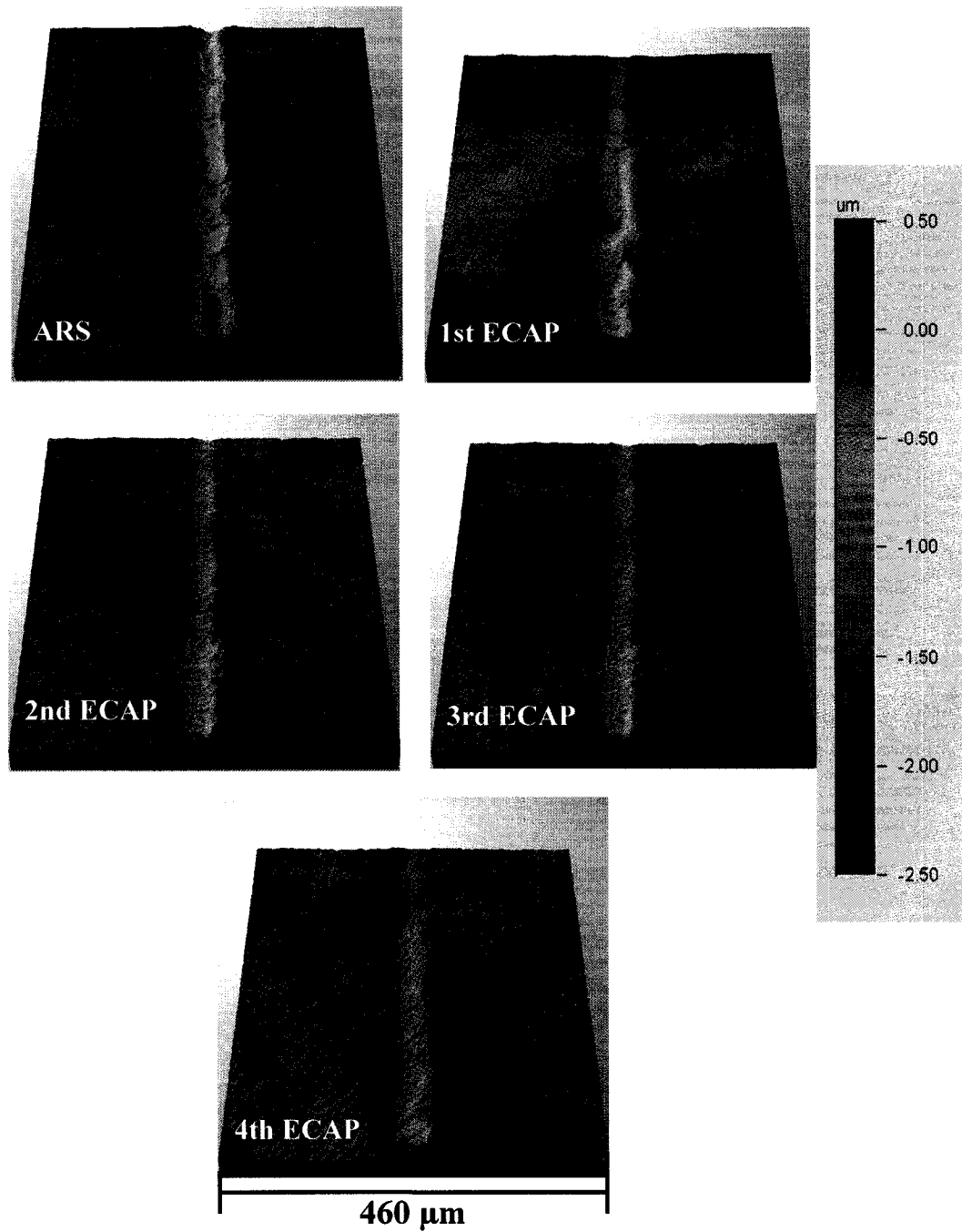


Figure 4.22. Average scratch depth and residual scratch depth measured at a point corresponding to the maximum load (10N) applied during the scratch for ARS, 1st ECAP, 2nd ECAP, 3rd ECAP and 4th ECAP sample. The scratch tester measures the scratch depth and the optical profilometer measures the residual depth. (Zero equivalent strain during ECAP represents ARS sample)



**Figure 4.23. 3D optical surface profiles of the residual scratch depths on ARS, 1st ECAP, 2nd ECAP, 3rd ECAP and 4th ECAP sample.**

## **CHAPTER 5**

### **5. Discussion**

In this chapter, the results obtained by DSC, X-ray diffraction and instrumented indentation and scratch technique, which were presented in the previous chapter, will be discussed. First, the optical microstructure carried out for cold rolled sample will be discussed. Then the martensitic transformation temperatures and transformation behaviour of cold rolled and ECAP processed samples will be discussed using the thermodynamics of the martensitic transformation. The martensitic transformation path in ECAP processed samples will be explained by possible chemical inhomogeneity after the deformation and ageing in the die. The X-ray diffraction results after cold rolling and ECAP will be discussed and a possible explanation for austenite stabilisation after 80% cold rolling reduction and martensite stabilisation after ECAP processing will be given. The pseudoelastic recovery behaviour of cold rolled samples measured by instrumented indentation and scratch technique will be discussed to explain why 80CW sample shows the maximum damage recovery. After ECAP processing, the pseudoelastic and shape memory behaviour of Ti 50.8at.% Ni alloy will be discussed and how the applied strain during deformation controls the degree of pseudoelastic and shape memory behaviour will be presented.

#### **5.1. Microstructures As Determined By Optical Micrography**

The optical micrography does not give much information on the microstructure of the binary TiNi alloys. Specially, when the alloys are deformed heavily, the grain boundaries become fuzzy under optical microscope. However, from the micrograph



shown in **Figure 4.1**, some distinct features are revealed. In as-received sample, the structure was inhomogeneous; irregular shaped and different sizes of grains were seen, which was expected in hot rolled condition. When the as-received alloys is solutionised and quenched (ARS sample) the structure becomes homogeneous and equiaxed grains of austenite phase is seen. In case of 10CW and 20CW sample lenticular shaped surface morphology is seen inside the austenite grains. In addition, the grain boundaries are not well defined in these two samples unlike as-received and ARS sample. When the alloy is further deformed, in case of 50CW and 80CW sample, there is hardly any trace of grain boundaries; instead, heavily deformed banded structure is seen in these two samples. In case of 80CW sample, some granular shaped morphology is seen without clear definition of any grain boundaries.

## **5.2. Experimental Determination of Phase Transformation Temperatures**

The transformation temperatures of Ni rich TiNi alloys are very sensitive to any kind of heat treatment. The transformation temperature changes significantly with small change in temperature during heat treatment and any kind of strain applied in the material prior or after the treatment. It can be seen from the **Figure 4.2** and **Table 4. 1**, that solution treatment at 900 °C followed by quenching inside a quartz tube changes not only the forward and reverse transformation temperatures, but also peak broadening is seen. There is a change in the hysteresis (total span of the transformation temperature, i.e. the difference between  $A_f$  and  $M_f$ ) of the martensitic transformation. In case of as-received alloy, the transformation temperature hysteresis is 45 °C whereas the same after solution treatment is 56 °C, an increase of 11 °C. This change in transformation hysteresis is important from practical application point of view as this can be altered using heat

treatment to suit the applications need. Before we discuss further on the martensitic transformation behaviour of cold rolled and ECAP processed samples, thermodynamics of martensitic transformation will be reviewed briefly in the following subsection.

### 5.2.1. Thermodynamics of Martensitic Phase Transformation

Consider the **Figure 5.1**, which shows a schematic diagram of free energy-temperature relationship for a thermoelastic martensitic transformation. Tong & Wayman [116] suggested that in case of thermoelastic martensitic transformation, free energy balance at some point of transformation temperature can be given by the following equation:

$$\Delta G^{P \rightarrow M} = \Delta G_c^{P \rightarrow M} + \Delta G_{nc}^{P \rightarrow M} + \Delta g^{P \rightarrow M} = 0 \quad (5.1)$$

Where  $\Delta G_c^{P \rightarrow M}$  is the chemical free energy change and  $\Delta G_{nc}^{P \rightarrow M}$  is the non-chemical (mainly stored elastic energy) free energy change.  $\Delta g^{P \rightarrow M}$  is the energy associated with the friction of the motion of P/M interface. In effect, it is the opposition to the formation of a small martensite plate or to the growth of an existing plate. Tong and Wayman [116] have discussed the effect of non-chemical free energy term on the martensitic transformation behaviour. In case of thermally induced martensitic transformation, the non-chemical free energy term  $\Delta G_{nc}^{P \rightarrow M}$  due to martensitic transformation is positive and it increases continuously with increasing amount of martensite. Also, the chemical free energy term  $\Delta G_c^{P \rightarrow M}$  is negative below  $T_0$  temperature. According to **equation 5.1**, the transformation to happen, the free energy change needed for the transformation ( $\Delta G_c^{P \rightarrow M} + \Delta G_{nc}^{P \rightarrow M}$ ) should override  $\Delta g^{P \rightarrow M}$ . This

indicate when  $\Delta G_{nc}^{P \rightarrow M}$  is small, chemical free energy needed  $\Delta G_c^{P \rightarrow M}$  is also small to satisfy the condition for transformation. In addition, **Figure 5.1** indicates when  $\Delta G_{nc}^{P \rightarrow M}$  is small transformation temperatures  $M_f$  and  $A_s$  comes closer to the  $M_s$  and  $A_f$  temperatures, respectively. This is precisely the case for ARS sample where a sharp forward and reverse transformation peak is seen in DSC profile due to smaller  $\Delta G_{nc}^{P \rightarrow M}$ .

### 5.2.2. Phase Transformation of Cold Rolled Samples As Determined by DSC

The ARS sample when plastically deformed using cold rolling to give various thickness reductions, the transformation temperatures change significantly compared to that of ARS sample. Up to 20 % reduction, the forward ( $B2 \rightarrow B19'$ ) and reverse transformation ( $B19' \rightarrow B2$ ) peaks are seen in DSC profile and beyond 30% rolling there is no transformation seen in the alloy. Another interesting point is that, even for 10CW and 20CW sample the transformation temperatures decreases and the hysteresis increases. Also, the reversible heat flow per unit mass decreases with increase in rolling reduction and at about 30 % thickness reduction the thermally induced transformations are completely suppressed. Beyond 30 % cold rolling the transformation temperatures are not seen in the DSC profile within the temperature range ( $-90^0$  to  $+90^0$ C). However, the transformation path in case of 10CW and 20CW sample was a single step transformation similar to ARS sample. There was no two-step and multi-step transformation seen in case of rolled samples. This transformation behaviour of the rolled samples can be explained using the thermodynamic aspects of the martensitic transformation as discussed in section 5.2.1.

After cold rolling, a large number of dislocations are introduced in the structure. There exists additional large contribution from strain energy due to the dislocations and grain boundaries, which means there is an increase in non-chemical free energy term,  $\Delta G_{nc}^{P \rightarrow M}$ . An increase in non-chemical free energy term  $\Delta G_{nc}^{P \rightarrow M}$  results in the balance of  $(\Delta G_c^{P \rightarrow M} + \Delta G_{nc}^{P \rightarrow M})$  with respect to  $\Delta g^{P \rightarrow M}$  at a lower temperature. Thus transformation temperatures  $M_f$  and  $A_s$  is shifted towards the left with respect to  $M_s$  and  $A_f$  temperatures. In turn, the strain field of the defects introduced during cold rolling suppress the martensitic transformation and results in an enhanced increase in the non-chemical energy term leading to spread out transformations in 10CW and 20CW sample. Whereas, with increase in rolling reduction beyond 30%, the transformation temperatures are lowered beyond  $-90^\circ\text{C}$  and that is why there is no transformation seen in 30CW, 50CW and 80CW sample in DSC.

### 5.2.3. Phase Transformation of ECAP Processed Samples As Determined by DSC

In case of ECAP samples, the transformation behaviour is completely different that rolled samples. During ECAP, the samples are plastically deformed in austenitic stage as was done during cold rolling, but the deformation temperature ( $450^\circ\text{C}$ ) was much higher than that of cold rolling. As it is mentioned in the experimental section, that the samples after ECAP was kept inside the die until the die comes to a room temperature. It takes approximately 2 hours to cool the die to room temperature from  $450^\circ\text{C}$  meaning after each pressing the samples were aged inside the die. The matrix of ARS sample is supersaturated with Ni as it was quenched from  $900^\circ\text{C}$  and the solubility of Ni at room temperature is 50.0 at.% (Refer **Figure 2.6**) - much lower than it is present in the as-received alloy. Because of this, precipitates form in the structure when the alloy is

aged after the solution treatment and the precipitation hardening takes place. The precipitates - not only their size and distribution but local composition change due to precipitation also affect the transformation behaviour greatly. From **Figure 2. 9**, it can be seen that a small decrease in the atomic percentage of Ni in the alloy increases the transformation temperature. The DSC result of the ECAP samples indicates that the transformation temperatures are much higher when compared to the transformation temperatures of ARS sample. The  $A_S$  and  $A_f$  temperature of ARS sample are  $-23\text{ }^{\circ}\text{C}$ ,  $6\text{ }^{\circ}\text{C}$  and that of 1st ECAP sample are  $24\text{ }^{\circ}\text{C}$ ,  $53\text{ }^{\circ}\text{C}$  as seen in **Figure 4.5**. This indirectly suggests that the precipitation in the matrix has taken place during the ageing of the samples inside the die resulting the decrease in Ni content in the matrix, which causes the increase in forward and reverse transformation temperatures. Consequently, the alloy became shape memory alloy at room temperature.

Having discussed the increase in transformation temperatures in the ECAP sample, we should now discuss the multistage transformation behaviour. The multistage transformation is a quite interesting phenomenon in some specific Ni rich TiNi alloys; the origin of which is not understood clearly and there are many explanations available in the literature. Allafi et al. [69] and Fan et al [117] give the most promising explanations. The former have proposed that the multi-stage transformation is due to the composition inhomogeneity in matrix B2 phase between  $\text{Ti}_3\text{Ni}_4$  particles and large-scale inhomogeneity between grain boundary and the interior of the grains. Such composition inhomogeneity is a result of the kinetics of precipitation formation in a supersaturated solid solution. This composition inhomogeneity between precipitate particles in TiNi alloys would create two  $B19' \rightarrow R$  transformation peaks and one subsequent

$R \rightarrow B2$  transformation peak. The former two peaks correspond to the transformation at low Ni region (near the precipitate) and high Ni region (away from precipitate). Fan et al [117] have explained this multistage transformation behaviour in terms of precipitation kinetics. They have suggested that based on the degree of supersaturation (the excess Ni concentration beyond solubility limit) in the alloy, the driving force for precipitation changes. Depending on the driving force, the nucleation barrier for precipitation changes from a very high value to almost zero value. The nucleation rate for precipitation formation thus changes with the supersaturation degree, which is given by the equation:

$$I \propto \exp(-\Delta G_c/kT) \quad (5.2)$$

Where,  $\Delta G_c$  is the nucleation barrier or the critical free energy to form a nucleus;  $k$  is the Boltzmann constant;  $T$  is the transformation temperature. The presence of grain boundary and dislocations also affect the nucleation rate. At low supersaturation, Fan et al. [117] have shown that the nucleation rate at grain boundary and at dislocations is significantly larger than that of grain interior. These findings can explain the multi stage transformation seen in DSC, which corresponds to the transformation at different location in the matrix. The grain boundaries undergo a two-step transformation and the grain interior which is precipitate free undergo a single-stage transformation thus in total a three-step or multi-step transformation is seen.

Now we should understand as why three-stage transformation is seen only after 2nd ECAP (refer **Figure 4.4**). From the previous discussion, it was argued that degree of supersaturation, presence of grain boundary and similar defects like dislocation is necessary to observe multistage-dislocation. It may be that after 1st ECAP the presence

of grain boundary and dislocations were not sufficient to cause a large scale inhomogeneity in the matrix to cause multistage transformation. After two passes in ECAP, the conditions may be ideal for a preferential nucleation of precipitates in grain boundaries and dislocations resulting heterogeneous distribution of precipitates in the matrix and that is why the multi-stage transformation behaviour. After that with increasing number of passes, because of dislocation cutting through the particles and small enough grain size, even a preferential precipitation at the grain boundary and at the dislocations results in an overall homogeneous distribution of the precipitates in the matrix preventing the multi-step transformation.

### **5.3. X-Ray Diffraction study of Cold Rolled and ECAP Samples**

X-ray diffraction study was done to find out the phases present after various processing conditions and supplement the findings from DSC. **Figure 4.6** shows the XRD profile for ARS sample and after 10, 20 50 and 80% cold rolling reduction. As can be seen from the XRD profile the ARS sample shows reflections only from (110), (200), (211) and (220) plane of B2 phase indicating that the structure is completely austenitic at room temperature. In case of 10CW and 20CW sample apart from  $(110)_{B2}$ ,  $(200)_{B2}$ , and  $(211)_{B2}$  reflections there were reflections from (111), (200) and (220) plane of B19' martensite. The  $(220)_{B2}$  reflections are not seen in these two samples which may be because of peak broadening due to reduction in grain sizes during cold rolling. The additional reflections from (111), (200) and (220) plane of B19' martensite indicate that the phase structure after 10% and 20% rolling reduction is a mixture of austenite and martensite. However, the DSC indicates that the transformation temperatures in 10CW and 20CW sample is much lower than room temperature ( $23^{\circ}\text{C}$ ) and the structure at room

temperature should be the high temperature phase i.e., austenite. At this point, one should keep in mind is that DSC records the transformation temperatures, which are induced in the alloy due to change in temperature. DSC does not give any information about stress induced martensite which is present at any temperature above  $A_f$ , the austenite finish temperature. Hence, based on DSC results any comment on the phases present in the alloy may be erroneous; phase identification must be done by XRD analysis, which indicates the presence of stress induced martensite in 10CW and 20CW sample. The XRD results indicate that a partial martensite stabilisation takes place when the residual stress level in the alloys is below certain limit.

The above discussion is also valid for the XRD profiles of 50CW and 80CW sample. These two samples show the reflection only from  $(110)_{B2}$ ,  $(200)_{B2}$ , and  $(211)_{B2}$  planes. Even though there is no transformation seen in 50CW and 80CW sample in DSC profile, the reasons for which was discussed in the section 5.2.2, these two samples show no sign for martensite stabilisation in the matrix as there is no reflections from planes corresponding to  $B19'$  martensite. There may be an argument raised that the reflections from  $B19'$  martensite phase is suppressed because of peak broadening. This argument may not be true as will be discussed when discussing the recovery behaviour of cold rolled samples in later section. However, one more question remain unanswered as why the partial stabilisation in the martensite is not seen in 50CW and 80CW sample. In other words, why the partial martensite stabilisation takes place below a certain residual stress limit and above that austenite stabilisation is seen.

In fact, the present observations are quite similar to the observations made by Nakayama et al. [67] and Karaman et al. [98]. Nakayama et al. have reported the presence



of B2 phase alone after 70% cold rolling reduction of Ti 50.2at.% Ni, whereas martensite stabilisation was expected. Karaman et al. also have reported austenite stabilisation in room temperature SPD of Ti 50.8at.% Ni. The possible explanation for this unusual austenite stabilisation is that in case of 10CW and 20CW sample, stress induced martensite (SIM) forms and then in some area because of the high stress localisation martensite stabilises in the matrix. However, when the alloy is deformed further, in case of 50CW and 80CW sample, initially SIM forms in the matrix and then it is back transformed into B2 phase as first proposed by Tyumentsev et al.[118] in case of TiNi(Fe, Mo) alloy. Then Karaman et al. [98] (as shown in **Figure 5.2**) proposed similar mechanism in case of Ni rich TiNi alloys deformed at room temperature in austenitic phase. This new deformation twinning mechanism is based on forward plus back-transformation ( $B2 \rightarrow B19' \rightarrow B2$ ) with the back-transformation taking place in an alternative transformation system. The forward transformation occurs due to the austenite instability under an externally applied stress field and martensite exists only in high local stress areas. After that, back transformation through another system, that is, deformation twins occurs to relax the local stress.

In case of ECAP samples, as shown in **Figure 4.8** the reflections from  $(002)_{B19'}$ ,  $(111)_{B19'}$ ,  $(121)_{B19'}$ , and  $(\bar{2}12)_{B19'}$  plane of B19' martensite are in all ECAP samples. There were also reflections from  $(121)_R$  and  $(322)_R$  plane of R phase. These reflections indicate that the structure is a mixture of both B19' and R phase. DSC results also shows that at room temperature (23 °C) the structure is two-phase structure as seen in **Figure 4.5**. In ECAP processed samples, the back transformation to austenite does not happen unlike in cold rolled samples. This is because the transformation in ECAP processed

samples is controlled by the compositional change and the microstructure. In addition, the formed martensite after 1st ECAP is stable at room temperature due to the possible compositional variation after ECAP processing.

Even though there are no direct observations made by TEM analysis after cold rolling and ECAP, the XRD analysis indicates huge reduction of grain size in both cold rolled samples and sample after ECAP. For 50CW and 80CW sample only  $(110)_{B2}$  peak is seen and all other peaks which were available in ARS, 10CW and 20CW are not available, as shown in **Figure 4.6**. From **Figure 4.7** and **4.9**, continuous increase in FWHM of  $(110)_{B2}$  peak in rolled samples and  $(111)_{B19'}$  peak in ECAP samples, respectively indicates significant reduction in grain size in the alloy. In addition, the previous work in the literature related to cold rolling [65-68] and ECAP [90-96] of TiNi alloys report a grain size in the range of 50-200 nm. Based on these references and the XRD results, it can be inferred that at room temperature, in case of 80CW alloy the structure is fine nano-grain of B2 austenite and in ECAP samples, the structure is fine nano-grains of martensite.

#### **5.4. Pseudoelasticity of Cold Rolled Samples**

The various indentation and scratch testing on the cold rolled samples have shown the effect of cold rolling and thus reduction of grain sizes on pseudoelasticity of Ti 50.8at.% Ni. The results of conical and Berkovich indentations shown in **Figure 4.14** and **Figure 4.11** respectively, indicate that 80CW sample has the maximum depth recovery ratio. Even though the recovery was not complete in both conical and Berkovich indentations, the 80CW sample showed maximum recovery consistently in both type of indentations. This incomplete recovery can be rationalised using the concept of

representative strain. In case of the conical indentations, the indenters used produce spherical indentation at low loads. Using Oliver and Pharr method [23,24] the contact radius at peak load during indentation was estimated and then the representative strain under the indenter was calculated using the equation 4.1 and is shown in the **Table 5.1** below:

**Table 5.1.** Estimated contact radius and representative strain under the conical indenter with 107  $\mu\text{m}$  tip radius for ARS and various cold rolled samples during PMC up to 2500 mN. Data shown is only for the 5th indentation cycle with peak load of 2500 mN

Sample	Contact radius, $a$ ( $\mu\text{m}$ )	Representative strain, $\epsilon_r$
ARS	$28.1 \pm 3.3$	$0.053 \pm 0.006$
10CW	$26.1 \pm 5.0$	$0.049 \pm 0.009$
20CW	$29.8 \pm 2.2$	$0.056 \pm 0.004$
50CW	$24.7 \pm 1.8$	$0.046 \pm 0.003$
80CW	$22.7 \pm 1.9$	$0.042 \pm 0.004$

From the **Table 5.1**, it can be seen that the representative strain under the indenter is varying greatly in different sample. However, in 80CW sample the representative strain is the lowest. The pseudoelastic effect under uniaxial tension or compression exists up to a recoverable strain of 0.08. The 80CW sample has the minimum representative strain among all the samples. Thus, the recovery ratio is maximum for this sample. Whereas, in case of 10CW and 20CW sample, the representative strain is larger than 50CW and 80CW sample. This is obvious because the microstructure in 10CW and 20CW sample contains both austenite and martensite phase as confirmed by XRD. The martensite being a soft phase the penetration is larger in a mixture of both phases, as in case of 10 and

20CW sample than it is only in austenite phase, as in case of 50CW and 80CW sample. There is another reason why the pseudoelastic recovery is incomplete in these samples even though the representative strain under the indenter is well below the maximum limit of recoverable strain in case of uniaxial tension or compression. The pseudoelastic recovery heavily depends on the local strain gradient in the alloys during deformation. The tip radius of the indenter and the geometry of the indenter play an important role in generating the strain under the indenter during indentation. We shall discuss this in more detail in later part of our discussion (see section 5.5).

However, in case of Berkovich indentations the depth recovery ratio lies between 0.3 to 0.4 and beyond 1000 mN load there is not much variation in the depth recovery ratio, even though 80CW sample shows the maximum recovery. The representative strain during Berkovich indentation in elastic-plastic solid is approximately 0.08 [115]. This strain is much higher than the representative strain generated during conical indentation. Hence, such lower recovery is natural in Berkovich indentations. Another important difference between spherical and pyramidal indentation could be the magnitude and the spatial distribution of stress and strain in the localised region beneath the indenter.

Similar pseudoelastic recovery behaviour to that of indentation loading is observed in case of scratch loading of cold rolled samples, even though the deformation gradient in scratch loading is more severe than the indentation loading. The reason for higher maximum scratch depth and lower recovery for 10CW and 20CW sample is that the deformation is done in a mixture of austenite and martensite. Since the cold rolled samples or the martensite in 10CW and 20CW sample are not aged, pseudoelasticity is not expected from the martensite in these two samples. The deformation in these two

samples is more of deformation of austenite and martensite where part of the austenite deformation is recovered due to pseudoelasticity and the deformation in martensite is more of martensite reorientation followed by yielding. Hence, both the scratch depth and the recovery is less. Whereas, in case of 50CW and 80CW sample the structure consists of austenite as seen in DSC (**Figure 4.3**) and confirmed by XRD (**Figure 4.6**). The deformation done during indentation and scratch loading in these two samples consists of deformation of austenite. Hence, the deformation done is recoverable as long as the strain generated during deformation does not cause plastic yielding of the material beneath the indenter. Another consideration to be made while discussing the scratch testing result is that the indenter used for static indentation had a tip radius of 107  $\mu\text{m}$  and that for scratch testing had a tip radius of 269  $\mu\text{m}$ . While it is difficult to estimate the strain generated under the indenter during scratch testing, it is possible that the strain generated under the indenter in case of a static loading by the indenter having larger tip radius is smaller compared to that by the indenter having smaller tip radius. In addition, the spatial stress and strain distribution in case of an indenter with smaller tip radius could be higher. However, keeping the indenter radius constant, it is shown in the present study that the recovery ratio increases with increase in cold rolling in both indentation and scratch deformation. The key point to achieve the complete recovery is prevention of plastic yielding of the material below the indenter.

To support the above discussion and to see the effect of larger indentation loading simple indentation cycles were performed on ARS sample and 80CW sample at 1N, 10N and 20N with a conical indenter having a tip radius of 107  $\mu\text{m}$ . The depth recovery ratio was calculated from load-displacement curve and representative strain was estimated as

described in the earlier sections. **Figure 5.3** shows the result of such indentations on ARS and 80CW sample. It is seen from **Figure 5.3** that the depth recovery in 80CW is much higher especially at higher loads. However, the complete recovery is not seen even at very low representative strain. The reason for low recovery ratio even at lower indentation loads and lower representative strain could be attributed to the geometry of the indenter. Even though the indenter is a conical indenter with spherical tip, the tip radius (107  $\mu\text{m}$ ) is much smaller than the sphero-conical indenter, which had a tip radius of 200  $\mu\text{m}$ . In this sense, the conical indenter with 107  $\mu\text{m}$  tip radius is much sharper and the strain gradient in some localised region under the indenter might be reaching the maximum limit of recoverable strain in case of uniaxial tension or compression. This will result in deformation by slip rather than stress induced transformation.

In this section, we have discussed the reason for incomplete depth recovery under indentation loading for conical and Berkovich indentation in ARS and various cold rolled Ti 50.8at.% Ni samples. The pseudoelastic depth recovery behaviour of various cold rolled sample under scratch loading is also discussed. Now, it is important to understand why the 80CW sample shows the highest depth recovery in indentation and scratch loading. We shall discuss that based on the hardness measurement using Berkovich indentations of cold rolled samples in the following two sections.

#### **5.4.1. Mechanical Properties of Cold Rolled Samples**

The hardness measured using indentation technique in case of TiNi alloys is a function of the phases present in the alloy, inhomogeneity in the microstructure, amount of strain applied during indentation resulting volume percentage of martensite formed and amount of pile-up and sink-in. The hardness measured using the conical indentation

at 500 mN and 2500 mN is shown in the **Figure 4.10(a)**. Since the hardness is measured using Berkovich indenter, the strain at all indentation load is same. In that case, the variation in hardness at different loads should be a result of inhomogeneity in the material. The hardness is increased with the increasing amount of rolling deformation. The lower hardness for 10CW and 20CW sample at 2500 mN is because the indentation is done in a mixture of austenite and martensite and the martensite being soft, it resulted in lower hardness. Whereas, at lower load since the indentation depth is much lower the 10CW and 20CW sample show a large variation in the hardness. When the load is increased to 2500 mN, the indentation depth increases and the hardness value is more representative of that of the bulk sample. Thus, the measured hardness is more consistent. Another important factor that results in large variation in the hardness measured by instrumented indentation is the amount of pile-up and sink-in during indentation. In case of pile-up, the Oliver and Pharr method results in decreased accuracy because of overestimation of the contact depth. However, followed by Hall-Petch relation [70], as the grain size reduces the hardness of the material should increase and that is what is seen in **Figure 4.10(a)**. 80CW sample has the highest hardness and that is why it is difficult to penetrate this sample, which results in lower representative strain under the scratch and indentation loading. Consequently this sample shows the maximum recovery in both type of loading.

Similarly, the Young's modulus measured by indentation technique depends on a number of parameters, especially when there is a phase transition during indentation the measurement becomes even more difficult. One important consideration in measuring the Young's modulus using indentation techniques is when there is phase transition from

austenite to martensite, depending on the volume percentage of martensite transformed, the Young's modulus value should decrease; the value would still depend on the accuracy of the unloading slope,  $S$ . However, the Young's modulus values reported in **Figure 4.10(b)** does not follow any particular trend and any comment without estimating the volume percentage of transformed martensite should be erroneous.

#### **5.4.2. On the Stress-Strain Diagram of Cold Rolled Samples**

During spherical indentation, the representative strain under the indenter increases continuously with the contact depth, as the applied load increases. An attempt is made to generate stress-strain diagram and the yield point of the cold rolled samples using spherical indentation. Only three different samples with three different microstructure was used for this study – ARS sample which has only austenite phase, 10CW sample which has some residual SIM in the austenite phase and 80CW sample which has only austenite phase but with much lower grain size compared to ARS sample. The result of such an attempt is shown in **Figure 4.12**. However, the data in the y-axis is the measured hardness from the indentation experiments but not the stress because Tabor's observation [119] of  $\sigma_{indentation} \approx H/3 \approx \sigma_{uniaxialtension}$  may not be true for shape memory alloys. While it is difficult to estimate the yield strength of the samples from the indentation induced load-displacement curve, **Figure 4.12** infers that the 80CW sample has higher yield strength than other two samples. The higher strength helps in inducing SIM transformation even to higher loads without initiating the plastic yield of the austenite resulting higher recover under indentation and scratch loading.

From the first set of PMC indentation in **Figure 4.12**, the depth recovery ratio for all three samples was calculated and the result is shown in **Figure 5.4**. The depth



recovery ratio from the second set of PMC indentations was not calculated because the unloading during each indentation cycle was done up to 50% of the maximum load of the corresponding cycle. The result again shows that not only 80CW sample has the highest recovery but also has the maximum recovery up to a higher load. This is an indirect evidence for the fact that 80CW sample has the higher yield strength in austenitic phase, which delays the onset of plastic yield and shows SIM transformation and back transformation upon loading and unloading, respectively up to a higher load compared to other samples. The **Figure 5.4** also supports the fact that tip radius of a similar type of indenter has a big role in introducing the amount of plastic strain under the indenter. For the same 1N indentation load, the recovery ratio for ARS and 80CW sample with the indenter having 107  $\mu\text{m}$  tip radius is 0.78 and 0.79, respectively. Whereas, the recovery ratios with indenter having 200  $\mu\text{m}$  tip radius is 0.75 and 0.93, respectively. Indirectly this implies that the higher the radius of a spherical and/or conical indenter, the lower is the strain gradient under the indenter introducing plastic strain in the material, resulting higher recovery.

### **5.5. Shape Memory and Pseudoelasticity of ECAP Samples**

As indicated by the DSC (**Figure 4.5**) and XRD (**Figure 4.8**) results, the ARS pseudoelastic alloy at room temperature became a shape memory alloy at room temperature after the ECAP process due to the increase in forward and reverse martensitic transformation temperatures. This helped to study the effect of reduction in grain size on PE and SM behaviour of Ti 50.8at.% Ni alloy using indentation and scratch testing. **Figure 4.16** shows the indentation induced shape memory effect in this particular alloy after different number of ECAP passes. For each indents in 1st ECAP, 2nd ECAP,

3rd ECAP and 4th ECAP sample the contact radius,  $a$ , was estimated by Oliver and Pharr method [23,24] and representative strain,  $\epsilon_r$ , was then calculated using equation 4.1. PE recovery and SM recovery in each sample for all the indents are also calculated and is given in **Table 5.2**. From this table it can be seen that the SM recovery ratio of all samples is 1.0 up to 10 N and even at 20 N, the SM recovery ratio is varying between 0.84 to 0.88, which is very high when compared to the PE recovery of cold rolled samples. The representative strain at 20 N varies from 0.059 to 0.066. The representative strain and shape memory recovery in all the samples are higher than the values reported in a similar experiments conducted by Ni et al. [19] for a TiNi alloy with similar composition but with a slightly different transformation temperatures. In addition, Ni et al. used an indenter with 213.4  $\mu\text{m}$  tip radius, which will produce lower plastic strain than the indenter with 200  $\mu\text{m}$  tip radius.

The pseudoelastic recovery behaviour of the ARS alloy was studied using indentation and scratch loading and was compared with that of ECAP processed samples. **Figure 4.15(a)** and **(b)** shows the indentation induced pseudoelastic recovery for ECAP samples. The result shows that with increasing equivalent strain applied during ECAP the material shows better pseudoelastic recovery. In addition, the decrease in PE depth recovery with increasing indentation load is much lower in case of 4th ECAP sample than the other samples. This can again be rationalised using the concept of representative strain. The representative strain was calculated for all the indents and is plotted on top of **Figure 4.15(a)** and the result is shown in **Figure 5.5**. In **Figure 5.5 (a)**, **(b)** and **(c)** the DRR and representative strain is plotted at 5 N, 10 N and 20 N indentation load, respectively.

**Table 5.2. Calculated contact radius, equivalent strain and measured PE recovery and SME recovery of Ti 50.8at.% Ni alloy after different ECAP passes.**

	<b>Indentation load (N)</b>	<b>0.5</b>	<b>1</b>	<b>5</b>	<b>10</b>	<b>20</b>
<b>1st ECAP, Equivalent strain=0.64</b>	<b>Contact radius, <math>\mu\text{m}</math></b>	18.3	24.5	41.3	53.9	66.4
	<b>Representative strain</b>	0.018	0.024	0.041	0.054	0.066
	<b>PE recovery</b>	0.31	0.34	0.53	0.50	0.56
	<b>SM recovery</b>	1.0	1.0	1.0	1.0	0.88
<b>2nd ECAP, Equivalent strain=1.27</b>	<b>Contact radius, <math>\mu\text{m}</math></b>	15.5	21.5	38.5	49.2	58.5
	<b>Representative strain</b>	0.015	0.021	0.038	0.049	0.059
	<b>PE recovery</b>	0.63	0.62	0.78	0.54	0.69
	<b>SM recovery</b>	1.0	1.0	1.0	1.0	0.84
<b>3rd ECAP, Equivalent strain=1.90</b>	<b>Contact radius, <math>\mu\text{m}</math></b>	15.7	21.1	37.3	48.1	61.3
	<b>Representative strain</b>	0.016	0.021	0.037	0.048	0.061
	<b>PE recovery</b>	0.61	0.56	0.60	0.60	0.58
	<b>SM recovery</b>	1.0	1.0	1.0	1.0	0.86
<b>4th ECAP, Equivalent strain=2.54</b>	<b>Contact radius, <math>\mu\text{m}</math></b>	16.5	23.4	40.5	49.9	64.8
	<b>Representative strain</b>	0.016	0.023	0.041	0.050	0.065
	<b>PE recovery</b>	0.64	0.50	0.59	0.57	0.53
	<b>SM recovery</b>	1.0	1.0	1.0	1.0	0.87

It is seen from the **Figure 5.5**, the representative strain varies greatly in different samples; in fact, the representative strain decreases with increasing number of passes during ECAP. The higher recovery in 4th ECAP sample is because of the lower representative strain under the indenter. The important question, which needs to be addressed, is why the representative strain decreases as the equivalent strain increases

during ECAP. Interestingly, the nano-hardness of ECAP samples as shown in **Figure 4.13** is decreasing with increasing the equivalent strain during ECAP. Based on the hardness values of the ECAP sample, the indentation depth thus the contact depth and the representative strain in the ECAP samples should increase as the number of pass in ECAP increases. However, one should keep in mind that the hardness values reported in **Figure 4.13** is for the martensite phase at room temperature and the results reported in **Figure 5.5** correspond to the indentation in austenite phase at 75 °C. We shall discuss more on the deformation characteristics in these two phases when we discuss the results of the scratch testing done in ECAP samples as those results also indicate similar behaviour.

The scratch testing done on ECAP samples at 75 °C (**Figure 4.22**) also shows that with increasing equivalent strain in the samples, the maximum scratch depth decreases; even though there is not much difference in residual scratch depth with increasing equivalent strain in the samples. The reason for the small difference in residual depths is that the scratch testing was done in progressive loading mode with load increasing 0.1 N to 10 N and at 10 N the representative strain in all ECAP samples during indentation varies between 0.033 to 0.039 as seen in **Figure 5.5**. Even though the representative strain under the indenter during scratch loading might be different from indentation loading and it is difficult to estimate the representative strain under the indenter during scratch loading, it is safe to say that at 10 N there was not much plastic deformation introduced under the indenter while doing the scratch. However, from **Figure 4.22** and **4.23**, it is seen that 1st ECAP sample has the highest scratch depth and residual scratch depth whereas, the 4th ECAP sample has the lowest scratch depth and residual scratch

depth. Qian et al. [113] has done a study recently, which shows that the hardness and the transformation stress in TiNi alloys increase with temperature. In addition, the yield strength of metal and metallic alloys shows an inverse relationship with the temperature. This means that at higher temperature to arrest the plastic deformation and to promote the stress induced martensitic transformation the hardness and yield strength of the material has to be increased. This is what is happening in case of ECAP samples. The difference in 1st ECAP and 4th ECAP sample is the amount of deformation introduced in ECAP and the 4th ECAP sample should have the higher hardness and yield strength at 75 °C. The higher hardness and yield strength results in lower depth during indentation and scratch loading, thus even at higher load, stress induced martensitic transformation is initiated without going into the austenitic yield region and most of the strain introduced in the material is within the limit of recoverable strain in the alloy. Hence, as the strength of the alloy is increased by reducing the grain size using the severe plastic deformation (SPD) technique, at any given temperature, the load up to which pseudoelasticity is seen is increased. Therefore, SPD technique is a very useful technique to improve the pseudoelastic and shape memory behaviour of shape memory alloys.

To summarise this section we have discussed both indentation, scratch induced shape memory, and pseudoelastic behaviour for ECAP processed samples. Up to 10 N loads during indentation all the samples show complete shape memory behaviour, whereas, during scratch some residual deformation at 10 N is seen. In addition, at 20 N load during indentation, the shape memory recovery ratio varies between 0.84 to 0.88. Whereas, the pseudoelastic depth recovery is complete for 3rd and 4th ECAP sample at 5N indentation load. However, the DRR is highest (0.95) for 4th ECAP sample even at

20 N load and this DRR is very high when compared to other samples at the same load. This improvement in pseudoelastic and shape memory recovery is rationalised using the concept of representative strain and higher strength in the material due to reduction in grain size followed by ECAP.

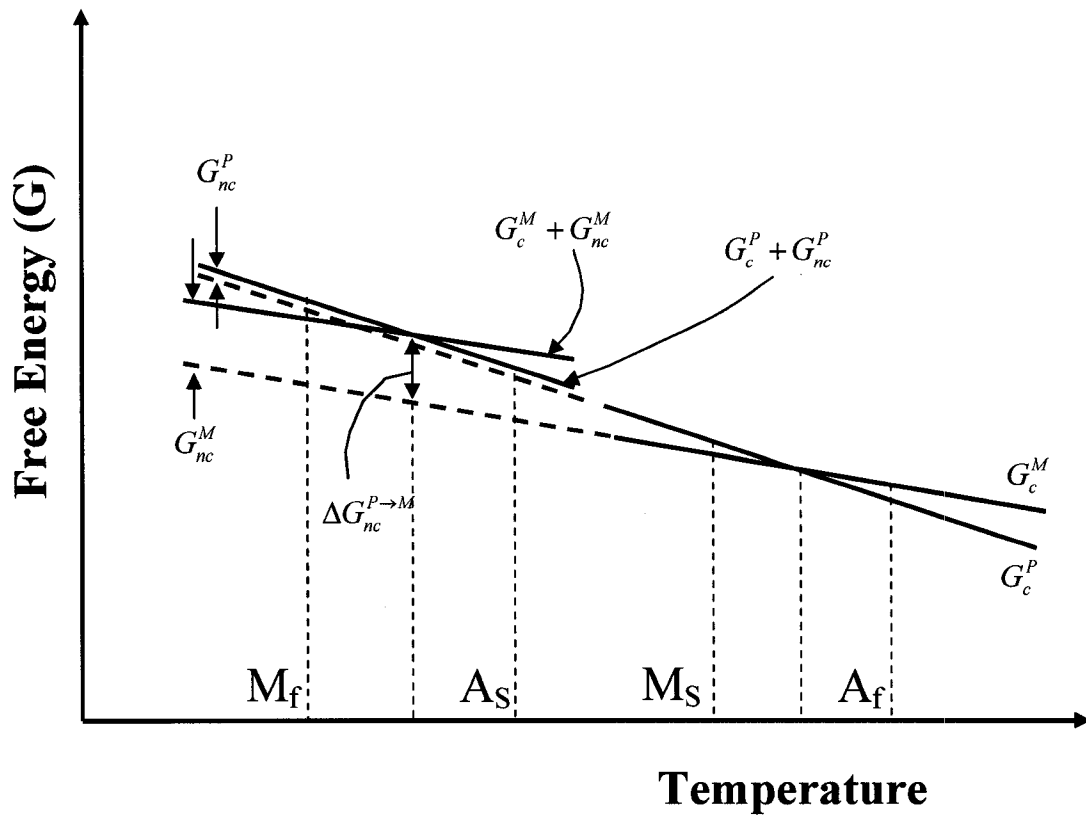


Figure 5.1. Schematic free energy diagram showing the effect of increasing non-chemical free energy contribution to transformation temperatures.  $G_c^P$ , is the chemical free energy for parent phase;  $G_c^M$ , is the chemical free energy in martensite phase. In all other terms subscript 'nc' represents nonchemical free energy of corresponding phase;  $\Delta G_{nc}^{P \rightarrow M}$ , is the change in nonchemical free energy associated with parent to martensite transformation.

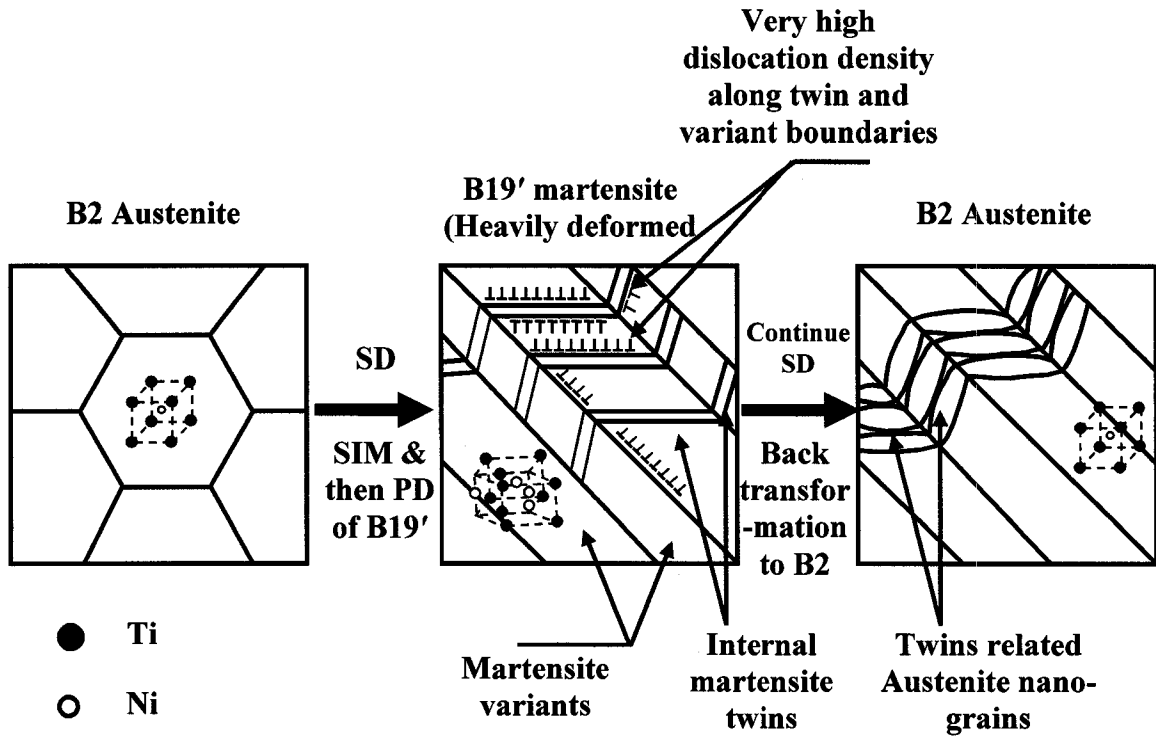


Figure 5.2. Schematic of the mechanism for deformation twin formation in B2 austenite during cold rolling of Ti 50.8at.% Ni above  $A_1$  temperature via the  $B2 \rightarrow B19' \rightarrow B2$  transformation sequence.



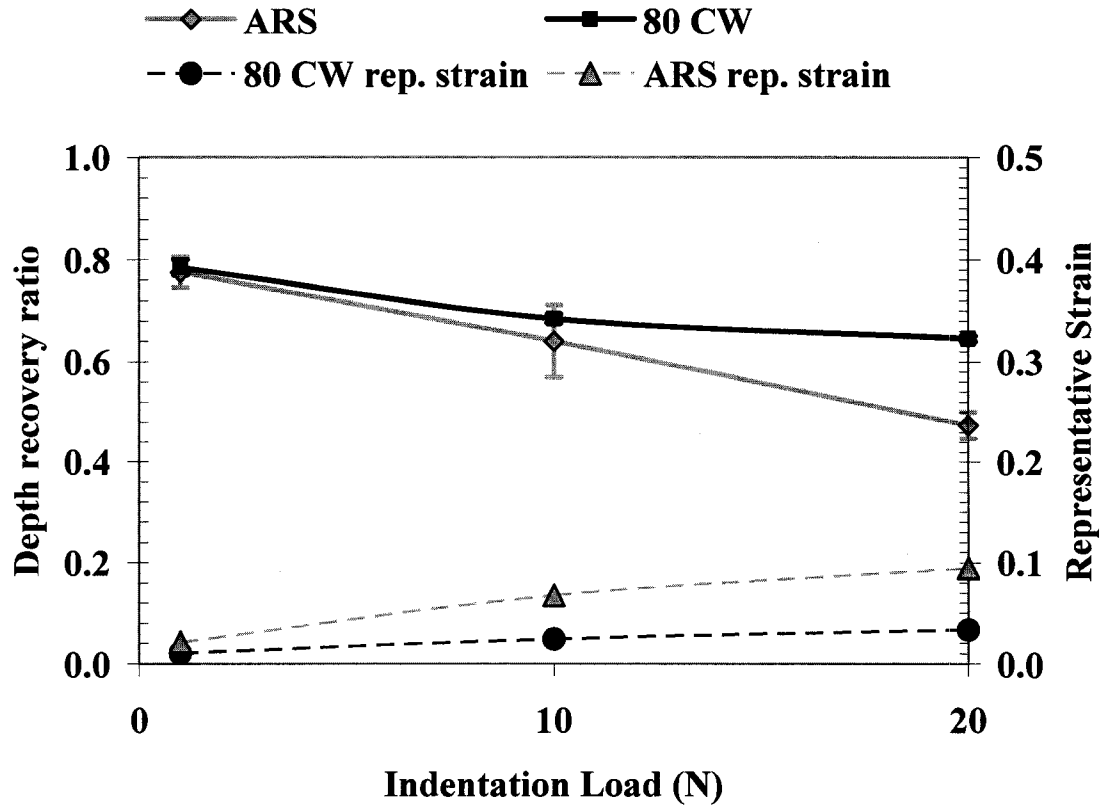


Figure 5.3. The depth recovery ration and the representative strain for ARS and 80CW sample during a simple indentation using a conical indenter having 107  $\mu\text{m}$  tip radius at three different indentation loads. The numbers in the boxes are the representative strain applied during the indentation.

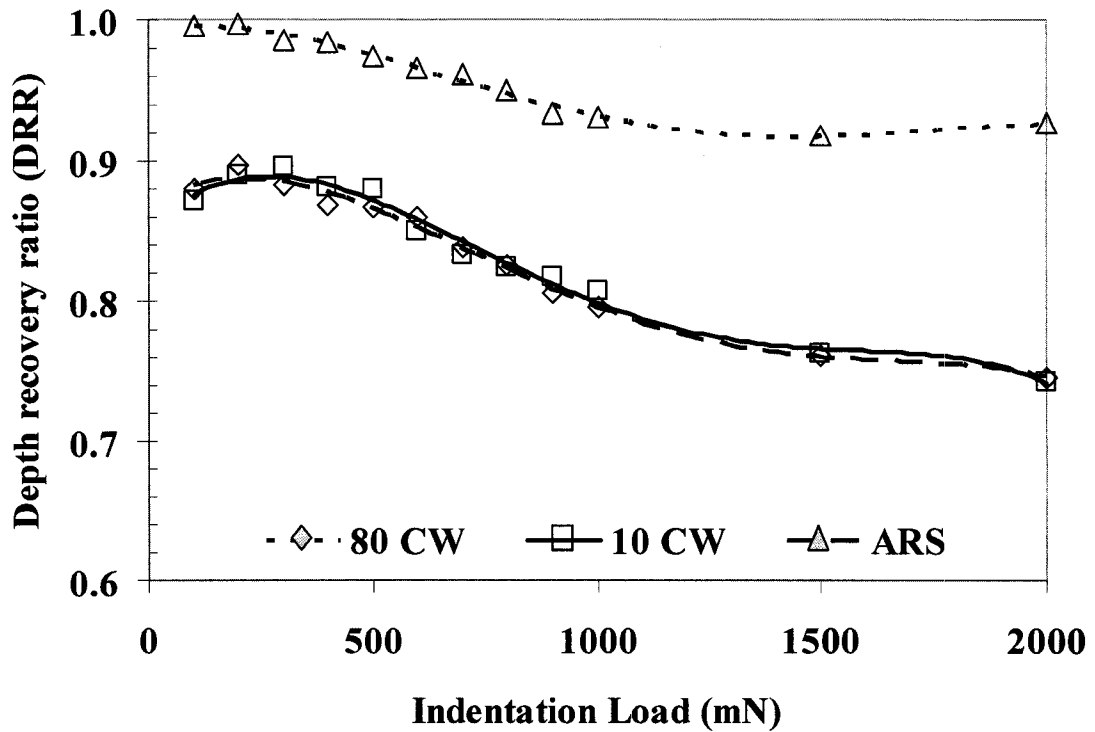
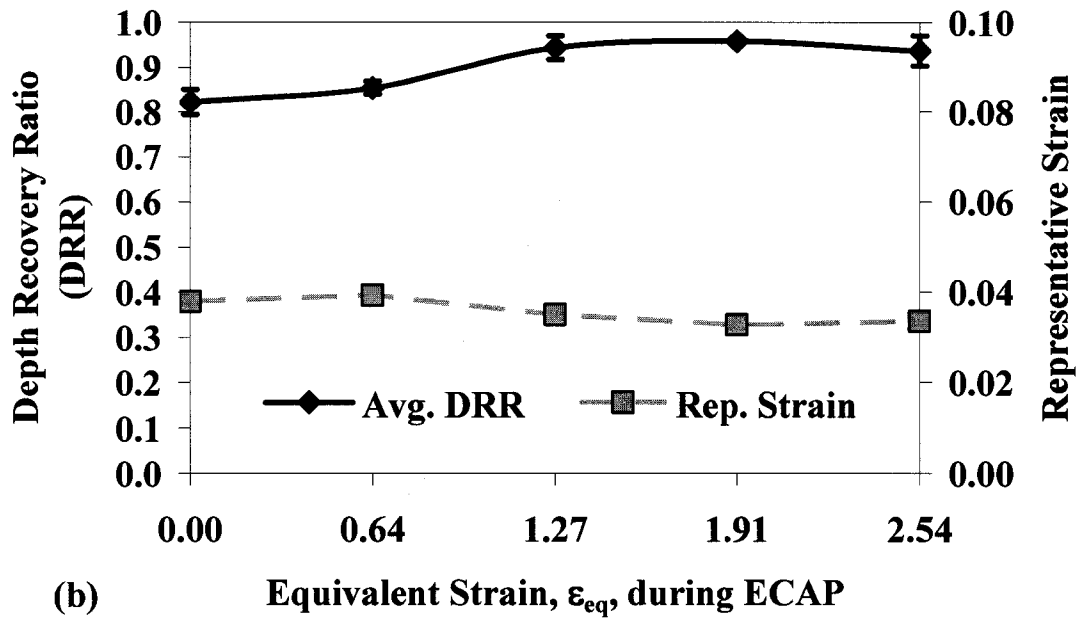
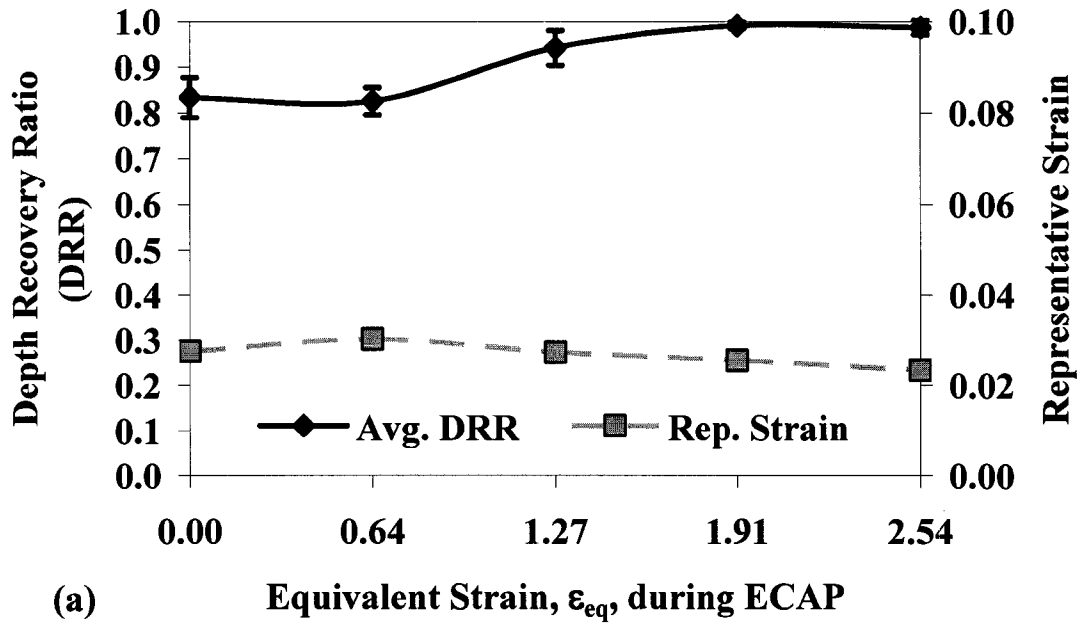


Figure 5.4. Calculated depth recovery ratio for ARS, 10CW and 80CW sample from the result shown in Figure 4.12. Only the first set of indentations were used for the calculation.



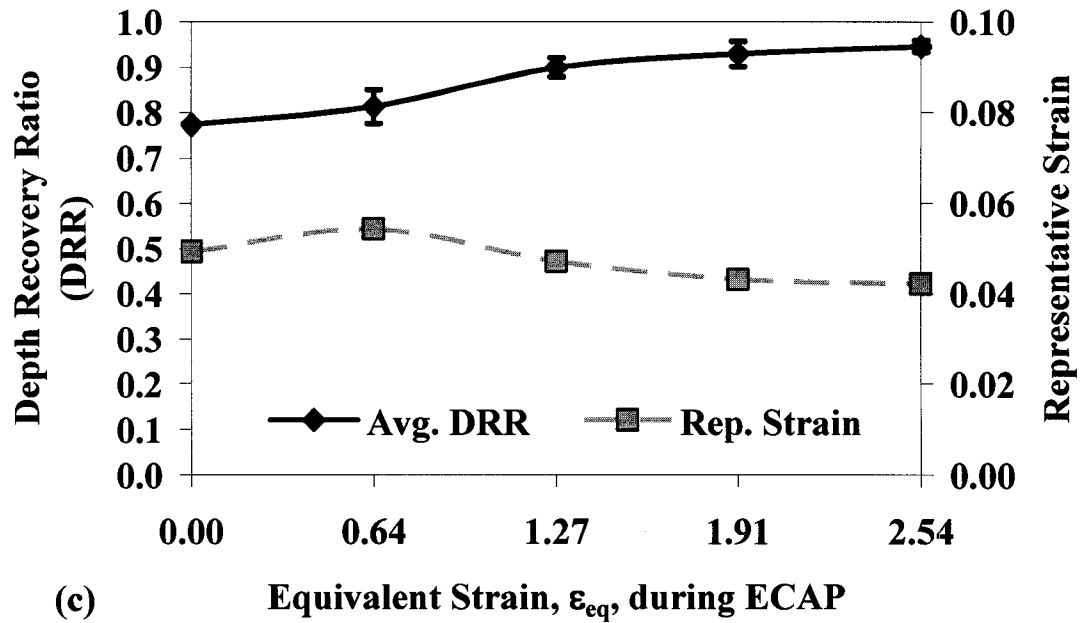


Figure 5.5. Pseudoelastic depth recovery ratio and representative strain of ARS sample measured at room temperature and ECAP samples measured at three different loads at 75 °C using a spherical indenter with 200  $\mu\text{m}$  tip radius; (a) at Indentation load 5N (b) at 10 N and (c) at 20 N.

## CHAPTER 6

### 6.1. Summary and Conclusions

The aim of this study was to subject TiNi alloy to severe deformation such that yield strength of the alloy is increased. This increase in yield strength should enable the alloy to undergo stress induced martensitic transformation prior to austenite yielding so that the deformation introduced in the material is recovered once the load is removed resulting a self-healing bulk material by taking advantage of increased range of pseudoelasticity.. To achieve this, Ti 50.8at.% Ni alloy was deformed using cold rolling to give a thickness reduction of 80% and using equal channel angular pressing technique to give a total equivalent strain up to 2.54. The martensitic transformation behaviour and phases present in the alloy were studied using differential scanning calorimeter and X-ray diffraction analysis. The deformed alloy was subjected to instrumented indentation and scratch loading under different loading and at two different temperatures (23 °C and 75 °C). The depth recovery ratio under indentation load was calculated and the deformed scratch surface was measured using 3D optical profilometer. Based on the work carried out, the following conclusions can be drawn:

1. Cold working suppresses the transformation temperatures of binary Ti 50.8at.% Ni alloys to beyond -90 °C. Up to 30% cold rolling reduction in thickness results in broadening of the transformation temperatures and beyond 30% reduction in thickness stabilise the austenite phase in the alloy.

2. Cold working up to 30% reduction in thickness results in partial stabilisation of martensite phase in localised region of the high temperature austenite phase in the alloy. Deformation beyond 30% rolling stabilises the austenite phase in the alloy.
3. From the measured peak width at half maximum of  $(110)_{B2}$  peak in cold rolled sample and by taking reference from the similar work carried out reported in the literature, it can be inferred that the 80% cold rolled sample had the lowest grain size which should be nanocrystalline.
4. Pseudoelastic recovery is dependent on the mode of deformation and the strain applied during the deformation. Berkovich indentation where the strain gradient is much higher than the spherical indentation results in much lower pseudoelastic recovery in the alloy. The actual strain gradient under the indenter during indentation and scratch loading depends on the tip radius of a spherical and conical indenter. Higher the tip radius, lower is the plastic strain introduced under the indenter resulting higher PE recovery.
5. After cold rolling the 80CW sample shows the highest recovery for the load ranges used during indentation (100 mN to 20 N) and scratch loading (0.1 N to 10 N) which is due to increase in yield strength of the austenite phase after large amount of deformation. The increase in yield strength helps in delaying the onset of plastic yielding in austenite phase and introducing SIM transformation and back transformation up on loading and unloading respectively.
6. Scratch testing also reveals similar results to that of spherical indentation. Even though the loading conditions in scratch testing are more severe than the indentation loading, the 80% cold rolled TiNi alloy had the maximum scratch

recovery, which was completely pseudoelastic. Besides, the amount of pile-up is also less in 80CW sample, which will be advantageous in case of repetitive sliding contact systems. It is important to understand that using the property of pseudoelasticity complete self-healing in TiNi is possible only if the strain introduced in the material during deformation does not result in plastic yielding of austenite. However, in real contact system achieving this condition is an optimistic desire.

7. High temperature severe plastic deformation using equal channel angular pressing has substantial effect on the transformation behaviour. Ti 50.8at.% Ni alloy which was pseudoelastic at room temperature acquired shape memory characteristics after ECAP at 450 °C. From the DSC and XRD results it can be concluded that after ECAP at 450 °C, the alloy was a mixture of low temperature phases, namely B19' and R phase.
8. Even though the deformation during ECAP was done in austenitic phase, the transformation temperatures has increased after the first pass of ECAP and thereafter, remained almost constant unlike cold rolled sample where the transformation temperatures decreases. This contradicting behaviour is possibly due to the ageing effect after ECAP pass resulting the micro-scale inhomogeneity in the alloy, which was not a case in cold rolling.
9. Multistage transformation peaks are observed after 2nd pass of ECAP, however, again after 3rd pass of ECAP two stage transformation is seen. In addition, R phase transformation is seen in all ECAP samples.

10. While after ECAP, the alloy after all processing condition showed approximately 6 % shape memory strain recovery under 10 N indentation load, the pseudoelastic recovery varied greatly with the load applied during indentation and with the amount of plastic deformation introduced resulting grain refinement. At 10 N load, the pseudoelastic recovery in all the ECAP samples varied from 0.85 to 0.96 and not showing a complete self-healing unlike shape memory strain recovery.
11. The scratch testing after different ECAP passes showed similar results unlike the indentation results after ECAP. However, the 4th ECAP sample showed lower scratch depth and residual scratch depth after unloading, complete recovery is not seen.

Thus, on a concluding note, achieving self-healing using pseudoelasticity of TiNi alloys may be possible under controlled deformation where the actual strain applied is of known magnitude and can be controlled while deformation. In addition, achieve self-healing using shape memory ability appears to be more appealing at this point. However, one should again keep in mind that there is a limit up to which the strain can be recovered in both pseudoelasticity and shape memory behaviour. For complete recovery, it is also important to avoid strain accumulation in the materials during repetitive loading condition, which result in crossing the critical strain recovery limit and in such case plastic deformation can not be avoided. The strain accumulation is more predominant in case of shape memory behaviour as the deformation is done in martensite and unless it is heated above the austenite finish temperature or a special heat treatment is given as in case of rubber-like-behaviour (RLB) the martensite does not show self-healing property.

In this study, possibly for the first time the following are shown:



1. Bulk surface with self-healing or damage recovery property can be achieved using pseudoelastic property of Ti 50.8at.% Ni alloy. The amount of damage recovery significantly depends on the applied load and the geometry of the indenting surface.
2. The self-healing using pseudoelastic property is a more appropriate choice than self-healing using shape memory property even though the later shows complete recovery. This is because self-healing using shape memory property demands that the surface needs to be heated and cooled which may not be practical in all applications. In addition, the damage in martensite phase is accumulative which might cause the plastic yielding of the phase preventing the self-healing in repetitive or cyclic loading conditions..

## **6.2. Suggestions for Future Work**

- Study the indentation and scratch induced recovery after deforming the sample using ECAP at room temperature. Because at room temperature deformation, the microstructure control will be lot easier and better control on transformation temperature can be achieved by controlled heat treatment after ECAP deformation. Then follow up the work by Transmission Electron Microscope (TEM) and Focused Ion Beam (FIB) techniques.
- While the pseudoelastic elastic recovery heavily depends on the strain gradient under the contact surface, it will be a great idea to study the strain gradient formation using numerical simulation beneath the contact surface. This along with

experimental study will be useful to understand how the controlled deformation can be used to achieve complete self-healing.

- Another interesting study will be to start with shape memory alloy and deform the shape memory alloy using cold rolling and/ or severe plastic deformation technique, thereby, avoiding the uncertainty during control of martensitic transformation temperatures and microstructures during heat treatment as these affect the shape memory recovery and pseudoelastic recovery. Then follow up the work by Transmission Electron Microscope (TEM) and Focused Ion Beam (FIB) techniques.

## List of References

- [1] Basinski, Z. S.; Christian, J. W. *Acta Metallurgica* **1954**, *2*, 101-116.
- [2] Worden, K.; Bullough, W. A.; Haywood, J., Eds.; In *Smart Technologies*; World Scientific: Singapore, 2003; pp 109-135.
- [3] Buehler, W. J.; Wiley, R. C. *ASM – Transactions* **1962**, *55*, 269-276.
- [4] Kauffman, G. B.; Mayo, I. *The Chemical Educator* **June, 1997**, *2*, 1.
- [5] Liu, C.; Qin, H.; Mather P. T. *Journal of Materials Chemistry* **2007**, *17*, *16*, 1543-1558.
- [6] Otsuka, K.; Sakamoto, H.; Shimizu, K. *Acta Metallurgica* **1979**, *27*, 585-601.
- [7] Kakeshita, T.; Shimizu, K.; Maki, T.; Tamura, I.; Kijima, S.; Date, M. *Scripta Metallurgica* **1985**, *19*, 973-976.
- [8] Chernenko, V. A.; Cesari, E.; Kokorin, V. V.; Vitenko, I. N. *Scripta Metallurgica et Materialia* **1995**, *33*, 1239-1244.
- [9] Chernenko, V. A.; Segui, C.; Cesari, E.; Pous, J.; Kokorin, V. V. *Physical Review B (Condensed Matter)* **1998**, *57*, 2659-2662.
- [10] Otsuka, K.; Wayman, C. M., Eds.; In *Shape Memory Materials*; Cambridge University Press: The Pitt Building, Trumpington Street, Cambridge CB2 1RP, United Kingdom, 1999; pp 298.
- [11] Shaw, J. A. *Materials Instabilities in a Nickel-Titanium Shape Memory Alloy*, University of Texas, Austin, UMI, Ann Arbor, Michigan, 1997.
- [12] Van Humbeeck, J. In *Non-medical applications of shape memory alloys*; ICOMAT 98. International Conference on Martensitic Transformations, 7-11 Dec. 1998; Elsevier: San Carlos de Bariloche, Argentina, 1999; Vol. A273-275, pp 134-148.
- [13] Widu, F.; Drescher, D.; Junker, R.; Bourauel, C. *J. Mater. Sci. Mater. Med.* **1999**, *10*, 275-281.
- [14] Schwartz, M., Ed.; In *Encyclopedia of Smart Materials, Volumes 1-2*; John Wiley & Sons: 2002; Vol. 1-2, pp 1193.
- [15] Hiraga, H.; Inoue, T.; Shimura, H.; Matsunawa, A. *Wear* **1999**, *231*, 272-278.
- [16] Zhang, T.; Li, D. Y. *Materials Science & Engineering A (Structural Materials: Properties, Microstructure and Processing)* **2000**, *A293*, 208-214.

- [17] Liang, Y. N.; Li, S. Z.; Jin, Y. B.; Jin, W.; Li, S. *Wear* **1996**, *198*, 236-241.
- [18] Singh, J.; Alpas, A. T. In *Dry sliding wear mechanisms in a Ti<sub>50</sub>Ni<sub>47</sub>Fe<sub>3</sub> intermetallic alloy*; 10th International Conference on Wear of Materials; Boston, MA, USA, 1995; Vol. 181-183, pp 302-311.
- [19] Ni, W.; Cheng, Y.T.; Grummon, D. S. *Applied Physics Letters* **2002**, *80*, 3310-3312.
- [20] Ni, W.; Cheng, Y.T.; Grummon, D. S. *Applied Physics Letters* **2003**, *82*, 2811-2813.
- [21] Ni, W.; Cheng, Y.T.; Lukitsch, M.; Weiner, A. M.; Lev, L. C.; Grummon, D. S. *Wear* **2005**, *259*, 842-848.
- [22] Ni, W.; Cheng, Y.T.; Grummon, D. S. In *Tribological applications of shape memory and superelastic effects*; Surface Engineering 2004 - Fundamentals and Applications, Nov 30-Dec 2 2004; Materials Research Society, Warrendale, PA 15086, United States: Boston, MA, United States, 2005; Vol. 843, pp 89-98.
- [23] Oliver, W. C.; Pharr, G. M. *Journal of Material Research* **1992**, *7*, 1564-1580.
- [24] Oliver, W. C.; Pharr, G. M. *Journal of Material Research* **2004**, *19*, 3.
- [25] Belousov, O. K.; Terent'ev, V. F.; Kogan, I. S. *Metal Science and Heat Treatment* **1975**, *17*, 375-376.
- [26] Sekiguchi, Y.; Watanabe, Y.; Funami, K.; Funakubo, H.; Suzuki, Y. *Journal of the Faculty of Engineering, University of Tokyo, Series B* **1982**, *36*, 777-786.
- [27] Adler, P. H.; Yu, W.; Pelton, A. R.; Zadno, R.; Duerig, T. W.; Barresi, R. *Scripta Metallurgica et Materialia* **1990**, *24*, 943-947.
- [28] Bhattacharya, R. S.; Rai, A. K.; Pronko, P. P. *Materials Letters* **1984**, *2*, 483-486.
- [29] Richman, R. H.; Rao, A. S.; Hodgson, D. E. *Wear* **1992**, *157*, 401-407.
- [30] Tan, L.; Dodd, R. A.; Crone, W. C. *Biomaterials* **2003**, *24*, 3931-3939.
- [31] Philip, T. V.; Beck, P. A. *Journal of Metals* **1957**, *9*, 1269-1271.
- [32] Ren, X.; Miura, N.; Zhang, J.; Otsuka, K.; Tanaka, K.; Koiwa, M.; Suzuki, T.; Chumlyakov, Y. I.; Asai, M. *Materials Science and Engineering A* **2001**, *312*, 196-206.
- [33] Nishida, M.; Honma, T. *Scripta Metallurgica* **1984**, *18*, 1293-1298.
- [34] Saburi, T.; Nenno, S. *Scripta Metallurgica* **1974**, *8*, 1363-1367.

- [35] Schroeder, T. A.; Wayman, C. M. *Scripta Metallurgica* **1977**, *11*, 225-230.
- [36] Zhang, Y.; Cheng, Y. T.; Grummon, D. S. *Applied Physics Letters* **2006**, *88*, 131904-1.
- [37] Otsuka, K.; Ren, X. *Progress in Materials Science* **2005**, *50*, 511-678.
- [38] Miura, S.; Maeda, S. *Philosophical Magazine* **1974**, *30*, 565-581.
- [39] Barcelo, G.; Rapacioli, R.; Ahlers, M. *Scripta Metallurgica* **1978**, *12*, 1069-1074.
- [40] Sakomoto, H.; Kijima, Y.; Shimizu, K.; Otsuka, K. *Scripta Metallurgica* **1981**, *15*, 281-285.
- [41] Ren, X.; Otsuka, K. *Nature* **1997**, *389*, 579-582.
- [42] Hwang, C. M.; Salamon, M. B.; Wayman, C. M. *Philosophical Magazine A (Physics of Condensed Matter, Defects and Mechanical Properties)* **1983**, *47*, 177-191.
- [43] Nam, T. H.; Saburi, T.; Shimizu, K. *Materials Transactions JIM* **1990**, *31*, 959-967.
- [44] Otsuka, K.; Sawamura, T.; Shimizu, K. *Physica Status Solidi (A) Appl. Res.* **1971**, *5*, 457-470.
- [45] Hehemann, R. F.; Sandrock, G. D. *Scripta Metallurgica* **1971**, *5*, 801-805.
- [46] Michal, G. M.; Sinclair, R. *Acta Crystallographica, Section B (Structural Crystallography and Crystal Chemistry)* **1981**, *B37*, 1803-1807.
- [47] Kudoh, Y.; Tokonami, M.; Miyazaki, S.; Otsuka, K. *Acta Metallurgica* **1985**, *33*, 2049-2056.
- [48] Tadaki, T.; Wayman, C. M. *Metallography* **1982**, *15*, 247-258.
- [49] Salamon, M. B.; Meichle, M. E.; Wayman, C. M. *Physical Review B (Condensed Matter)* **1985**, *31*, 7306-7315.
- [50] Wu, S. K.; Wayman, C. M. *Acta Metallurgica* **1989**, *37*, 2805-2813.
- [51] Reed-Hill, R. E.; Abbaschian, R. In *Physical Metallurgy Principles*; PWS Publishing: Boston, c1994, c1992; pp xv, 926 p.
- [52] Wechsler, M. S.; Lieberman, D. S.; Read, T. A. *Journal of Metals* **1953**, *5*, 1503-1515.
- [53] Massalski, T.B.; Okamoto, H.; Subramanian, P.R.; Kacprzak, L., Eds.; In *Binary Alloy Phase Diagrams*, 2nd edition, Vol. 3. Materials Park, OH: ASM International; 1990; p. 2874.

- [54] Otsuka, K.; Ren, X. In *Martensitic transformations in nonferrous shape memory alloys*; International Conference on Martensitic Transformations; Elsevier: San Carlos de Bariloche, Argentina, 1999; Vol. A273-275, pp 89-105.
- [55] Eckelmeyer, K. H. *Scripta Metallurgica* **1976**, *10*, 667-672.
- [56] Angst, D. R.; Thoma, P. E.; Kao, M. Y. *Journal De Physique. IV : JP* **1995**, *5*, C8, 747-752.
- [57] Miyazaki, S.; Otsuka, K. *Metallurgical Transactions A (Physical Metallurgy and Materials Science)* **1986**, *17A*, 53-63.
- [58] Lo, Y. C.; Wu, S. K. *Journal of Materials Science* **1995**, *30*, 1577-1583.
- [59] Wu, S. K.; Lin, H. C. In *TiNi-based high temperature shape memory alloys*; In Honour of Professor C M Wayman on the Occasion of His Retirement; TMS: Urban, IL, USA, 1998; pp 197-206.
- [60] Lin, H. C.; Wu, S. K.; Chou, T. S.; Kao, H. P. *Acta Metallurgica et Materialia* **1991**, *39*, 2069-2080.
- [61] Lin, H. C.; Wu, S. K. *Scripta Metallurgica et Materialia* **1992**, *26*, 59-62.
- [62] Kurita, T.; Matsumoto, H.; Abe, H. *J. Alloys Compounds* **2004**, *381*, 158-161.
- [63] Kainuma, R.; Wang, J. J.; Omori, T.; Sutou, Y.; Ishida, K. *Scripta Materialia* **2005**, *52*, 311-16.
- [64] Chang, S. H.; Wu, S. K.; Chang, G. H. *Scripta Materialia* **2005**, *52*, 1341-1346.
- [65] Koike, J.; Parkin, D. M.; Nastasi, M. *Journal of Materials Research* **1990**, *5*, 1414-1418.
- [66] Nakayama, H.; Tsuchiya, K.; Liu, Z.; Umemoto, M.; Morii, K.; Shimizu, T. *Materials Transactions* **2001**, *42*, 1987-1993.
- [67] Nakayama, H.; Tsuchiya, K.; Umemoto, M. *Scripta Materialia* **2001**, *44*, 1781-1785.
- [68] Tae-hyun Nam; Yeon-ho Kim; Gyu-bong Cho; Shin-goo Hur; Sang-sik Jeong *Materials Science & Engineering A (Structural Materials: Properties, Microstructure and Processing)* **2006**, *438-440*, 531-535.
- [69] Eggeler, G.; Khalil-Allafi, J.; Gollerthan, S.; Somsen, C.; Schmahl, W.; Sheptyakov, D. *Smart Materials and Structures* **2005**, *14*, 186-191.
- [70] Hall, E.O. *Proc. Phys. Soc. London B* **1951**, *64*, 747-743.

- [71] Gil Sevillano, J.; Van Houtte, P.; Aernoudt, E. *Progress in Materials Science* **1980**, *25*, 69-409.
- [72] Hughes, D. A.; Hansen, N. *Acta Materialia* **1997**, *45*, 3871-3886.
- [73] Lloyd, D. J.; Kenny, D. *Acta Metallurgica* **1980**, *28*, 639-649.
- [74] Gleiter, H. *Progress in Materials Science* **1989**, *33*, 223-315.
- [75] Koch, C. C. In *Amorphization reactions during mechanical alloying/milling of metallic powders*; International Conference on Contemporary Problems on Reactivity of Solids; Novosibirsk, USSR, 1990; Vol. 8, pp 283-297.
- [76] Suryanarayana, C. *Progress in Materials Science* **2001**, *46*, 1-184.
- [77] Cabibbo, M.; Evangelista, E.; Scalabroni, C. *Micron* **2005**, *36*, 401-414.
- [78] Dimitrov, O.; Korznikov, A. V.; Korznikova, G. F.; Tram, G. *Journal De Physique. IV : JP* **2000**, *10*, 6-33.
- [79] Dong Hyuk Shin; Byung Cheol Kim; Kyung-Tae Park; Wung Yong Choo *Acta Materialia* **2000**, *48*, 3245-3252.
- [80] Horita, Z.; Fujinami, T.; Nemoto, M.; Langdon, T. G. *Journal of Materials Processing Technology* **2001**, *117*, 288-292.
- [81] Valiev, R. Z.; Islamgaliev, R. K.; Alexandrov, I. V. *Progress in Materials Science* **2000/3**, *45*, 103-189.
- [82] Segal, V. M. *Materials Science & Engineering A (Structural Materials: Properties, Microstructure and Processing)* **1995**, *A197*, 157-164.
- [83] Perez, C. J. L.; Berlanga, C.; Perez-Illzarbe, J. In *Processing of aluminum alloys by equal channel angular drawing at room temperature*; International Conference on Advanced Materials Processing Technologies, 18-21 Sept. 2001; Elsevier: Madrid, Spain, 2003; Vol. 143-144, pp 105-111.
- [84] Iwahashi, Y.; Wang, J.; Horita, Z.; Nemoto, M.; Langdon, T. G. *Scripta Materialia* **1996**, *35*, 143-146.
- [85] Karaman, I.; Yapici, G. G.; Chumlyakov, Y. I.; Kireeva, I. V. *Materials Science & Engineering A (Structural Materials: Properties, Microstructure and Processing)* **2005**, *410-411*, 243-247.
- [86] Iwahashi, Y.; Horita, Z.; Nemoto, M.; Langdon, T. G. *Acta Materialia* **1998/5/22**, *46*, 3317-3331.

- [87] Chakkingal, U.; Suriadi, A. B.; Thomson, P. F. *Materials Science & Engineering A (Structural Materials: Properties, Microstructure and Processing)* **1999**, *A266*, 241-249.
- [88] Gholinia, A.; Prangnell, P. B.; Markushev, M. V. *Acta Materialia* **2000**, *48*, 1115-1130.
- [89] Nakashima, K.; Horita, Z.; Nemoto, M.; Langdon, T. G. *Acta Materialia* **1998/3/2**, *46*, 1589-1599.
- [90] Pushin, V. G.; Stolyarov, V. V.; Valiev, R. Z.; Kourov, N. I.; Kuranova, N. N.; Prokofiev, E. A.; Yurchenko, L. I. *Annales de Chimie (Science des Materiaux)* **2002**, *27*, 77-88.
- [91] Pushin, V. G.; Valiev, R. Z. In *The nanostructured TiNi shape-memory alloys: New properties and applications; Interfacial Effects and Novel Properties of Nanomaterials*; Trans Tech Publications Ltd: Warsaw, Poland, 2003; Vol. 94, pp 13-24.
- [92] Pushin, V. G.; Gunderov, D. V.; Kourov, N. I.; Yurchenko, L. I.; Prokofiev, E. A.; Stolyarov, V. V.; Zhu, Y. T.; Valiev, R. Z. In *Nanostructures and phase transformations in TiNi shape memory alloys subjected to severe plastic deformation*; Ultrafine Grained Materials III, Mar 14-18 2004; Minerals, Metals and Materials Society, Warrendale, United States: Charlotte, NC., United States, 2004; , pp 481-486.
- [93] Pushin, V. G.; Stolyarov, V. V.; Valiev, R. Z.; Lowe, T. C.; Zhu, Y. T. *Materials Science and Engineering A* **2005**, *410-411*, 386-389.
- [94] Pushin, V. G.; Valiev, R. Z.; Zhu, Y. T.; Prokoshkin, S. D.; Gunderov, D. V.; Yurchenko, L. I. *Materials Science Forum* **2006**, *503-504*, 539-544.
- [95] Khmelevskaya, I. Y.; Trubitsyna, I. B.; Prokoshkin, S. D.; Dobatkin, S. V.; Tatyagin, E. V.; Stolyarov, V. V.; Prokofjev, E. A. In *Thermomechanical treatment of Ti-Ni-based shape memory alloys using severe plastic deformation*; International Conference on Processing and Manufacturing of Advanced Materials; Trans Tech Publications: Leganes, Madrid, Spain, 2003; Vol. 426-432, pp 2765-2770.



- [96] Stolyarov, V. V.; Prokof'ev, E. A.; Prokoshkin, S. D.; Dobatkin, S. B.; Trubitsyna, I. B.; Khmelevskaya, I. Y.; Pushin, V. G.; Valiev, R. Z. *Physics of Metals and Metallography* **2005**, *100*, 608-618.
- [97] Xie, C. Y.; Fan, Z. G.; Li, Z. H.; Xiang, G. Q.; Cheng, X. H. *Materials Science Forum* **2006**, *503-504*, 1013-1018.
- [98] Karaman, I.; Kulkarni, A. V.; Luo, Z. P. *Philosophical Magazine* **2005**, *85*, 1729-1745.
- [99] Otsuka, K.; Shimizu, K. *International Metals Reviews* **1986**, *31*, 93-114.
- [100] Saburi, T.; Yoshida, M.; Nenno, S. *Scripta Metallurgica* **1984**, *18*, 363-370.
- [101] Miyazaki, S.; Otsuka, K.; Suzuki, Y. *Scripta Metallurgica* **1981**, *15*, 287-292.
- [102] Otsuka, K.; Wayman, C. M.; Nakai, K.; Sakamoto, H.; Shimizu, K. *Acta Metallurgica* **1976**, *24*, 207-226.
- [103] Shaw, G. A.; Stone, D. S.; Johnson, A. D.; Ellis, A. B.; Crone, W. C. *Applied Physics Letters* **2003**, *83*, 257-259.
- [104] Gall, K.; Juntunen, K.; Maier, H. J.; Sehitoglu, H.; Chumlyakov, Y. I. *Acta Materialia* **2001**, *49*, 3205-3217.
- [105] Clayton, P. *Wear* **1993**, *162-64*, 202-210.
- [106] Liao, H. M.; Lin, H. C.; He, J. L.; Chen, K. C.; Lin, K. M. In *Dry sliding wear of TiNi shape memory alloys*; International Conference on Displacive Phase Transformations and their Applications in Materials Engineering. In honor of Professor C M Wayman on the occasion of his retirement, 8-9 May 1996; TMS: Urban, IL, USA, 1998; pp 251-6.
- [107] Lin, H. C.; Liao, H. M.; He, J. L.; Chen, K. C.; Lin, K. M. *Metall Mat Trans A Phys Metall Mat Sci* **1997**, *28A*, 1871-1877.
- [108] Liu, R.; Li, D. Y. *Materials Science and Technology* **2000**, *16*, 328-332.
- [109] Li, D. Y. *Smart Materials and Structures* **2000**, *9*, 717-726.
- [110] Li, D. Y.; Liu, R. *Wear* **1999**, *225-229*, 777-783.
- [111] Li, D. Y.; Ma, X. *Journal of Materials Science and Technology* **2001**, *17*, 45-46.
- [112] Qian, L.; Xiao, X.; Sun, Q.; Yu, T. *Appl. Phys. Lett.* **2004**, *84*, 1076-1078.
- [113] Qian, L.; Sun, Q.; Xiao, X. *Wear* **2006**, *260*, 509-522.

- [114]Ni, W.; Cheng, Y.; Lukitsch, M. J.; Weiner, A. M.; Lev, L. C.; Grummon, D. S. *Applied Physics Letters* **2004**, *85*, 4028-4030.
- [115]Johnson, K. L.; In *Contact Mechanics*; Cambridge University Press, Cambridge, UK, 1985.
- [116]Tong, H. C.; Wayman, C. M.; *Acta Metallurgica* **1974**, *22*, 887-896.
- [117]Fan, G.; Chen, W.; Yang, S.; Zhur, J.; Ren, X.; Otsuka, K. *Acta Materialia* **2004**, *52*, 4351-4362.
- [118]Tyumentsev, A. N.; Surikova, N. S.; Litovchenko, I. Y. et al. *Acta Materialia* **2004**, *52* 2067.
- [119]Tabor, D. In *The Hardness of Metals*, Oxford University Press, Oxford, 1951, 46-51.

## VITA AUCTORIS

NAME Sanjib Kumar Dey

PLACE OF BIRTH Cuttack, Orissa, India

YEAR OF BIRTH 1979

EDUCATION Bachelor of Engineering (B.E.), Metallurgical Engineering  
National Institute of Technology, Karnataka, India  
1997-2001

Master of Applied Science (M.A.Sc), Engineering Materials  
University of Windsor, Windsor, Ontario, Canada  
2005-2007